ACS chemical biology

Articles

pubs.acs.org/acschemicalbiology

Topology Specific Stabilization of Promoter over Telomeric G-Quadruplex DNAs by Bisbenzimidazole Carboxamide Derivatives

V. Dhamodharan,*[,‡] S. Harikrishna,[‡] Achikanath C. Bhasikuttan,[§] and P. I. Pradeepkumar*[,‡]

[‡]Department of Chemistry, Indian Institute of Technology Bombay, Powai, Mumbai 400076, India

[§]Radiation & Photochemistry Division, Bhabha Atomic Research Centre, Mumbai 400 085, India

Supporting Information

ABSTRACT: Various potential G-quadruplex forming sequences present in the genome offer a platform to modulate their function by means of stabilizing molecules. Though G-quadruplex structures exhibit diverse structural topologies, the presence of G-quartets as a common structural element makes the design of topology specific ligands a daunting task. To address this, the subtle structural variations of loops and grooves present in the quadruplex structures can be exploited. To this end, we report the design and synthesis of quadruplex stabilizing agents based on bisbenzimidazole carboxamide derivatives of pyridine, 1,8-naphthyridine, and 1,10-phenanthroline. The designed ligands specifically bind to and stabilize promoter quadruplexes having parallel topology over any of the human telomeric quadruplex topologies (parallel, hybrid, or antiparallel) and duplex DNAs. CD melting studies indicate that ligands could impart higher stabilization to *c-MYC* and c-KIT promoter quadruplexes (up to 21 °C increment in T_m) than telomeric and duplex DNAs ($\Delta T_m \leq 2.5$ °C). Consistent with a CD melting study, ligands bind strongly ($K_b = \sim 10^4$ to 10^5 M^{-1}) to *c-MYC* quadruplex DNA. Molecular modeling and dynamics studies provide insight into how the specificity is achieved and underscore the importance of flexible *N*-alkyl side chains attached to the benzimidazole-scaffold in recognizing propeller loops of promoter quadruplexes. Overall, the results reported here demonstrate that the benzimidazole scaffold represents a potent and powerful side chain, which could judiciously be assembled with a suitable central core to achieve specific binding to a particular quadruplex topology.

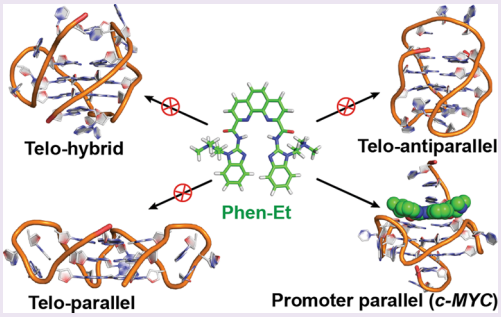

G-quadruplexes are structurally diverse and dynamic four stranded nucleic acids formed by stacking of two or more G-quartets in the presence of appropriate metal ions.[1,2] The number of such putative G-quadruplex-forming sequences in the human genome was estimated to be over 370 000, which will increase further by considering bulge formations in the strands of quadruplexes.[3,4] These quadruplex structures have been detected at the telomere, across the chromosomes, and in the transcriptome of human cells by employing quadruplex-specific antibody and thus validate their existence *in vivo*.[5−7] Formation of stable G-quadruplexes induces various effects on cellular functions, such as stalling replication,[8] halting the function of telomerase enzymes,[9] and modulating gene expression at the transcription[10] and translation levels.[11,12] Therefore, quadruplexes are harnessed as potential therapeutic targets by exogenous small molecules or ligands.[13] In this direction, small molecules are shown to bind and stabilize the quadruplex structures present in the genome and transcriptome in cellular systems.[5,6] They are also known to induce the DNA damage response pathway[14,15] and promote synthetic lethality in cancer cells.[16]

Various promoter quadruplexes present upstream of proto-oncogenes represent the six hallmarks of cancer[17] and can be targeted by ligands to down-regulate their expression.[10,18] Most of the promoter quadruplexes such as *c-MYC*,[19] c-KIT,[20,21] *VEGF*,[22] *RET*,[23] *HIF-1α*,[24] etc. are known to adopt parallel topology. Contrarily, a growing amount of evidence indicates that the parallel form of telomeric DNA might not be a biologically relevant target as it requires dehydrated conditions to exist.[25−27] Recent findings suggest that hybrid-1, hybrid-2, and 2-tetrad antiparallel basket topologies are the biologically relevant quadruplex structures for the telomeric DNA.[26,28−30] Major folding differences between parallel-promoter quadruplexes and telomeric quadruplexes can be exploited for the design of topology-specific ligands. G-quadruplex ligands, which can specifically discriminate one quadruplex over other quadruplexes without compromising selectivity over the duplex, are highly desirable to exploit structure-specific therapeutic interventions at the genomic level. However, from a purely therapeutic point of view, the extent of specificity needed between various quadruplexes is poorly understood. A G-quadruplex specific ligand could also be added judiciously along with the quadruplex specific antibodies to reinforce the visualization quadruplex structure at the precise location in the genome, as reported for the RNA quadruplex visualization by carboxypyridostatin (carboxyPDS) ligand.[6]

Received: June 19, 2014
Accepted: December 11, 2014

DOI: 10.1021/cb5008597
ACS Chem. Biol. XXXX, XXX, XXX−XXX

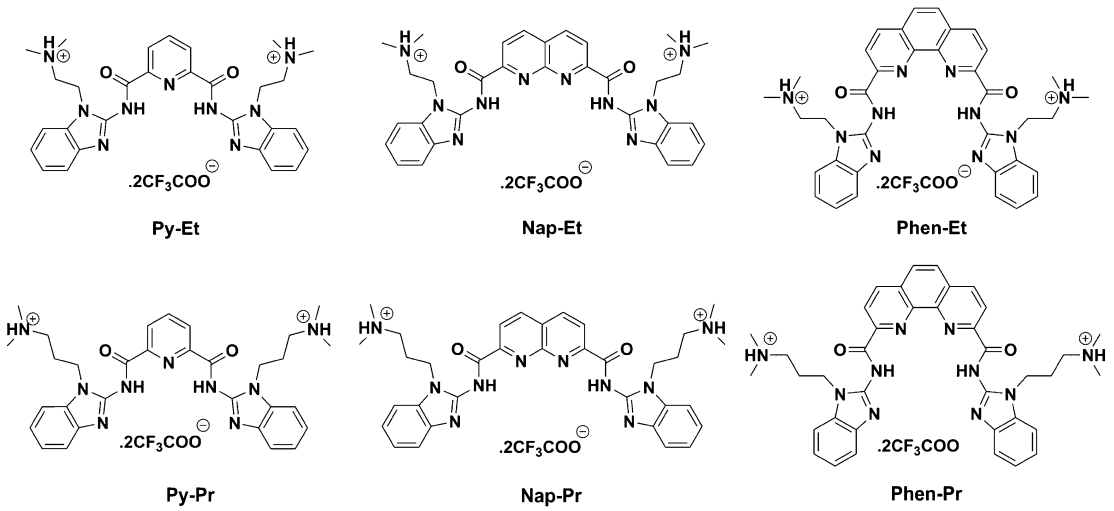

Figure 1. Structures of topology specific G-quadruplex DNA stabilizing ligands. Central cores contain pyridine (Py), 1,8-naphthyridine (Nap), and 1,10 phenanthroline (Phen), and benzimidazole contains dimethyl aminopropyl (Pr) and dimethyl aminoethyl (Et) as side chains.

To date, numerous ligands have been reported as G-quadruplex stabilizing agents with high selectivity toward quadruplex over duplex DNAs.[31−33] Nevertheless, it is highly challenging to design a ligand which is specific for a targeted quadruplex over other quadruplexes, as G-quartet is the common structural feature in all quadruplexes. But loops (diagonal, lateral, and propeller) and width of the grooves (narrow, medium, and wide) are differed for each quadruplex considerably.[34] Furthermore, there are considerable differences in the structures reported for native quadruplexes (without ligand) and quadruplex−ligand complexes as ligand-induced binding pockets are created in the latter due to rearrangement of the flexible loops or flanking nucleotides.[35,36] Therefore, these flexible loops and unique groove widths[34] need to be considered along with the large π surface area of the quartet for achieving specific binding of a small molecule to the targeted quadruplex topology.[36,37] Interestingly, few ligands are reported to specifically stabilize the human telomeric quadruplex having parallel, antiparallel, or hybrid topologies over promoter quadruplexes with parallel topologies. For example, acridine based ligands bind specifically to telomeric DNA over promoter quadruplexes (*c-KIT1*, *c-KIT2*).[38] Receptor-based virtual screening strategies also identified specific telomeric binding ligands.[39] In addition, ligands which discriminate between various telomeric quadruplexes are also reported. Oxazole-based heptacyclic derivative (TOxaPy) is able to specifically stabilize the antiparallel form of human telomeric DNA over other topologies;[40] *N*-methyl mesoporphyrin IX (NMM) showed specificity for parallel topology over antiparallel topology of telomeric DNA.[41] The recently reported pyridostatin based ligand is able to discriminate the telomeric RNA quadruplex from its DNA counterpart.[42]

Ligands having few fold binding preferences for promoter quadruplexes over telomeric DNA are also reported.[43−47] So far, to the best of our knowledge, there is no report on ligands, which specifically bind to and stabilize the promoter quadruplex DNAs over all the known topologies of human telomeric DNA. Moreover, due to the lack of structural information, the reasons for the limited topological bias of the reported ligands are poorly understood.

In this work, we report the specific recognition and stabilization of promoter quadruplexes over telomeric quadruplexes by benzimidazole carboxamide derivatives of pyridine, 1,8-naphthyridine, and 1,10-phenanthroloine (Figure 1). Ligand-induced stabilization of quadruplex and duplex DNAs assessed by CD melting studies show that all ligands are able to impart higher stabilization to promoter quadruplexes (*c-MYC*, *c-KIT1*, and *c-KIT2*) over human telomeric and duplex DNAs. CD and NMR titration studies point out that the ligand binds to the *c-MYC* quadruplex through end-stacking and is able to induce the formation of the *c-MYC* quadruplex in the absence of added metal ions. UV−vis titration studies reveal that the ligands could specifically bind to the *c-MYC* quadruplex over telomeric and duplex DNA. In addition, the above ligands are able to arrest primer extension at the *c-MYC* quadruplex forming site with low IC_{50} values. Structural insights obtained by molecular modeling and dynamics studies explain why ligands bind specifically to parallel quadruplexes over telomeric and duplex DNAs.

RESULTS AND DISCUSSION

Ligand Design and Synthesis. Benzimidazole scaffolds, which are structural isosteres of purine bases, have widely been studied as duplex groove binders as well as quadruplex DNA stabilizing agents.[48−50] Metal complexes such as platinum(II) and palladium(II) of bisbenzimidazole were able to bind and stabilize quadruplex DNA selectively over duplex DNA.[51,52] By and large, these benzimidazole based ligands do not discriminate one quadruplex topology over others, and their selectivity was explored only in the context of targeted quadruplex over duplex DNA.[51,53] Mostly flexible alkyl side chains appended to these benzimidazole ligands are positioned on the benzene ring of the benzimidazole moiety.[49,53] We envisage that the precise location of side chains on the imidazole ring of the benzimidazole moiety (Figure 1) with appropriate length will have a crucial role in differentiating various quadruplexes as accessibility to the phosphate backbone of loops of each quadruplex structure is quite different. Herein, six bisbenzimidazole carboxamide derivatives of pyridine, 1,8-naphthyridine, and 1,10-phenanthroline were designed and synthesized to discriminate between various quadruplex topologies (Figure 1). The aromatic central cores were chosen because of their presence in several G-quadruplex DNA stabilizing agents.[54−58] The rationales for the design of such

DOI: 10.1021/cb5008597
ACS Chem. Biol. XXXX, XXX, XXX−XXX

Scheme 1. Synthesis of Bisbenzimidazole Derivatives of Pyridine, 1,8-Naphthyridine, and 1,10-Phenanthroline Carboxamides[a]

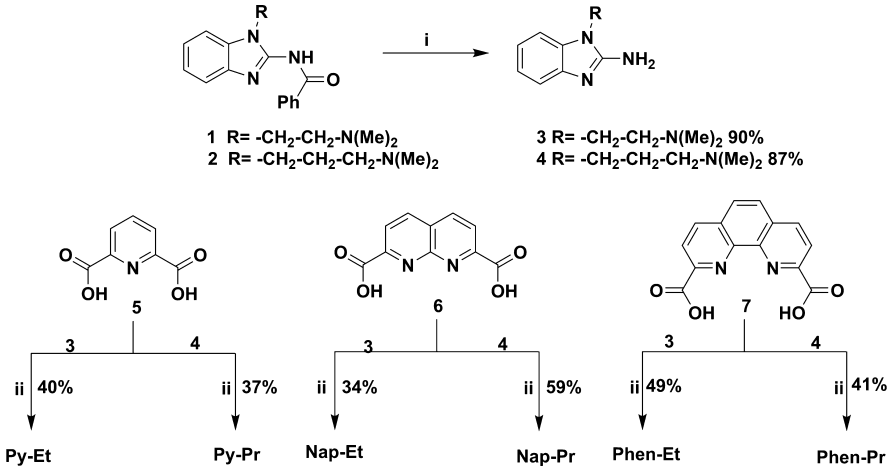

[a]Reagents and conditions: (i) CH_3NH_2-EtOH (33%), 80 °C, 4 d; (ii) (a) EDC.HCl, HOBt, *N*-methyl morpholine, DCM, rt, 24 h (b) TFA, DCM, rt, 10 min.

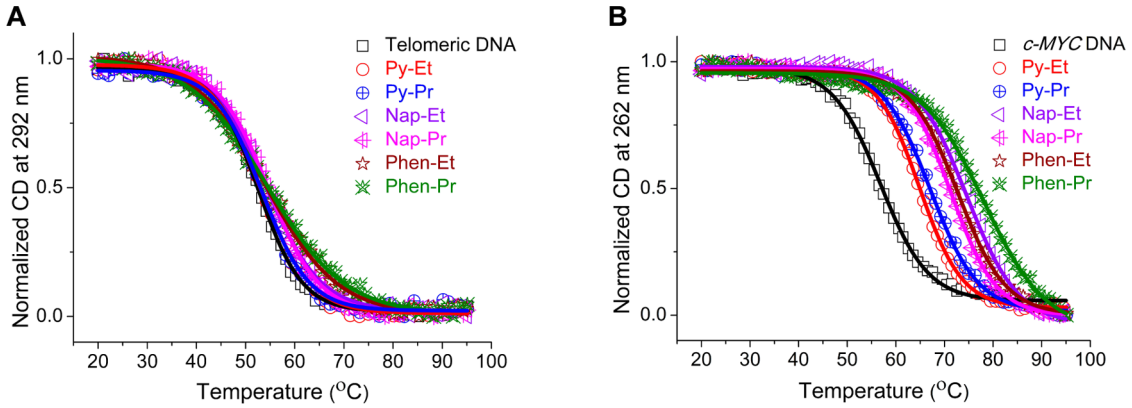

Figure 2. CD melting curves for telomeric and *c-MYC* DNAs (10 μM in 10 mM lithium cacodylate buffer pH 7.2) in the absence and presence of ligands (3 molar equiv). (A) Telomeric DNA (10 mM KCl, and 90 mM LiCl). (B) *c-MYC* DNA (1 mM KCl and 99 mM LiCl).

ligands are as follows: (1) Nitrogen atoms present in the central core and the NH of the amide bond can form internal H-bonding, which would fix the ligand conformation to a crescent shape.[59] This is expected to enhance its accessibility to the top of the G-quartets. (2) As the benzimidazole scaffold is structurally similar to purine bases, the stacking interactions between benzimidazole and guanine bases in the quartet are anticipated. (3) Furthermore, the positively charged flexible alkyl side chains have the potential to interact with negatively charged phosphate groups present in the loop and grooves.

Syntheses of target molecules (Figure 1) were achieved by coupling corresponding dimethlyaminoethyl or dimethylaminopropyl substituted 2-aminobenzimidazole compounds with the appropriate dicarboxylic acid as shown in Scheme 1. The key precursors **1** and **2**, needed for the synthesis of side chains **3** and **4**, were prepared using the reported procedures with slight modifications starting from 2-nitrofluorobenzene in four steps (Scheme S1, Supporting Information).[60] Deprotection of the benzoyl group in **1** and **2** using ethanolic methylamine (~33%) in a sealed tube at 80 °C furnished the required amines **3** and **4** in 87−90% yields. The direct coupling of these amine compounds **3** and **4** with the dicarboxylic acid of pyridine **5**, 1,8-naphthyridine **6**, and 1,10-phenanthroline **7** by EDC·HCl yielded corresponding amide compounds. These amides were treated with trifluoroacetic acid (TFA) to give final ligands **Py-Et**, **Py-Pr**, **Nap-Et**, **Nap-Pr**, **Phen-Et**, and **Phen-Pr** (Figure 1 and Scheme 1) in the protonated forms in 34−59% yields.

CD Melting Studies. Initial screening of all ligands (Figure 1) was carried out using a CD melting assay, which provided the ligand-induced thermal stabilization of quadruplex and duplex DNAs. Initially, the effect of ligands on human telomeric DNA was tested. Thermal melting of telomeric DNA was monitored at 292 nm since its CD spectrum in K^+ solution has a major positive band centered at 292 nm for the mixed populations of parallel and hybrid structures. In the absence of any ligand, the telomeric DNA showed a T_m of 52.6 ± 0.2 °C (Figure 2A, Table 1). In the presence of various ligands the T_m was increased only marginally up to a maximum of 2.5 °C. These results clearly point out that ligand-induced stabilization of telomeric DNA is very low. Next, we were interested to check the effect of ligands on stabilization of promoter quadruplex DNAs (*c-KIT1*, *c-KIT2*, and *c-MYC*). Promoter quadruplexes are known to adopt parallel topology under K^+ conditions, thus the melting studies were monitored at 262 nm (Figure 2B and Figure S1, Supporting Information). Interestingly, unlike the marginal ligand-induced stabilization observed for telomeric DNA, stabilization of the promoter quadruplex was increased up to 20.7 °C for **Phen-Pr** (Table 1). The ΔT_m values are in the range of 1.8−10.0 °C for **Py-Et** and **Py-Pr**; 8.1−17.8 °C for **Nap-Et** and **Nap-Pr**; and 16.0−20.7 °C for

DOI: 10.1021/cb5008597
ACS Chem. Biol. XXXX, XXX, XXX−XXX

Table 1. Thermal Stability of Various Quadruplex DNAs and Duplex DNA with Ligands Measured by CD Melting Experiments

	ΔT_m (°C)[a]				
ligands	telomeric DNA	*c-KIT1*	*c-KIT2*	*c-MYC*	duplex ds17
Py-Et	0.5 ± 0.4	7.1 ± 0.3	1.8 ± 0.8	8.0 ± 0.3	1.0 ± 0.4
Py-Pr	0.6 ± 0.2	7.5 ± 0.3	3.7 ± 0.7	10 ± 0.4	2.0 ± 0.4
Nap-Et	1.5 ± 0.5	11.3 ± 0.3	10.3 ± 0.9	17.8 ± 0.2	0
Nap-Pr	2.5 ± 0.5	14.5 ± 0.9	8.1 ± 0.9	14.5 ± 0.8	2.3 ± 0.4
Phen-Et	1.0 ± 0.8	18.5 ± 0.9	16.3 ± 0.6	16.0 ± 0.3	0
Phen-Pr	1.7 ± 0.8	20.7 ± 1.1	16.6 ± 0.7	19.6 ± 0.5	n.d.

[a] ΔT_m represents the shift in thermal melting [ΔT_m = T_m (DNA + 3 mol equiv ligand) − T_m (DNA)]. For all experiments, DNA 10 μM for quadruplex or 15 μM for duplex DNA in 10 mM lithium cacodylate buffer pH 7.2 was used. The T_m values are 52.6 ± 0.2 °C [telomeric DNA in 10 mM KCl, 90 mM LiCl]; 47.7 ± 0.3 °C [*c-KIT1* DNA in 10 mM KCl, 90 mM LiCl]; 52.8 ± 0.6 °C [*c-KIT2* DNA in 1 mM KCl, 99 mM LiCl]; 56.7 ± 0.1 °C [*c-MYC* DNA in 1 mM KCl, 99 mM LiCl]; 62.7 ± 0.4 °C [ds-17 DNA in 10 mM KCl and 90 mM LiCl]. All experiments were triplicated, and the values reported are an average of three independent measurements with the estimated standard deviation. As the ionic strength is known to modulate the binding of a cationic ligand to the negatively charged DNA, for all melting experiments, a total ionic strength of 110 mM was maintained with the help of Li^+ ions, which does not alter the structure and stability of the K^+-induced quadruplex forms.[61]

Phen-Et and **Phen-Pr** ligands. This clearly indicates that the effect of stabilization increases with increasing π surface area of the central core (1,10-phenanthroline > 1,8-naphthyridine > pyridine). However, there is no conclusive order in the magnitude of stabilization of promoter quadruplexes with increasing side chain length from dimethylaminoethyl to dimethylaminopropyl due to the presence of diverse central cores in the ligands. To further validate our findings on the distinct specificity of the ligands toward promoter quadruplexes, melting experiments were also carried out with a well-characterized ligand, **3AQN** (bisquinolium derivative of 1,8-naphthyridine),[55,58] under identical salt and buffer conditions. Results showed that the reference compound **3AQN** conferred stability to both telomeric (ΔT_m = 24.0) and *c-MYC* (ΔT_m > 30.0) quadruplex DNAs (Figure S2, Supporting Information), contrasting with the results obtained with bisbenzimidazole ligands (Table 1).

Having established specific stabilization promoter quadruplexes over telomeric DNA by the benzimidazole ligands, the ability of the ligands to stabilize duplex DNA was also verified. The thermal stability of duplex DNA monitored at 242 nm provided a T_m of 62.7 ± 0.4 °C in the absence of ligands (Table 1, Figure S1C, Supporting Information). The stability of duplex DNA upon the addition of ligands was increased by 2.3 °C. Remarkably, there was no detectable stabilization observed for duplex DNA in the presence of **Nap-Et** and **Phen-Et** ligands. Overall results show that ligands selectively stabilize promoter quadruplexes over duplex DNAs.

Since the telomeric DNA is known to adopt antiparallel topology in the presence of Na^+ ions, melting studies were performed to examine whether these ligands could stabilize the antiparallel topology. Due to the lowest induced-stabilization effect of **Phen-Et** to the telomeric DNA (ΔT_m = 1 °C), further studies were focused on this ligand. Thermal melting of the antiparallel form of telomeric DNA provided a T_m of 51.2 ± 0.4 °C in the absence of ligands (Figure S3A, Supporting Information). The addition of **Phen-Et** resulted in no change in T_m, indicating that the ligand did not stabilize the antiparallel quadruplex structure of telomeric DNA (Figure S3A, Supporting Information). Having established marginal ligand-induced stabilization of telomeric quadruplex DNA both in Na^+ and in K^+ ions, we evaluated the effect of the ligand on the parallel topology of telomeric DNA. It is reported that under polyethylene glycol (PEG) conditions in the presence of K^+ ions, telomeric DNA is known to adopt only the parallel topology.[62] Similar to the results obtained with antiparallel quadruplex topology, the addition of **Phen-Et** showed no stabilizing effect on the telomeric parallel topology (Figure S3B, Supporting Information). In contrast, the reference compound **3AQN** stabilizes the PEG-induced parallel quadruplex DNA by a ΔT_m = 10.0 (Figure S3C, Supporting Information), distinguishing it from **Phen-Et**.

Another possibility one should not rule out is the formation of higher-order quadruplex structures by human telomeric DNA.[26,30,63] In order to study whether the ligand, **Phen-Et**, can stabilize this higher order form of telomeric DNA, a sequence $AGGG(TTAGGG)_7$, which can form two contiguous quadruplexes, was used. Results show that the T_m of long telomeric quadruplex DNA was increased only by ∼2 °C in the presence of the ligand (Figure S3D, Supporting Information). Overall the CD melting data indicate that ligands are less effective in stabilizing any of the telomeric DNA topological forms (antiprallel, parallel, hybrid, or higher order forms). The marginal ligand-assisted stabilization observed for telomeric DNA prompted us to rationalize these findings. Quadruplexes have different sites (quartets, loops, and grooves) to which ligands bind via various noncovalent interactions such as stacking, electrostatic, hydrogen-bonding and van der Waals forces. It appears that the parallel form of promoter quadruplexes fulfills the structural requirements to maximize these noncovalent interactions with the ligands. These aspects were probed in detail by molecular modeling and dynamics studies (see in the respective section).

CD and NMR Titration Studies. CD studies were performed to examine whether the ligand could induce quadruplex structures from the promoter and telomeric DNAs in the absence of added metal ions. In the absence of added metal ions, *c-MYC* DNA exhibited a positive peak at 264 nm and a negative peak at 240 nm (Figure 3A), which are consistent with the parallel topology. Upon the addition of **Phen-Et**, the ellipticity at 263 nm remarkably increased, indicating strong induction of the quadruplex form (Figure 3A). Other promoter DNAs such as *c-KIT1* and *c-KIT2* were also induced the parallel form of the quadruplex but with less prominent CD enhancement by the addition of **Phen-Et** (Figure S4A and B, Supporting Information). Contrarily, the CD spectrum of telomeric DNA in the absence of added metal ions showed a weak positive band at 256 nm and negative bands at 279 and 238 nm (Figure S4C, Supporting Information).[64] In the presence of **Phen-Et**, no well-defined

DOI: 10.1021/cb5008597
ACS Chem. Biol. XXXX, XXX, XXX−XXX

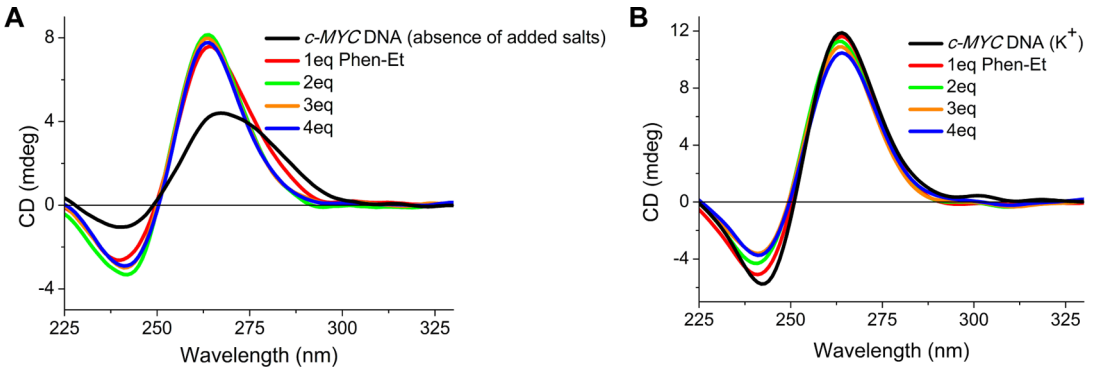

Figure 3. CD titration of ligand **Phen-Et** to *c-MYC* DNA (15 μM in 10 mM Tris buffer pH 7.2) in the absence and presence of K^+ ions. (A) *c-MYC* DNA with increasing molar equiv (0 to 4) of **Phen-Et**. (B) *c-MYC* DNA (100 mM KCl) with increasing molar equiv (0 to 4) of **Phen Et**.

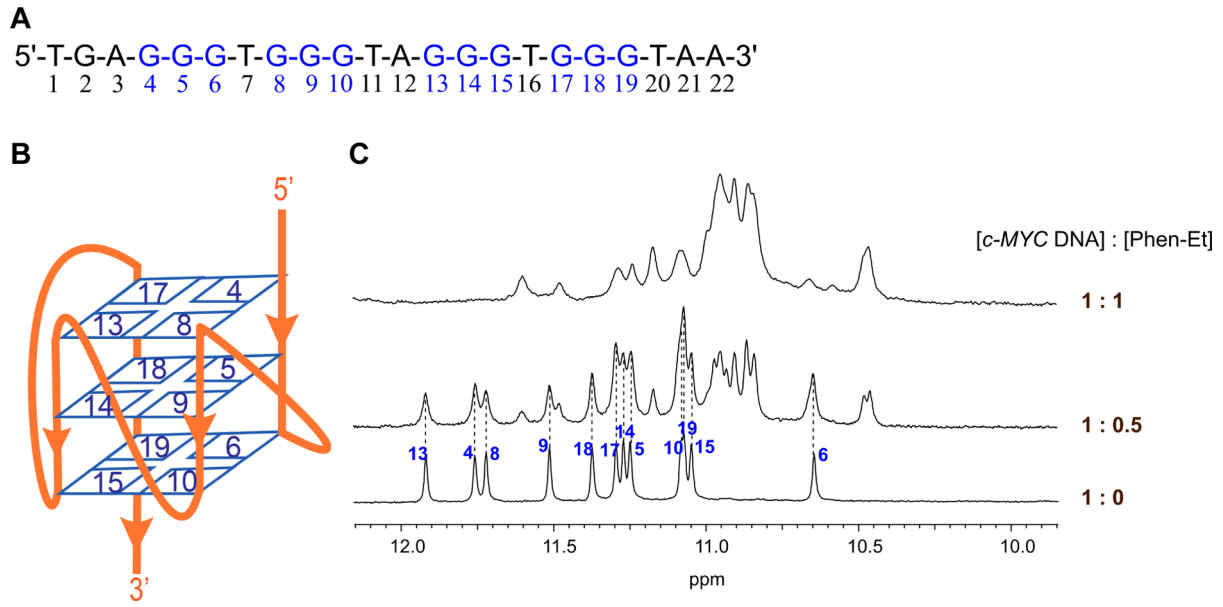

Figure 4. Sequence, topology, and ^{1}H NMR (800 MHz) spectra and of *c-MYC* DNA. (A) Sequence of *c-MYC* DNA. The guanine bases (G) which are involved in G-quartet formation are labeled in blue. (B) Topology of the parallel *c-MYC* quadruplex DNA.[19] (C) ^{1}H NMR spectra of imino region of *c-MYC* DNA (227 μM in 80 mM KCl and 20 mM potassium phosphate buffer pH 6.7) in the absence and presence of **Phen-Et**. Spectra were recorded in a H_2O/D_2O mixture (9:1) at 25 °C. At a 1:0.5 DNA/ligand molar ratio, both the *c-MYC* quadruplex–ligand complex and *c-MYC* quadruplex coexist, and at a 1:1 molar ratio, only the quadruplex–ligand complex exists. Dotted lines indicate imino protons corresponding to the ligand-free *c-MYC* quadruplex. Imino protons of G-quartets were labeled based on the previous literature findings.[19]

quadruplex peaks corresponding to any of the known topologies were observed (Figure S4C Supporting Information), owing to its nonspecific interactions with an unfolded-telomeric DNA structure. In contrast, many classes of G-quadruplex selective ligands such as telomestatin,[64] bisquinolinium compounds (**360A**, **3AQN**),[55] and thioflavin T[33] are known to induce the antiparallel quadruplex structure of the telomeric DNA in the absence of added salts.

CD studies were also performed in the presence of metal ions (K^+) to examine the structural changes of preformed quadruplex upon the addition of the ligand. In the presence of K^+ ions, *c-MYC* DNA exists in parallel form as evidenced from the positive peak at 263 nm and negative peak at 242 nm (Figure 3B).[65] The addition of **Phen-Et** to the preformed quadruplex led to very slight changes in ellipticity, and the parallel topology was retained in the folded form. Similarly, parallel topologies of *c-KIT1* and *c-KIT2* quadruplex structures were retained after the addition of **Phen-Et** (Figure S5A and B, Supporting Information). In the case of telomeric quadruplex DNA, induction of the weak antiparallel form was observed by the addition of **Phen-Et** (Figure S5C, Supporting Information). However, from the CD melting studies, it was apparent that such induction by the ligand has conferred only marginal stability to the telomeric quadruplex DNA. Overall, CD studies clearly suggest that **Phen-Et** is able to induce and stabilize the parallel quadruplex form of *c-MYC* quadruplex DNA.

Imino-protons in the ^{1}H NMR spectra of the quadruplex and quadruplex–ligand complex provide valuable insights into the stoichiometry and binding mode of ligands. It is reported that when ligands bind to the quadruplex by the end-stacking mode, the imino-proton peaks of all G-quartets get shielded, which leads to upfield chemical shifts.[66−68] In contrast, when ligands bind to grooves of the quadruplex, chemical shifts of imino protons are unaffected or undergo only nominal changes.[39,65,69] The NMR spectrum of *c-MYC* DNA showed 12 well-resolved distinct peaks in the imino region corresponding to 12 guanines present in the three quartets of the quadruplex (Figure 4).[66] However, when 0.5 molar equiv of **Phen-Et** was titrated into *c-*

DOI: 10.1021/cb5008597
ACS Chem. Biol. XXXX, XXX, XXX−XXX

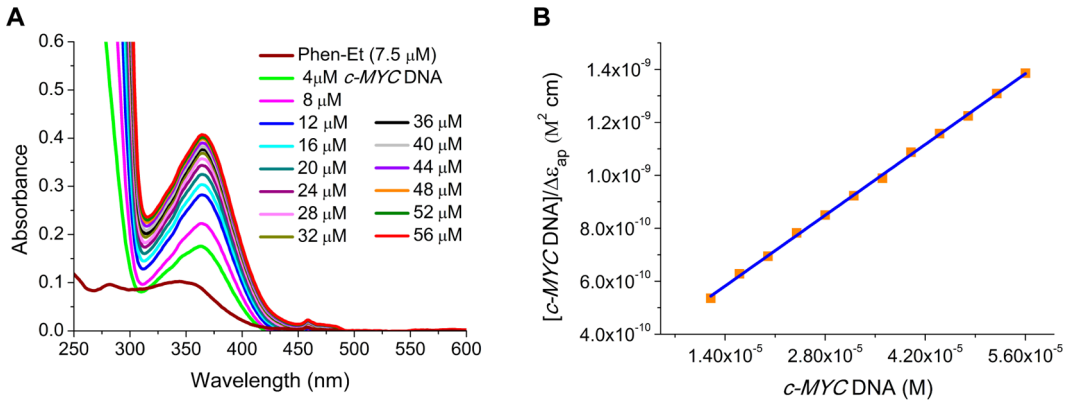

Figure 5. Absorption spectra of **Phen-Et** and with *c-MYC* DNA and the binding plot. (A) Addition of *c-MYC* DNA (4−56 μM in 100 mM KCl and 10 mM lithium cacodylate, pH 7.2) into the solution of **Phen-Et** (7.5 μM under identical salt and buffer conditions) at 25 °C. (B) Plot of [*c-MYC* DNA]/$\Delta\varepsilon_{ap}$ versus [*c-MYC* DNA].

MYC DNA, a new set of peaks with upfield chemical shifts for the ligand−quadruplex complex emerged, while the peaks corresponding to *c-MYC* DNA (without ligand) were also present (Figure 4). This clearly indicates that the ligand favors the end-stacking binding mode and a complete saturation of the quadruplex was not attained and consequently mixed populations of both quadruplex and quadruplex-ligand complex were coexisting. Interestingly, upon the addition of 1 molar equiv of **Phen-Et** (1:1 stoichiometry), only the upfield shifted imino protons for a single dominant conformation of the quadruplex−ligand complex were observed (Figure 4). These results are in line with recently reported NMR studies of quadruplex−ligand complexes wherein quindoline and phenanthroline-bisquinolinium (Phen-DC3) compounds induce an upfield shift of all imino-protons as they bind onto the terminal quartet of the *c-MYC* quadruplex.[66,68]

UV−Vis Absorption Studies. UV titration experiments were performed to find the binding constant of the ligands with various DNAs. Ligands are known to exhibit a bathochromic shift, hyperchromicity, or hypochromicity upon binding with DNA.[33,51,70,71] A solution of **Phen-Et** displayed absorbance maxima at 282 nm and around 344 nm (Figure 5A). The addition of the *c-MYC* quadruplex to this solution resulted in a red-shift by 20 nm and remarkable hyperchromicity at 364 nm (Figure 5A), indicating a strong interaction of **Phen-Et** and *c-MYC* quadruplex DNA. The ratio of slope-to-intercept, obtained by the plotting of [*c-MYC*]/$\Delta\varepsilon_{ap}$ versus [*c-MYC*], provided a binding constant (K_b) of $(6.39 \pm 0.33) \times 10^4$ M^{-1} at 25 °C (Figure 5B, see experimental section in the Supporting Information for details). Under identical salt and buffer concentrations, UV−vis titrations were also performed for telomeric and duplex DNA (Figure S6, Supporting Information). Though a red-shift was observed upon the addition of telomeric and duplex DNA to the **Phen-Et** solution, there was only a slight change in the absorbance at 364 nm (Figure S6, Supporting Information). Due to the very weak interaction of **Phen-Et** with telomeric and duplex DNA, we were not able to deduce the binding constants. These results clearly reinstate that **Phen-Et** specifically binds to and stabilizes the *c-MYC* quadruplex over telomeric and duplex DNAs.

Since **Phen-Pr** has imparted higher stabilization to the *c-MYC* quadruplex over other ligands, its binding affinity to the *c-MYC* quadruplex was also determined. Consistent with the **Phen-Et** ligand, the addition of *c-MYC* DNA into the solution of **Phen-Pr** also exhibited a red-shift (by 20 nm) and remarkable hyperchromicity at 364 nm. The binding constant (K_b) of **Phen-Pr** was found to be $(2.41 \pm 0.16) \times 10^5$ M^{-1}, which is ∼4 fold higher than that of **Phen-Et** (Figure S7A and B, Supporting Information). It is apparent that the observed binding affinities of the ligands are moderate and lower than the potent G-quadruplex stabilizing ligands such as pyridostatin (PDS).[72] This underscore that G-quadruplex specific ligands may not exhibit very high binding affinity so as to maintain the biding specificity confined to a particular topology. Overall, consistent with the melting study, the ligands **Phen-Et** and **Phen-Pr** have higher binding affinity and specificity for the *c-MYC* quadruplex over telomeric and duplex DNAs (Figure S7C and D, Supporting Information).

***Taq* Polymerase Stop Assay.** Ligand-induced stability of the quadruplex DNA was further probed using a *Taq* polymerase stop assay.[73,74] Here templates containing the *c-MYC* quadruplex forming sequence and nonquadruplex forming sequence (mutated *c-MYC* DNA in which one G was replaced by A) were used. In the absence of ligand at 55 °C, *Taq* polymerase was able to extend the primer into a full length product when the *c-MYC* quadruplex forming template was used (Figure 6, Figures S8 and S9, Supporting Information). However, in the presence of the ligand, the quadruplex structure present in the template is stabilized, due to which *Taq* polymerase was unable to unwind this stable quadruplex to get a full length product. Hence, instead of a full length product, there was stop product at the quadruplex forming site in the presence of the ligand. A plot of the percentage of the stop product versus concentration of the ligand used furnishes the IC_{50} values (Figure S10, Supporting Information). The ligands **Nap-Et** and **Nap-Pr** showed IC_{50} values of ∼0.8 μM and ∼7.2 μM; phenanthroline based ligands, **Phen-Et** and **Phen-Pr**, showed IC_{50} values of ∼1.0 μM and ∼0.5 μM, respectively (Figure S10, Supporting Information). In the case of pyridine based ligands, **Py-Et** and **Py-Pr**, a full length product was observed even at 100 μM (Figure S9, Supporting Information) due to the poor stabilization of quadruplexes by them. It should be noted that in the case of **Nap-Et**, at a high concentration (3 μM), pausing sites were observed not only in the quadruplex forming site but also in the primer-template site due to its binding to single/double stranded DNA (Figure S8A, Supporting Information). Similar results were also observed for the potent ligands such as telomestatin and amidoanthroquinone (BSU-1051).[73,43]

DOI: 10.1021/cb5008597
ACS Chem. Biol. XXXX, XXX, XXX−XXX

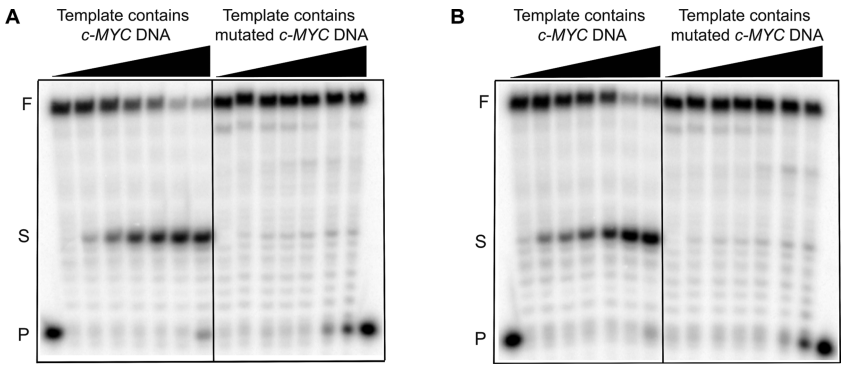

Figure 6. Denaturing PAGE (15%, 7 M urea) of primer-extension stop assay by *Taq* polymerase. Template sequence contains quadruplex forming *c-MYC* DNA and nonquadruplex forming mutated *c-MYC* DNA (100 nM template, 50 nM primer, 0.2 mM dNTPs, and 0.5 U *Taq* polymerase). (A) **Phen-Et** (0, 0.25, 0.5, 1, 2, 4, and 8 μM). (B) **Phen-Pr** (0, 0.1, 0.2, 0.3, 0.5, 1, and 2 μM). F, S, and P denote a full length product, a stop product at the quadruplex forming site, and a primer, respectively. Extension of the primer by *Taq* polymerase at 55 °C leads to a full length product in the absence of a ligand, whereas in the presence of the ligands, which stabilize the quadruplex, extension is paused at the quadruplex forming site.

The template sequence containing a nonquadruplex forming region (mutated *c-MYC*) was also studied under identical conditions to evaluate any nonspecific binding of the ligands (Figure 6). Results indicate that all ligands, except **Nap-Et**, showed no effect on the mutated DNA, which further substantiates that inhibition of the primer extension is quadruplex mediated and the ligands have a higher binding affinity for the quadruplex over single and double stranded DNAs. In the case of **Nap-Et**, pausing sites were observed due to its nonspecific binding to single or double stranded DNA (Figure S8A, Supporting Information). Overall, the IC_{50} values are well in agreement with CD melting data of *c-MYC* quadruplex DNA, where **Phen-Pr** imparted the highest stabilization (ΔT_m = 20.7 °C) and showed the lowest IC_{50} value (~0.5 μM).

Molecular Modeling and Dynamics Studies. Molecular dynamics (MD) simulation studies were carried out to decipher the structural basis of ligand specificity in binding and stabilizing the promoter G-quadruplex over the telomeric G-quadruplex and ds DNAs. The ligands were energy optimized at the B3LYP/6-311G** level in Gaussian 09,[75] and optimized geometries showed that conformational freedom of the ligands was strictly restricted by two intramolecular hydrogen bonds between N atoms in the aromatic core and H atoms in the amide group linking the side chains (Figure S11, Supporting Information). Molecular docking studies were performed using Glide with the energy optimized structures of **Phen-Et** and **Phen-Pr** ligands with *c-MYC* (PDB entry: 1XAV),[19] telomeric parallel (PDB entry: 1KF1),[76] hybrid (PDB entry: 2MB3),[67] and antiparallel (PDB entry: 143D)[77] G-quadruplex structures. All of the docked structures showed the top G-quartet as the preferred binding site for the ligands. The docked structures were subjected to 100 ns of unrestrained MD simulations using the AMBER 12 package.[78] A generalized AMBER force field[79] and FF12SB were used for the ligand and DNA, respectively.

Binding free energies for all G-quadruplex–ligand complexes were estimated using the MM-PB/GBSA method.[80] The total binding free energy (ΔG, Table 2, Tables S1–S3, Supporting Information) clearly showed that **Phen-Et** and **Phen-Pr** have higher selectivity/specificity toward the parallel *c-MYC* quadruplex (~ −61 to −66 kcal mol^{-1}) over the telomeric (~ −12 to −42 kcal mol^{-1}) and duplex (~ −14 to −20 kcal mol^{-1}) DNAs. Results also highlight that **Phen-Et** is more specific than **Phen-Pr** toward *c-MYC* over telomeric quadruplex DNA.

Table 2. Binding Free Energy (ΔG, kcal mol^{-1}) at 300 K for G-Quadruplex and ds DNA with Each Ligand Estimated Using MM-PB/GBSA in AMBER 12

structures	Phen-Et	Phen-Pr
c-MYC (1XAV)	−61.67 ± 3.4[a]	−66.65 ± 4.2
telomeric antiparallel (143D)	−35.57 ± 6.7	−42.38 ± 6.7
telomeric hybrid (2MB3)	−12.13 ± 3.7	−42.28 ± 5.2
dsDNA	−14.47 ± 5.2	−20.00 ± 2.9

[a]Standard deviation of the ΔG values calculated from 100 ns of MD simulations.

It should be noted that there exist major structural differences between *c-MYC* and telomeric quadruplex topologies. The telomeric parallel and *c-MYC* structure contain only propeller loops, whereas the telomeric antiparallel structure contains two lateral and one diagonal loop, and the hybrid structure contains two lateral and one propeller loop.[19,67,77] These diverse loop conformations and their orientation of the sugar phosphate backbone could make differences in the binding sites for G-quadruplex interacting ligands. The MD snapshot for the **Phen-Et** and **Phen-Pr** with the *c-MYC* quadruplex unveiled that the G-quartet surface along with the reoriented 5′ flanking nucleotides create a well-defined binding site (Figure 7).[68] As a result, ligands were able to stack on top of all four guanines present in the quartet of *c-MYC* DNA. The MD snapshot of **Phen-Et** with the telomeric antiparallel G-quadruplex showed only the central phenanthroline ring stacked onto the G-quartet, while two benzimidazole side chains were away from the G-quartet surface (Figure S12, Supporting Information). However, the MD snapshot of the telomeric hybrid G-quadruplex DNA and ligands revealed that **Phen-Pr** stacks well on top of the G-quartet (Figure S13, Supporting Information). In addition, both ligands in the presence of telomeric antiparallel G-quadruplex DNA underwent energetically unfavorable amide bond rotations during the course of MD simulations (Figure S12, Supporting Information). Interestingly, **Phen-Et** and **Phen-Pr** retained their energy optimized conformation during the course of dynamics, when they bound to *c-MYC* G-quadruplex DNA (Figure S14, Supporting Information). Overall, these results suggest that **Phen-Et**, which has a shorter side chain than **Phen-Pr**, could

DOI: 10.1021/cb5008597
ACS Chem. Biol. XXXX, XXX, XXX–XXX

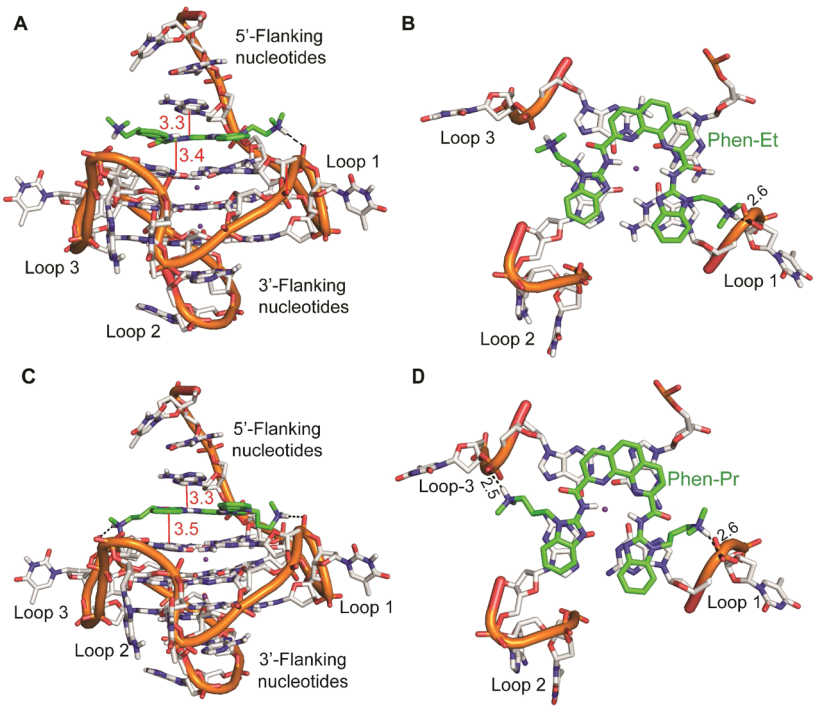

Figure 7. Final MD snapshot of **Phen-Et** and **Phen-Pr** with *c-MYC* G-quadruplex DNA after 100 ns simulations. (A) **Phen-Et** bound to the *c-MYC* quadruplex (side view). (B) **Phen-Et** stacks onto the 5′-quartet and makes electrostatic interactions with the loops (axial view). (C) **Phen-Pr** bound to the *c-MYC* quadruplex (side view). (D) **Phen-Pr** stacks onto the 5′-quartet and makes electrostatic interaction with loops (axial view). The red lines indicate the distance between nucleobases and ligand; black dotted lines denote the electrostatic interactions between ligands and DNA. The phosphate backbone and nucleosides are represented in cartoon and stick representations, respectively. The K^+ ions are shown as purple spheres. All of the distances are in Å.

impart higher specificity toward *c-MYC* G-quadruplex DNA over telomeric G-quadruplex topologies. The differences in binding preference of the ligands toward different topologies imply that the intrinsic flexibility of the flanking nucleotides in *c-MYC*, which is lacking in telomeric DNA, should be considered for the design of topology specific G-quadruplex stabilizing ligands.[66]

To unveil the link between the length of side chains and observed quadruplex specificity, the distances between the protonated side chains in the ligands and phosphate groups present in the loop of G-quadruplex DNA were probed. One of the N-protonated side chains of **Phen-Et** and the phosphate backbone of the propeller loop of the *c-MYC* G-quadruplex forms electrostatic interactions, as the distance between them was found to be 2.6 ± 0.5 Å (Figure 7A and B). Such interaction was not observed in the other protonated side chain of **Phen-Et**. In the case of **Phen-Pr**, both N-protonated side chains were in close contact (∼2.6 Å) with the phosphate backbone of the propeller loops, favoring electrostatic interactions (Figure 7C and D). Conversely, the distance between the protonated side chains and phosphate group in the diagonal and lateral loop of telomeric G-quadruplex structures was ∼8.2 Å, deterring **Phen-Et** to form favorable electrostatic interactions (Figure S15, Supporting Information). Contrarily, one of the N-protonated side chains of **Phen-Pr** was located at a distance of ∼3.2 Å from the negatively charged phosphate backbone of lateral and diagonal loops present in telomeric quadruplex structures, thus favoring electrostatic interactions (Figure S15, Supporting Information). These results validate that the length of the side chains plays a critical role in discriminating between various quadruplex topologies.

To further understand the role of noncovalent interactions of ligand binding to G-quadruplex DNAs, the presence of stacking and electrostatic interactions was probed at each picosecond (ps) during the course of 100 ns of MD simulations. For electrostatic interactions, a cutoff distance of ≤3.5 Å was considered between positively charged N-protonated side chains of the ligand and the negatively charged DNA backbone. Similarly, for the analysis of stacking interactions, the distance of ≤3.5 Å between the ligand and G-quartet was considered along with a ±10° vector angle of the planes. In the case of **Phen-Et** and **Phen-Pr** ligands with the *c-MYC* G-quadruplex, both the electrostatic and stacking interactions were found to be present ∼85% of the total simulation time (Table S4, Supporting Information). The combined effect of these two noncovalent interactions facilitates the ligands to form a stable complex with *c-MYC* G-quadruplex DNA. Interestingly, **Phen-Et** with telomeric antiparallel quadruplex structure showed that electrostatic and stacking interactions were present only ∼45% and ∼39% of the simulation time, respectively. In the case of the telomeric hybrid structure, **Phen-Et** exhibited the stacking and electrostatic interactions during ∼8% and ∼6% of the simulation time, respectively, (Table S4, Supporting Information). However, **Phen-Pr** with the human telomeric antiparallel and hybrid G-quadruplex showed the presence of both interactions more than ∼50% of the simulation time. The low prevalence of these noncovalent interactions between the ligands and telomeric quadruplex topologies accounts for their weak stabilizing effects observed in the experiments. Additionally, energetics of $\pi-\pi$ stacking[81] of quadruplex−ligand complexes were computed at the MP2/6-31G* (0.25) level in Gaussian 09 (Table 3 and Table S5, Supporting Information). For the stacking energy calculations, the

DOI: 10.1021/cb5008597
ACS Chem. Biol. XXXX, XXX, XXX−XXX

Table 3. Difference in the Stacking Energy of G-Quadruplex DNA in the Geometry of Ligand Unbound State and Bound State Calculated at MP2/6-31G*(0.25) Level (kcal mol^{-1}) in Gaussian 09

structures	*c-MYC* G-quadruplex (PDB entry: 1XAV)	telomeric antiparallel G-quadruplex (PDB entry: 143D)	telomeric hybrid G-quadruplex (PDB entry: 2MB3)
Phen-Et	−20.80	−3.73	−3.70
Phen-Pr	−22.51	−9.76	−10.89

structures of the original G-quadruplex and the structures obtained after 100 ns of MD simulation with ligands were utilized. The difference in the stacking energy of the two structures is shown in Table 3. The results clearly show that the ligands have better stacking affinity with *c-MYC* G-quadruplex DNA over telomeric DNA topologies. Additionally, stacking energy calculations reveal that **Phen-Et** is more specific toward the *c-MYC* quadruplex than **Phen-Pr**.

The conformational stability of the quadruplex−ligand complexes was analyzed using 1D and 2D RMSD maps. The RMSD analysis of G-quartets and ligands showed all atoms were within 1.5 Å during the course of 100 ns MD simulations in quadruplex−ligand complexes (Figures S16−S18, Supporting Information). The 5′-flanking nucleotides (RMSD = 2.8 ± 0.5 Å) in the *c-MYC* G-quadruplex underwent a global conformational change to accommodate the ligands in such a way as to maximize their interactions with G-quartets (Table S6, Supporting Information). Contrarily, two nucleotides from the 3′-flanking trinucleotides (RMSD = 1.8 ± 0.3 Å) of the *c-MYC* quadruplex stacked rigidly to the bottom of the G-quartet. The ligand **Phen-Et** did not form a rigid complex with the telomeric hybrid G-quadruplex as evidenced from the higher RMSD of the lateral loop (RMSD = 2.4 ± 0.8 Å) and ligand (RMSD = 3.1 ± 0.4 Å). Such deviations were not observed for **Phen-Pr** and telomeric hybrid G-quadruplex DNA (Table S6, Supporting Information). Furthermore, the two-dimensional RMSD maps of quadruplex−ligand complexes validate the conformational flexibility of **Phen-Et** with telomeric quadruplex structures during the course of MD simulations (Figure S19−S21, Supporting Information).

It has been reported that the binding preference of a ligand to a particular G-quadruplex topology or structure depends on its ability to maximize the available accessible surface area in the receptor quadruplex structure.[82] To delineate this aspect, solvent accessible surface area (SASA) of the quadruplex over the 100 ns of MD simulation was calculated for the quadruplex−ligand complexes using the Surf tool in AMBER 12. The normalized frequency of SASA during the course of simulation was analyzed (Figure S22, Supporting Information). The **Phen-Et** and **Phen-Pr** accessed the large surface area of the *c-MYC* G-quadruplex with a ΔSASA of 238 Å^2 and 253 Å^2, respectively (Figure 8). However, for the **Phen-Et**, ΔSASAs with the telomeric antiparallel and hybrid were found to be only 173 Å^2 and 169 Å^2, respectively. The difference in the ΔSASA between the parallel *c-MYC* and telomeric G-quadruplex topology is around 60 Å^2; therefore the ligands favor the *c-MYC* G-quadruplex over telomeric DNA topologies. The ability of a ligand to access the surface area of the DNA solely depends on the quadruplex topology. The ligands were able to reorient the 5′-flanking nucleotides in *c-MYC*, but not lateral or diagonal loops present in telomeric DNA topologies. However, it has been reported that strong stabilizing agents like telomestatin (ΔSASA = 225 Å^2) and naphthalene diimides (ΔSASA = 210 Å^2) were able to efficiently reorient the nucleobases present in the loops of telomeric G-quadruplex structures.[28,36,67,82]

MD dynamics and simulations (100 ns) were also extended to rationalize the inability of the ligands to stabilize or induce telomeric parallel topology as evidenced from the CD studies. The final MD snapshot of **Phen-Et** with telomeric parallel G-quadruplex DNA showed that the **Phen-Et** did not stack well onto the G-quartet surface (Figure S23, Supporting Information). Moreover, the N-protonated side chains in **Phen-Et** failed to form electrostatic interactions with the backbone of the propeller loop as the distance between them was found to be 10.2 Å, which led to flexibility of the ligand side chains as evidenced from the RMSD graphs (Figures S24 and S25, Supporting Information). The average RMSD of the loops of parallel quadruplex DNA was around 2.8 Å over 100 ns of MD simulations, which indicated the conformational flexibility of the propeller loops. Furthermore, the two-dimensional RMSD map of the G-quadruplex−**Phen-Et** complex illustrated the formation of an unstable complex during the MD simulations. Also, the presences of electrostatic and stacking interactions was found to be ∼5% and ∼12% of the 100 ns of the simulation time, respectively. The very low prevalence of electrostatic interactions was due to the lengthy (three nucleotides) and flexible propeller loops in the telomeric DNA in comparison to the shorter (one and two nucleotides) and rigid propeller loops

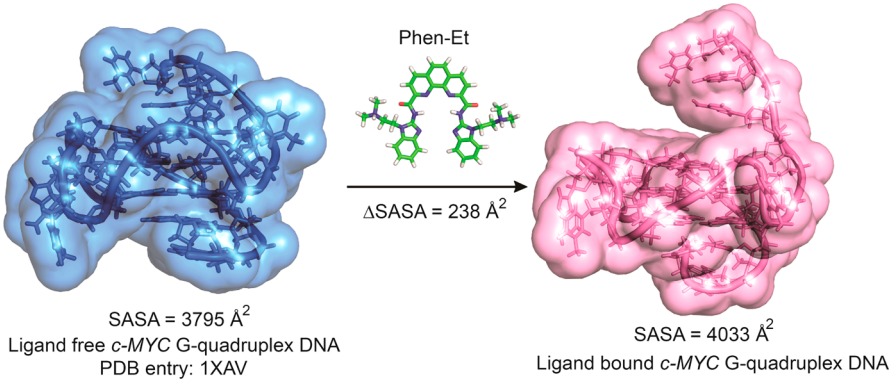

Figure 8. Comparison of solvent accessible surface area (SASA) between native and **Phen-Et** bound *c-MYC* quadruplex DNAs. ΔSASA = (SASA of **Phen-Et** bound *c-MYC* quadruplex complex) − (SASA of native *c-MYC* quadruplex DNA). SASA of **Phen-Et** bound *c-MYC* complex was calculated after 100 ns of MD simulations.

DOI: 10.1021/cb5008597
ACS Chem. Biol. XXXX, XXX, XXX−XXX

in *c-MYC* G-quadruplex DNA. Overall, the data clearly show that the ligand **Phen-Et** forms only a less stable complex with telomeric parallel G-quadruplex DNA, which accounts for the binding energy of -18.63 ± 3.2 kcal mol^{-1} observed for the complex (Table S7, Supporting Information).

The selectivity of **Phen-Et** and **Phen-Pr** ligands toward G-quadruplex DNAs over dsDNA was also explored by MD simulations. The final MD snapshot of the dsDNA and ligand (Figure S26, Supporting Information), binding energy values (Table 2 and Table S8, Supporting Information), and RMSD graphs (Figure S27, Supporting Information) indicated that ligands have significantly low binding affinity toward dsDNA. Overall, MD simulation studies, SASA analysis, and stacking energy calculations shed light on how the specificity was achieved by the **Phen-Et** and **Phen-Pr** ligands toward parallel G-quadruplex topology adopted by promoter DNAs.

Conclusions. We have designed and synthesized bisbenzimidazole carboxamide derivatives of pyridine, 1,8-naphthyridine, and 1,10-phenanthroline to specifically stabilize promoter quadruplexes over telomeric and duplex DNAs. Our studies showed that both the aromatic π surface area of the central core and appropriately positioned *N*-alkyl benzimidazole side chains with suitable length of the ligands play a crucial role in discriminating promoter quadruplexes from telomeric DNA. As a result, phenanthroline-based ligands having larger surface area compared to their pyridine and naphthyridine counterparts imparted high specificity toward promoter quadruplexes. Among **Phen-Et** and **Phen-Pr**, the former having an ethyl side chain emerged as the lead compound due to its inability to interact with the loops of telomeric DNA, reflecting the specific stabilization of promoter quadruplexes (ΔT_m = ~16−18 °C) over telomeric DNA (ΔT_m = 1 °C). In particular, the ligand has imparted only marginal stability to any of the telomeric DNA topological forms (antiprallel, parallel, hybrid, or higher order forms). NMR and CD titration studies showed that the ligand bound to the *c-MYC* quadruplex via end stacking and upon binding the parallel topology of the *c-MYC* quadruplex was retained. UV−vis titrations studies further validated the fact that the ligand specifically bound (K_b ~6×10^4 M^{-1}) to *c-MYC* quadruplex DNA. Furthermore, the *Taq* polymerase stop assay showed that the ligand was able to arrest the primer extension (IC_{50} ~ 1.0 μM) by stabilizing the *c-MYC* quadruplex structure present in the template. Molecular modeling and dynamics studies revealed that the length of the flexible *N*,*N*-dimethyl aminoethyl side chains present in the ligand was optimal in targeting propeller loops of the *c-MYC* quadruplex to establish electrostatic interactions. In addition, the ligands, by reorienting 5′ flanking nucleotides of the *c-MYC* quadruplex, maximize the accessible surface area for favorable stacking interactions with the G-quartet of the *c-MYC* quadruplex, accounting for the specificity of the ligands toward the *c-MYC* quadruplex over telomeric quadruplex structures.

Overall, this study underscores the importance of the flexible side chains in the ligands, which should be taken into consideration for the design of structure-specific quadruplex stabilizing agents. In this context, it should be noted that even when the accurate three-dimensional structure of various G-quadruplex DNA topologies is available, right now, there is no well-established methodology to design or identify the structure-specific ligands based on minor structural differences in each quadruplex topology. Therefore, the benzimidazole scaffolds reported here represent potent and powerful side chains to engineer the quadruplex specific ligands. Systematic explorations and screening of these side chains by attaching a suitable central core having drug-like properties can lead to the evolution of next generation ligands, which may find applications in quadruplex DNA based therapeutics. Furthermore, these topology specific ligands could also be utilized along with quadruplex specific antibodies for potential applications in visualizing promoter quadruplex DNAs in the cellular environment.

■ ASSOCIATED CONTENT

Ⓢ Supporting Information

Experimental procedures, CD melting and titrations curves, UV−vis absorption spectra, polymerase stop assay, additional results from molecular modeling and dynamics studies, and copies of NMR spectra. This material is available free of charge via the Internet at http://pubs.acs.org.

■ AUTHOR INFORMATION

Corresponding Authors

*E-mail: dhamodharan@chem.iitb.ac.in.
*E-mail: pradeep@chem.iitb.ac.in.

Notes

The authors declare no competing financial interest.

■ ACKNOWLEDGMENTS

We are thankful to Professor D. A. Case for waiving off the licensing fee for AMBER 12; Dr. S. Srivastava and Ms. M. Joshi, National Facility for High-Field NMR, TIFR-Mumbai, for their assistance with NMR titrations; Dr. R. Anand for providing access to her laboratory facilities. Computer center, IIT Bombay and NPSF-CDAC, Pune are gratefully acknowledged for providing high performance computing facilities. This work was financially supported by a grant from Department of Atomic Energy−Board of Research in Nuclear Sciences (DAE-BRNS), Government of India (grant no: 2012/37C/4/BRNS-1063). V.D. thanks CSIR and IRCC-IIT Bombay, and S.H. thanks DAE-BRNS for the fellowships.

■ DEDICATION

Dedicated to Professor Jyoti Chattopadhyaya on the occasion of his 65th birthday.

■ REFERENCES

(1) Burge, S., Parkinson, G. N., Hazel, P., Todd, A. K., and Neidle, S. (2006) Quadruplex DNA: sequence, topology and structure. *Nucleic Acids Res. 34*, 5402−5415.

(2) Patel, D. J., Phan, A. T., and Kuryavyi, V. (2007) Human telomere, oncogenic promoter and 5′-UTR G-quadruplexes: Diverse higher order DNA and RNA targets for cancer therapeutics. *Nucleic Acids Res. 35*, 7429−7455.

(3) Huppert, J. L., and Balasubramanian, S. (2007) G-quadruplexes in promoters throughout the human genome. *Nucleic Acids Res. 35*, 406−413.

(4) Mukundan, V. T., and Phan, A. T. (2013) Bulges in G-Quadruplexes: Broadening the Definition of G-Quadruplex-Forming Sequences. *J. Am. Chem. Soc. 135*, 5017−5028.

(5) Biffi, G., Tannahill, D., McCafferty, J., and Balasubramanian, S. (2013) Quantitative visualization of DNA G-quadruplex structures in human cells. *Nat. Chem. 5*, 182−186.

(6) Biffi, G., Di Antonio, M., Tannahill, D., and Balasubramanian, S. (2014) Visualization and selective chemical targeting of RNA G-quadruplex structures in the cytoplasm of human cells. *Nat. Chem. 6*, 75−80.

DOI: 10.1021/cb5008597
ACS Chem. Biol. XXXX, XXX, XXX−XXX

(7) Henderson, A., Wu, Y., Huang, Y. C., Chavez, E. A., Platt, J., Johnson, F. B., Brosh, R. M., Sen, D., and Lansdorp, P. M. (2014) Detection of G-quadruplex DNA in mammalian cells. *Nucleic Acids Res. 42*, 860−869.
(8) Paeschke, K., Bochman, M. L., Garcia, P. D., Cejka, P., Friedman, K. L., Kowalczykowski, S. C., and Zakian, V. A. (2013) Pif1 family helicases suppress genome instability at G-quadruplex motifs. *Nature 497*, 458−462.
(9) Zahler, A. M., Williamson, J. R., Cech, T. R., and Prescott, D. M. (1991) Inhibition of telomerase by G-quartet DMA structures. *Nature 350*, 718−720.
(10) Balasubramanian, S., Hurley, L. H., and Neidle, S. (2011) Targeting G-quadruplexes in gene promoters: a novel anticancer strategy? *Nat. Rev. Drug Discovery 10*, 261−275.
(11) Kumari, S., Bugaut, A., Huppert, J. L., and Balasubramanian, S. (2007) An RNA G-quadruplex in the 5′ UTR of the NRAS proto-oncogene modulates translation. *Nat. Chem. Biol. 3*, 218−221.
(12) Arora, A., Dutkiewicz, M., Scaria, V., Hariharan, M., Maiti, S., and Kurreck, J. (2008) Inhibition of translation in living eukaryotic cells by an RNA G-quadruplex motif. *RNA 14*, 1290−1296.
(13) Bidzinska, J., Cimino-Reale, G., Zaffaroni, N., and Folini, M. (2013) G-Quadruplex Structures in the Human Genome as Novel Therapeutic Targets. *Molecules 18*, 12368−12395.
(14) Rodriguez, R., Miller, K. M., Forment, J. V., Bradshaw, C. R., Nikan, M., Britton, S., Oelschlaegel, T., Xhemalce, B., Balasubramanian, S., and Jackson, S. P. (2012) Small-molecule-induced DNA damage identifies alternative DNA structures in human genes. *Nat. Chem. Biol. 8*, 301−310.
(15) Neidle, S. (2010) Human telomeric G-quadruplex: The current status of telomeric G-quadruplexes as therapeutic targets in human cancer. *FEBS J. 277*, 1118−1125.
(16) McLuckie, K. I. E., Di Antonio, M., Zecchini, H., Xian, J., Caldas, C., Krippendorff, B.-F., Tannahill, D., Lowe, C., and Balasubramanian, S. (2013) G-Quadruplex DNA as a Molecular Target for Induced Synthetic Lethality in Cancer Cells. *J. Am. Chem. Soc. 135*, 9640−9643.
(17) Brooks, T. A., Kendrick, S., and Hurley, L. (2010) Making sense of G-quadruplex and i-motif functions in oncogene promoters. *FEBS J. 277*, 3459−3469.
(18) Agarwal, T., Roy, S., Chakraborty, T. K., and Maiti, S. (2010) Selective Targeting of G-Quadruplex Using Furan-Based Cyclic Homooligopeptides: Effect on *c-MYC* Expression. *Biochemistry 49*, 8388−8397.
(19) Ambrus, A., Chen, D., Dai, J., Jones, R. A., and Yang, D. (2005) Solution Structure of the Biologically Relevant G-Quadruplex Element in the Human *c-MYC* Promoter. Implications for G-Quadruplex Stabilization. *Biochemistry 44*, 2048−2058.
(20) Phan, A. T., Kuryavyi, V., Burge, S., Neidle, S., and Patel, D. J. (2007) Structure of an unprecedented G-quadruplex scaffold in the human c-kit promoter. *J. Am. Chem. Soc. 129*, 4386−4392.
(21) Hsu, S.-T. D., Varnai, P., Bugaut, A., Reszka, A. P., Neidle, S., and Balasubramanian, S. (2009) A G-Rich Sequence within the c-kit Oncogene Promoter Forms a Parallel G-Quadruplex Having Asymmetric G-Tetrad Dynamics. *J. Am. Chem. Soc. 131*, 13399−13409.
(22) Agrawal, P., Hatzakis, E., Guo, K., Carver, M., and Yang, D. (2013) Solution structure of the major G-quadruplex formed in the human *VEGF* promoter in K+: insights into loop interactions of the parallel G-quadruplexes. *Nucleic Acids Res. 41*, 10584−10592.
(23) Tong, X., Lan, W., Zhang, X., Wu, H., Liu, M., and Cao, C. (2011) Solution structure of all parallel G-quadruplex formed by the oncogene *RET* promoter sequence. *Nucleic Acids Res. 39*, 6753−6763.
(24) De Armond, R., Wood, S., Sun, D. Y., Hurley, L. H., and Ebbinghaus, S. W. (2005) Evidence for the presence of a guanine quadruplex forming region within a polypurine tract of the hypoxia inducible factor 1 alpha promoter. *Biochemistry 44*, 16341−16350.
(25) Buscaglia, R., Miller, M. C., Dean, W. L., Gray, R. D., Lane, A. N., Trent, J. O., and Chaires, J. B. (2013) Polyethylene glycol binding alters human telomere G-quadruplex structure by conformational selection. *Nucleic Acids Res. 41*, 7934−7946.
(26) Hänsel, R., Löhr, F., Trantirek, L., and Dötsch, V. (2013) High-Resolution Insight into G-Overhang Architecture. *J. Am. Chem. Soc. 135*, 2816−2824.
(27) Haensel, R., Loehr, F., Foldynova-Trantirkova, S., Bamberg, E., Trantirek, L., and Doetsch, V. (2011) The parallel G-quadruplex structure of vertebrate telomeric repeat sequences is not the preferred folding topology under physiological conditions. *Nucleic Acids Res. 39*, 5768−5775.
(28) Luu, K. N., Phan, A. T., Kuryavyi, V., Lacroix, L., and Patel, D. J. (2006) Structure of the human telomere in K+ solution: An intramolecular (3 + 1) G-quadruplex scaffold. *J. Am. Chem. Soc. 128*, 9963−9970.
(29) Phan, A. T., Kuryavyi, V., Luu, K. N., and Patel, D. J. (2007) Structure of two intramolecular G-quadruplexes formed by natural human telomere sequences in K+ solution. *Nucleic Acids Res. 35*, 6517−6525.
(30) Petraccone, L., Spink, C., Trent, J. O., Garbett, N. C., Mekmaysy, C. S., Giancola, C., and Chaires, J. B. (2011) Structure and Stability of Higher-Order Human Telomeric Quadruplexes. *J. Am. Chem. Soc. 133*, 20951−20961.
(31) Luedtke, N. W. (2009) Targeting G-Quadruplex DNA with Small Molecules. *Chimia 63*, 134−139.
(32) Ou, T.-m., Lu, Y.-j., Tan, J.-h., Huang, Z.-s., Wong, K.-Y., and Gu, L.-q. (2008) G-quadruplexes: Targets in anticancer drug design. *ChemMedChem 3*, 690−713.
(33) Mohanty, J., Barooah, N., Dhamodharan, V., Harikrishna, S., Pradeepkumar, P. I., and Bhasikuttan, A. C. (2013) Thioflavin T as an Efficient Inducer and Selective Fluorescent Sensor for the Human Telomeric G-Quadruplex DNA. *J. Am. Chem. Soc. 135*, 367−376.
(34) Webba da Silva, M. (2007) Geometric Formalism for DNA Quadruplex Folding. *Chem.—Eur. J. 13*, 9738−9745.
(35) Campbell, N. H., Patel, M., Tofa, A. B., Ghosh, R., Parkinson, G. N., and Neidle, S. (2009) Selectivity in Ligand Recognition of G-Quadruplex Loops. *Biochemistry 48*, 1675−1680.
(36) Haider, S. M., Neidle, S., and Parkinson, G. N. (2011) A structural analysis of G-quadruplex/ligand interactions. *Biochimie 93*, 1239−1251.
(37) Xue, L., Ranjan, N., and Arya, D. P. (2011) Synthesis and Spectroscopic Studies of the Aminoglycoside (Neomycin)-Perylene Conjugate Binding to Human Telomeric DNA. *Biochemistry 50*, 2838−2849.
(38) Sparapani, S., Haider, S. M., Doria, F., Gunaratnam, M., and Neidle, S. (2010) Rational Design of Acridine-Based Ligands with Selectivity for Human Telomeric Quadruplexes. *J. Am. Chem. Soc. 132*, 12263−12272.
(39) Di Leva, F. S., Zizza, P., Cingolani, C., D'Angelo, C., Pagano, B., Amato, J., Salvati, E., Sissi, C., Pinato, O., Marinelli, L., Cavalli, A., Cosconati, S., Novellino, E., Randazzo, A., and Biroccio, A. (2013) Exploring the Chemical Space of G-Quadruplex Binders: Discovery of a Novel Chemotype Targeting the Human Telomeric Sequence. *J. Med. Chem. 56*, 9646−9654.
(40) Hamon, F., Largy, E., Guédin-Beaurepaire, A., Rouchon-Dagois, M., Sidibe, A., Monchaud, D., Mergny, J.-L., Riou, J.-F., Nguyen, C.-H., and Teulade-Fichou, M.-P. (2011) An Acyclic Oligoheteroaryle That Discriminates Strongly between Diverse G-Quadruplex Topologies. *Angew. Chem., Int. Ed. 50*, 8745−8749.
(41) Nicoludis, J. M., Miller, S. T., Jeffrey, P. D., Barrett, S. P., Rablen, P. R., Lawton, T. J., and Yatsunyk, L. A. (2012) Optimized End-Stacking Provides Specificity of N-Methyl Mesoporphyrin IX for Human Telomeric G-Quadruplex DNA. *J. Am. Chem. Soc. 134*, 20446−20456.
(42) Di Antonio, M., Biffi, G., Mariani, A., Raiber, E.-A., Rodriguez, R., and Balasubramanian, S. (2012) Selective RNA Versus DNA G-Quadruplex Targeting by In Situ Click Chemistry. *Angew. Chem., Int. Ed. 51*, 11073−11078.
(43) Seenisamy, J., Bashyam, S., Gokhale, V., Vankayalapati, H., Sun, D., Siddiqui-Jain, A., Streiner, N., Shin-ya, K., White, E., Wilson, W. D., and Hurley, L. H. (2005) Design and Synthesis of an Expanded

DOI: 10.1021/cb5008597
ACS Chem. Biol. XXXX, XXX, XXX−XXX

Porphyrin That Has Selectivity for the *c-MYC* G-Quadruplex Structure. *J. Am. Chem. Soc. 127*, 2944−2959.
(44) Jantos, K., Rodriguez, R., Ladame, S., Shirude, P. S., and Balasubramanian, S. (2006) Oxazole-Based Peptide Macrocycles: A New Class of G-Quadruplex Binding Ligands. *J. Am. Chem. Soc. 128*, 13662−13663.
(45) McLuckie, K. I. E., Waller, Z. A. E., Sanders, D. A., Alves, D., Rodriguez, R., Dash, J., McKenzie, G. J., Venkitaraman, A. R., and Balasubramanian, S. (2011) G-Quadruplex-Binding Benzo[a]-phenoxazines Down-Regulate c-KIT Expression in Human Gastric Carcinoma Cells. *J. Am. Chem. Soc. 133*, 2658−2663.
(46) Bejugam, M., Sewitz, S., Shirude, P. S., Rodriguez, R., Shahid, R., and Balasubramanian, S. (2007) Trisubstituted Isoalloxazines as a New Class of G-Quadruplex Binding Ligands: Small Molecule Regulation of c-kit Oncogene Expression. *J. Am. Chem. Soc. 129*, 12926−12927.
(47) Chauhan, A., Paladhi, S., Debnath, M., Mandal, S., Das, R. N., Bhowmik, S., and Dash, J. (2014) A small molecule peptidomimetic that binds to *c-KIT1* G-quadruplex and exhibits antiproliferative properties in cancer cells. *Bioorg. Med. Chem. 22*, 4422−4429.
(48) Jain, A. K., and Bhattacharya, S. (2011) Interaction of G-Quadruplexes with Nonintercalating Duplex-DNA Minor Groove Binding Ligands. *Bioconjugate Chem. 22*, 2355−2368.
(49) Bhattacharya, S., Chaudhuri, P., Jain, A. K., and Paul, A. (2010) Symmetrical Bisbenzimidazoles with Benzenediyl Spacer: The Role of the Shape of the Ligand on the Stabilization and Structural Alterations in Telomeric G-Quadruplex DNA and Telomerase Inhibition. *Bioconjugate Chem. 21*, 1148−1159.
(50) Jain, A. K., Paul, A., Maji, B., Muniyappa, K., and Bhattacharya, S. (2012) Dimeric 1,3-Phenylene-bis(piperazinyl benzimidazole)s: Synthesis and Structure−Activity Investigations on their Binding with Human Telomeric G-Quadruplex DNA and Telomerase Inhibition Properties. *J. Med. Chem. 55*, 2981−2993.
(51) Wang, P., Leung, C.-H., Ma, D.-L., Yan, S.-C., and Che, C.-M. (2010) Structure-Based Design of Platinum(II) Complexes as c-myc Oncogene Down-Regulators and Luminescent Probes for G-Quadruplex DNA. *Chem.—Eur. J. 16*, 6900−6911.
(52) Largy, E., Hamon, F., Rosu, F., Gabelica, V., De Pauw, E., Guédin, A., Mergny, J.-L., and Teulade-Fichou, M.-P. (2011) Tridentate N-Donor Palladium(II) Complexes as Efficient Coordinating Quadruplex DNA Binders. *Chem.—Eur. J. 17*, 13274−13283.
(53) Li, G., Huang, J., Zhang, M., Zhou, Y., Zhang, D., Wu, Z., Wang, S., Weng, X., Zhou, X., and Yang, G. (2008) Bis(benzimidazole)-pyridine derivative as a new class of G-quadruplex inducing and stabilizing ligand. *Chem. Commun.*, 4564−4566.
(54) Pennarun, G., Granotier, C., Gauthier, L. R., Gomez, D., and Boussin, F. D. (2005) Apoptosis related to telomere instability and cell cycle alterations in human glioma cells treated by new highly selective G-quadruplex ligands. *Oncogene 24*, 2917−2928.
(55) Dhamodharan, V., Harikrishna, S., Jagadeeswaran, C., Halder, K., and Pradeepkumar, P. I. (2012) Selective G-quadruplex DNA Stabilizing Agents Based on Bisquinolinium and Bispyridinium Derivatives of 1,8-Naphthyridine. *J. Org. Chem. 77*, 229−242.
(56) De Cian, A., DeLemos, E., Mergny, J.-L., Teulade-Fichou, M.-P., and Monchaud, D. (2007) Highly Efficient G-Quadruplex Recognition by Bisquinolinium Compounds. *J. Am. Chem. Soc. 129*, 1856−1857.
(57) Larsen, A. F., Nielsen, M. C., and Ulven, T. (2012) Tetrasubstituted Phenanthrolines as Highly Potent, Water-Soluble, and Selective G-Quadruplex Ligands. *Chem.—Eur. J. 18*, 10892−10902.
(58) Gracie, K., Dhamodharan, V., Pradeepkumar, P. I., Faulds, K., and Graham, D. (2014) Qualitative SERS analysis of G-quadruplex DNAs using selective stabilising ligands. *Analyst 139*, 4458−4465.
(59) Monchaud, D., Yang, P., Lacroix, L., Teulade-Fichou, M.-P., and Mergny, J.-L. (2008) A metal-mediated conformational switch controls G-quadruplex binding affinity. *Angew. Chem., Int. Ed. 47*, 4858−4861.
(60) Seth, P. P., Robinson, D. E., Jefferson, E. A., and Swayze, E. E. (2002) Efficient solution phase synthesis of 2-(N-acyl)-amino-benzimidazoles. *Tetrahedron Lett. 43*, 7303−7306.
(61) Guédin, A., Lacroix, L., and Mergny, J.-L. (2010) Thermal Melting Studies of Ligand DNA Interactions, In *Drug-DNA Interaction Protocols* (Fox, K. R., Ed.), pp 25−35, Humana Press.
(62) Xue, Y., Kan, Z.-y., Wang, Q., Yao, Y., Liu, J., Hao, Y.-h., and Tan, Z. (2007) Human Telomeric DNA Forms Parallel-Stranded Intramolecular G-Quadruplex in K+ Solution under Molecular Crowding Condition. *J. Am. Chem. Soc. 129*, 11185−11191.
(63) Singh, V., Azarkh, M., Drescher, M., and Hartig, J. S. (2012) Conformations of individual quadruplex units studied in the context of extended human telomeric DNA. *Chem. Commun. 48*, 8258−8260.
(64) Rezler, E. M., Seenisamy, J., Bashyam, S., Kim, M. Y., White, E., Wilson, W. D., and Hurley, L. H. (2005) Telomestatin and diseleno sapphyrin bind selectively to two different forms of the human telomeric G-quadruplex structure. *J. Am. Chem. Soc. 127*, 9439−9447.
(65) Dash, J., Shirude, P. S., Hsu, S.-T. D., and Balasubramanian, S. (2008) Diarylethynyl Amides That Recognize the Parallel Conformation of Genomic Promoter DNA G-Quadruplexes. *J. Am. Chem. Soc. 130*, 15950−15956.
(66) Dai, J., Carver, M., Hurley, L. H., and Yang, D. (2011) Solution Structure of a 2:1 Quindoline−*c-MYC* G-Quadruplex: Insights into G-Quadruplex-Interactive Small Molecule Drug Design. *J. Am. Chem. Soc. 133*, 17673−17680.
(67) Chung, W. J., Heddi, B., Tera, M., Iida, K., Nagasawa, K., and Phan, A. T. (2013) Solution Structure of an Intramolecular (3 + 1) Human Telomeric G-Quadruplex Bound to a Telomestatin Derivative. *J. Am. Chem. Soc. 135*, 13495−13501.
(68) Chung, W. J., Heddi, B., Hamon, F., Teulade-Fichou, M.-P., and Phan, A. T. (2014) Solution Structure of a G-quadruplex Bound to the Bisquinolinium Compound Phen-DC3. *Angew. Chem., Int. Ed. 53*, 999−1002.
(69) Ma, D.-L., Chan, D. S.-H., Fu, W.-C., He, H.-Z., Yang, H., Yan, S.-C., and Leung, C.-H. (2012) Discovery of a Natural Product-Like c-*myc* G-Quadruplex DNA Groove-Binder by Molecular Docking. *PLoS One 7*, e43278.
(70) Yaku, H., Murashima, T., Miyoshi, D., and Sugimoto, N. (2010) Anionic phthalocyanines targeting G-quadruplexes and inhibiting telomerase activity in the presence of excessive DNA duplexes. *Chem. Commun. 46*, 5740−5742.
(71) Kieltyka, R., Englebienne, P., Moitessier, N., and Sleiman, H. (2010) Quantifying Interactions Between G-Quadruplex DNA and Transition-Metal Complexes, In *G-Quadruplex DNA* (Baumann, P., Ed.), pp 223−255, Humana Press.
(72) Koirala, D., Dhakal, S., Ashbridge, B., Sannohe, Y., Rodriguez, R., Sugiyama, H., Balasubramanian, S., and Mao, H. (2011) A single-molecule platform for investigation of interactions between G-quadruplexes and small-molecule ligands. *Nat. Chem. 3*, 782−787.
(73) Han, H., Hurley, L. H., and Salazar, M. (1999) A DNA polymerase stop assay for G-quadruplex-interactive compounds. *Nucleic Acids Res. 27*, 537−542.
(74) Sun, D., and Hurley, L. (2010) Biochemical Techniques for the Characterization of G-Quadruplex Structures: EMSA, DMS Footprinting, and DNA Polymerase Stop Assay, In *G-Quadruplex DNA* (Baumann, P., Ed.), pp 65−79, Humana Press.
(75) Frisch, M., Trucks, G. W., Schlegel, H. B., Scuseria, G. E., Robb, M. A., Cheeseman, J. R., Scalmani, G., Barone, V., Mennucci, B., and Petersson, G. A. (2009) *Gaussian 09*, revision A.02, Gaussian, Inc., Wallingford, CT.
(76) Parkinson, G. N., Lee, M. P. H., and Neidle, S. (2002) Crystal structure of parallel quadruplexes from human telomeric DNA. *Nature 417*, 876−880.
(77) Wang, Y., and Patel, D. J. (1993) Solution structure of the human telomeric repeat d[AG3(T2AG3)3] G-tetraplex. *Structure 1*, 263−282.
(78) Case, D., Darden, T., Cheatham, T., III, Simmerling, C., Wang, J., Duke, R., Luo, R., Walker, R., Zhang, W., and Merz, K. (2012) *AMBER 12*, University of California, San Francisco.
(79) Wang, J. M., Wolf, R. M., Caldwell, J. W., Kollman, P. A., and Case, D. A. (2004) Development and testing of a general amber force field. *J. Comput. Chem. 25*, 1157−1174.

DOI: 10.1021/cb5008597
ACS Chem. Biol. XXXX, XXX, XXX−XXX

(80) Kollman, P. A., Massova, I., Reyes, C., Kuhn, B., Huo, S. H., Chong, L., Lee, M., Lee, T., Duan, Y., Wang, W., Donini, O., Cieplak, P., Srinivasan, J., Case, D. A., and Cheatham, T. E. (2000) Calculating structures and free energies of complex molecules: Combining molecular mechanics and continuum models. *Acc. Chem. Res. 33*, 889−897.
(81) Lech, C. J., Heddi, B., and Phan, A. T. (2013) Guanine base stacking in G-quadruplex nucleic acids. *Nucleic Acids Res. 41*, 2034−2046.
(82) Haider, S. M., Autiero, I., and Neidle, S. (2011) Surface area accessibility and the preferred topology of telomeric DNA quadruplex−ligand complexes. *Biochimie 93*, 1275−1279.

DOI: 10.1021/cb5008597
ACS Chem. Biol. XXXX, XXX, XXX−XXX

Supporting Information

Topology Specific Stabilization of Promoter over Telomeric G-Quadruplex DNAs by Bisbenzimidazole Carboxamide Derivatives

V. Dhamodharan,[‡] S. Harikrishna,[‡] Achikanath C. Bhasikuttan,[§] P. I. Pradeepkumar*[,‡]

[‡]*Department of Chemistry, Indian Institute of Technology Bombay, Powai, Mumbai 400076, India.*
[§]*Radiation & Photochemistry Division, Bhabha Atomic Research Centre, Mumbai 400 085, India*
Email: pradeep@chem.iitb.ac.in

TABLE OF CONTENTS

Preparation of ligand side chains

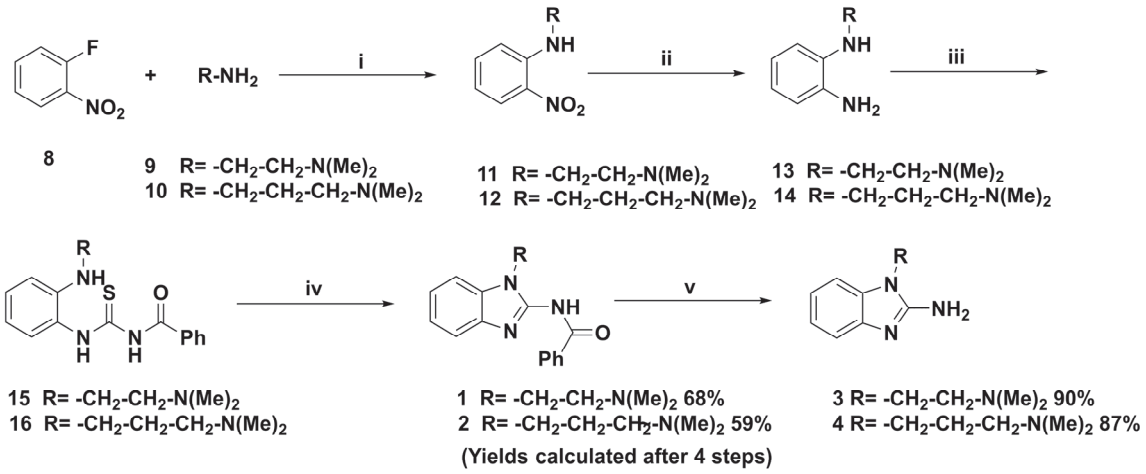

Scheme S1. Preparation of benzimidazole side chains.
Reagents and conditions: (i) K_2CO_3, DCM, rt, 24 h; (ii) H_2, Pd(10%)/C, EtOH, rt, 5 h; (iii) PhCONCS, DCM, rt, 20 h; (iv) EDC.HCl, DIPEA, DCM, rt, 24 h; (v) CH_3NH_2-EtOH, 80 °C, 4 d.

Experimental

General: All chemicals/reagents and solvents were obtained from commercial sources. DCM, Et_3N and DIPEA were dried using calcium hydride. Thin-layer chromatography (TLC) was performed on silica gel plates pre-coated with fluorescent indicator with visualization by UV light (254 nm). Silica gel (100−200 mesh) was used for column chromatography. ^{1}H NMR (400 MHz), ^{13}C NMR (100MHz) and ^{19}F NMR (376.5 MHz) were recorded on a 400 MHz Bruker NMR instrument. The chemical shifts in parts per million were referenced to TMS signal or the residual proton signal of deuterium solvents: TMS (0 ppm) or CD_3OD (3.31 ppm) for ^{1}H NMR spectra, and $CDCl_3$ (77.2 ppm) or CD_3OD (49.1 ppm) for ^{13}C NMR spectra. Multiplicities of ^{1}H NMR spin couplings are reported as s (singlet), br s (broad singlet), d (doublet), t (triplet), q (quartet), dd (doublet of doublets), or m (multiplet and overlapping spin systems). Values for apparent coupling constants (*J*) are reported in Hz. High- resolution mass spectra (HRMS) were obtained in positive ion electrospray ionization (ESI) mode using a Q-TOF analyzer.

***N*-(1-(2-(dimethylamino)ethyl)-1H-benzo[d]imidazol-2-yl)benzamide (1).** This compound was prepared using procedure reported previously[1] with slight modification. To a stirring solution of compound **8** (0.5 ml, 4.74 mmol), K_2CO_3 (1.63 g, 11.79 mmol) in dry DCM (8 ml) was added compound **9** (0.56 ml, 5.12 mmol). The stiring was continued for 24 h. Then water (20 ml) was added to the

reaction mixture and this solution was extracted with DCM (2×40 ml). The combined organic layer was dried over anhydrous Na_2SO_4, and concentrated under reduced pressure to yield yellow liquid compound **11** (990 mg, 4.73 mmol). This compound was dissolved in EtOH (20 ml), then Pd(10%)/C (100 mg) was added and stirred for 5 h under H_2 atmosphere. The reaction mixture then was passed through celite pad and the filtrate was evaporated to afford the compound **13** as brown solid (700 mg, 3.90 mmol). This compound was dissolved in dry DCM (15 ml) and kept in ice bath under N_2 atmosphere. To this cold solution, benzoylisothiocyante (0.53 ml, 3.94 mmol) was added and the ice cold temperature was maintained for 2 h. The reaction mixture was further stirred for 18 h at room temperature. To this reaction mixture, EDC.HCl (750 mg, 3.91 mmol) and DIPEA (2.7 ml, 15.5 mmol) were added and the stirring was continued for 24 h at room temperature. After completion of the reaction, water (40 ml) was added and the organic phase was extracted with DCM (2×100 ml). The organic phase was dried over Na_2SO_4, evaporated under reduced pressure and purified by column chromatography (40%-50% ethylacetate in petether) to yield compound **1** (1 g, 68% for 4 steps); R_f =0.4 (4% MeOH in DCM); ^{1}H NMR (400MHz , $CDCl_3$) δ 12.42 (br s, 1H), 8.35 (d, J = 6.8 Hz, 2H), 7.52−7.42 (m, 3H), 7.33−7.21 (m, 4H), 4.38 (t, J = 7.2 Hz, 2H), 2.79 (t, J = 7.2 Hz, 2H), 2.39 (s, 6H); ^{13}C NMR (100 MHz, $CDCl_3$) δ 176.4, 153.8, 138.1, 131.3, 129.7, 129.3, 128.6, 128.0, 123.1, 123.0, 111.5, 109.2, 57.1, 45.8, 40.5; HRMS (ESI) calcd for $C_{18}H_{20}N_4ONa$ $(M + Na)^+$ 331.1529 found 331.1530 (Δm +0.0001, error +0.3ppm)

1-(2-(dimethylamino)ethyl)-1H-benzo[d]imidazol-2-amine (3). Compound **1** (1 g, 3.2 mmol) was taken in a sealed tube containing ethanolic methylamine (33% (w/v), 20 ml). The sealed tube was closed by teflon screw cap and it was heated at 80 °C for 4 days. Then the reaction mixture was cooled to room temperature and the solvent was evaporated under reduced pressure. The desired compound was purified by column chromatography (80% ethylacetate in petether + 1% Et_3N) to afford compound **1** (600 mg, 90%); R_f =0.4 (5% MeOH in DCM + 1% Et_3N); ^{1}H NMR (400 MHz, $CDCl_3$) δ 7.42 (d, J = 7.8 Hz, 1H), 7.13−7.01 (m, 3H), 5.98 (br s, 2H), 4.00 (t, J = 4.8 Hz, 2H), 2.70 (t, J = 4.8 Hz, 2H), 2.33 (s, 6H); ^{13}C NMR (100 MHz, $CDCl_3$) δ 155.8, 141.8, 134.3, 121.4, 119.5, 116.0, 107.0, 60.0, 45.7, 41.5; HRMS (ESI) calcd for $C_{11}H_{17}N_4$ $(M + H)^+$ 205.1448 found 205.1446 (Δm −0.0002, error −1.0 ppm)

N-(1-(3-(dimethylamino)propyl)-1H-benzo[d]imidazol-2-yl)benzamide (2). This compound was prepared as reported previously[1] with slight modification. To a stirring solution of compound **8** (1 ml, 9.48 mmol), K_2CO_3 (3.2 g, 23.15 mmol) in dry DCM (15 ml) was added compound **10** (1.3 ml, 10.33

mmol). The stirring was continued for 24 h. Then water (40 ml) was added to the reaction mixture and this solution was extracted with DCM (2×80 ml). The organic layer was dried over anhydrous Na_2SO_4, and concentrated under reduced pressure to yield yellow liquid compound **12** (2.11 g, 9.45 mmol). This compound was dissolved in EtOH (30 ml), then Pd(10%)/C (210 mg) was added and stirred for 5 h under H_2 atmosphere. The reaction mixture was passed through celite pad and the filtrate was evaporated to afford the compound **14** as brown solid (1.7 g, 8.79 mmol). This compound was dissolved in dry DCM (15 ml) and kept in ice bath. To this cold solution, benzoylisothiocyante (1.2 ml, 8.92 mmol) was added and the ice cold temperature was maintained for 2 h. This solution was further stirred for 18 h at room temperature. Then to this reaction mixture, EDC.HCl (1.68 g, 8.76 mmol) and DIPEA (6.1 ml, 35.02 mmol) were added and the stirring was continued for 24 h at room temperature. After completion of the reaction, water (80 ml) was added and the organic phase was extracted with DCM (2×200 ml). The organic layer was dried over Na_2SO_4, evaporated and purified by column chromatography (40%-50% ethylacetate in petether) to yield compound **12** (1.82 g, 59 % for 4 steps). R_f = 0.42 (5% MeOH in DCM). ^{1}H NMR (400 MHz, $CDCl_3$) δ 12.41 (br s, 1H), 8.35 (d, J = 7.2 Hz, 2H), 7.51–7.42 (m, 3H), 7.33 (t, J = 7.9 Hz, 2H), 7.28–7.21 (m, 2H), 4.33 (t, J = 7.0 Hz, 2H), 2.37 (t, J = 6.8 Hz, 4H), 2.24 (s, 6H), 2.10–2.03 (m, 2H); ^{13}C NMR (100 MHz, $CDCl_3$) 176.2, 153.6, 138.2, 131.2, 129.9, 129.3, 128.6, 128.0, 123.0, 122.9,111.5, 109.3, 56.5, 45.5, 40.3, 26.6; HRMS (ESI) calcd for $C_{19}H_{23}N_4O$ $(M + H)^+$ 323.1866 found 323.1866 (Δm 0.0000, error 0.0 ppm)

1-(3-(dimethylamino)propyl)-1H-benzo[d]imidazol-2-amine (4). Compound **2** (1.65 g, 5.11 mmol) was taken in a sealed tube containing ethanolic methylamine (33%, 20 ml). The sealed tube was closed by Teflon screw cap and it was heated at 80 °C for 3 days. Then the reaction mixture was cooled to room temperature and the solvent was evaporated under reduced pressure. The desired compound was purified by column chromatography (80% ethylacetate in petether + 1% Et_3N) to afford compound **4** (980 mg, 87 %); R_f =0.4 (5% MeOH in DCM + 1% Et_3N); ^{1}H NMR (400 MHz, $CDCl_3$) δ 7.41 (d, J = 7.8 Hz, 1H), 7.13–7.02 (m, 3H), 6.08 (br s, 2H), 4.03 (t, J = 6.0 Hz, 2H), 2.24 (s, 6H), 2.21 (t, J = 5.8 Hz, 2H), 2.00–1.94 (m, 2H); ^{13}C NMR (100 MHz, $CDCl_3$) δ 155.9, 142.7, 134.2, 121.2, 119.2, 116.1, 107.2, 53.7, 44.5, 38.8, 26.0. HRMS (ESI) calcd for $C_{12}H_{19}N_4$ $(M + H)^+$ 219.1604 found 219.1605 (Δm +0.0001, error +0.4 ppm)

General procedure for coupling of amine side chains to the Pyridine, Naphthyridine and Phenanthroline carboxylic acid core: To a stirred solution of dicarboxylicacid compound (1 equiv) in

dry DCM under N_2 atm were added the corresponding amine (2 equiv), EDC·HCl (4 equiv), HOBt (0.2equiv), and NMM (15 equiv). The mixture was stirred for 24 h at room temperature and then the reaction mixture was diluted with DCM (100 ml) and washed with saturated $NaHCO_3$ (20 ml x 2) solution followed by brine solution (20 ml). The organic layer was dried over Na_2SO_4 and evaporated to give the semi-solid compound. This amide compound was washed with cold diethyl ether and decanted off to provide solid crude amine. This crude compound was dissolved in DCM (5ml) and 0.5 ml TFA was added stirred for 5 min at room temperature. The excess TFA and solvent were evaporated to dryness and the product was kept in high vacuum for 10 min. The product was precipitated by dissolving minimum volume of MeOH: DCM (1-5:99-95) solvent mixture and addition of excess cold ether. The solvents were decanted to get solid amide compounds in the protonated form.

2,2'-(((pyridine-2,6-dicarbonyl)bis(azanediyl))bis(1H-benzo[d]imidazole-2,1-diyl))bis(N,N-dimethylethan-1-aminium)trifluoroacetate (Py-Et). Pyridine-2,6-dicarboxylic acid **5** (25 mg, 0.149 mmol) in 5 mL of dry DCM, amine compound **1** (61 mg, 0.298 mmol), EDC·HCl (115 mg, 0.599 mmol), HOBt (4 mg, 0.029 mmol), and NMM (0.25 ml, 2.27 mmol) were used to afford **Py-Et** (46 mg, 40% yield); ^{1}H NMR (400 MHz, CD_3OD) δ 8.59 (d, J = 7.2 Hz, 2H), 8.15 (t, J = 7.2 Hz, 1H), 7.61 – 7.59 (m, 4H), 7.41–7.35 (m, 4H), 4.78 (br s, 4H), 3.72 (br s, 4H), 3.16 (s, 12H); ^{13}C NMR (100 MHz, CD_3OD) δ 174.6, 154.8, 154.1, 140.4, 130.3, 127.9, 125.4, 119.8, 116.9, 113.7, 111.2, 57.1, 44.1, 39.1; ^{19}F NMR (376.5 MHz, CD_3OD) δ −76.7; HRMS (ESI) calcd for $C_{29}H_{34}N_9O_2$ $(M + H)^+$ 540.2830 found 540.2828 (Δm −0.0002, error −0.4 ppm)

3,3'-(((pyridine-2,6-dicarbonyl)bis(azanediyl))bis(1H-benzo[d]imidazole-2,1-diyl))bis(N,N-dimethylpropan-1-aminium) trifluoroacetate (Py-Pr). Pyridine-2,6-dicarboxylic acid **5** (25 mg, 0.149 mmol) in 5 mL of dry DCM, amine compound **2** (66 mg, 0.302 mmol), EDC·HCl (115 mg, 0.599 mmol), HOBt (4 mg, 0.029 mmol), and NMM (0.25 ml, 2.27 mmol) were used to yield **Py-Pr** (44 mg, 37% yield). ^{1}H NMR (400 MHz, CD_3OD) δ 8.70 (d, J = 7.6 Hz, 2H), 8.24 (t, J = 7.6 Hz, 1H), 7.62 (t, J = 6.8 Hz, 4H), 7.44 –7.37 (m, 4H), 4.57 (t, J = 6.0 Hz , 4H), 3.29 (t, J = 8.0 Hz, 4H), 2.90 (s, 12H), 2.43–2.36 (m, 4H); ^{13}C NMR (100 MHz, CD_3OD) δ 174.4, 154.6, 153.7, 140.8, 130.6, 128.0, 125.4, 119.8, 116.9, 113.6, 111.3, 56.0, 43.5, 40.5, 25.2; ^{19}F NMR (376.5 MHz, CD_3OD) δ −72.7; HRMS (ESI) calcd for $C_{31}H_{38}N_9O_2$ $(M + H)^+$ 568.3143 found 568.3142 (Δm −0.0001, error −0.2 ppm)

2,2'-(((1,8-naphthyridine-2,7-dicarbonyl)bis(azanediyl))bis(1H-benzo[d]imidazole-2,1-

diyl))bis(N,N-dimethylethan-1-aminium)trifluoroacetate (Nap-Et). 1,8-naphthyridine-2,7-dicarboxylic acid[2] **6** (40 mg, 0.183 mmol) in 10 mL of dry DCM, amine compound **1** (75 mg, 0.367 mmol), EDC·HCl (141 mg, 0.735 mmol), HOBt (5 mg, 0.037 mmol), and NMM (0.3 ml, 2.72 mmol) were used to afford **Nap-Et** (52 mg, 34% yield). ^{1}H NMR (400 MHz, CD_3OD) δ 8.51–8.47 (m, 4H), 7.49–7.41 (m, 4H), 7.25 (br s, 4H), 4.80 (br s, 4H), 3.95 (br s, 4H), 3.33 (s, 12H); ^{13}C NMR (100 MHz, CD_3OD) δ 172.9, 158.6, 154.9, 154.2, 139.5, 130.1, 129.9, 125.0, 124.9, 124.2, 116.9, 113.2, 110.9, 57.7, 44.4, 39.1; ^{19}F NMR (376.5 MHz, CD_3OD) δ −76.9; HRMS (ESI) calcd for $C_{32}H_{35}N_{10}O_2$ $(M + H)^+$ 591.2944 found 591.2939 (Δm −0.0005, error −0.9 ppm)

3,3'-(((1,8-naphthyridine-2,7-dicarbonyl)bis(azanediyl))bis(1H-benzo[d]imidazole-2,1-diyl))bis(N,N-dimethylpropan-1-aminium)trifluoroacetate (Nap-Pr). 1,8-naphthyridine-2,7-dicarboxylic acid[2] **6** (40 mg, 0.183 mmol) in 10 mL of dry DCM, amine compound **2** (80 mg, 0.366 mmol), EDC·HCl (141 mg, 0.735 mmol), HOBt (5 mg, 0.037 mmol), and NMM (0.3 ml, 2.72 mmol) were used to afford **Nap-Pr** (92 mg, 59% yield). ^{1}H NMR (400 MHz, CD_3OD) δ 8.64 (br s, 4H), 7.59–7.58 (m, 4H), 7.40–7.34 (m, 4H), 4.54 (t, J = 5.7 Hz, 4H), 3.29 (t, J = 6.8 Hz, 4H), 3.07 (s, 12H), 2.47 (m, 4H); ^{13}C NMR (100 MHz, CD_3OD) δ 172.9, 158.7, 154.9, 153.8, 139.6, 130.2, 129.9, 125.6, 124.9, 124.1, 116.9, 113.4, 110.7, 55.4, 43.7, 40.2, 25.2; ^{19}F NMR (376.5 MHz, CD_3OD) δ −76.8; HRMS (ESI) calcd for $C_{34}H_{39}N_{10}O_2$ $(M + H)^+$ 619.3252 found 619.3257 (Δm +0.0005, error +0.8 ppm)

2,2'-(((1,10-phenanthroline-2,9-dicarbonyl)bis(azanediyl))bis(1H-benzo[d]imidazole-2,1-diyl))bis(N,N-dimethylethan-1-aminium)trifluoroacetate (Phen-Et). 1,10-phenanthroline-2,9-dicarboxylic acid[3] **7** (50 mg, 0.186 mmol) in 10 mL of dry DCM, amine compound **1** (77 mg, 0.376 mmol), EDC·HCl (143 mg, 0.745 mmol), HOBt (5 mg, 0.037 mmol), and NMM (0.3 ml, 2.72 mmol) were used to afford **Phen-Et** (80 mg, 49% yield). ^{1}H NMR (400 MHz, CD_3OD) δ 8.45 (br s, 4H), 8.00 (br s, 2H), 7.53–7.43 (m, 4H), 7.28 (t, J = 8.0 Hz, 2H), 7.17 (br s, 2H), 4.75 (br s, 4H), 3.66 (t, J = 5.3 Hz, 4H), 3.01 (s, 12H); ^{13}C NMR (100 MHz, CD_3OD) δ 173.9, 154.1, 153.6, 145.4, 138.5, 130.9, 129.8, 128.7, 125.0, 124.2, 119.9, 117.0, 113.5, 110.8, 56.2, 44.2, 38.9; ^{19}F NMR (376.5 MHz, CD_3OD) δ −76.4; HRMS (ESI) calcd for $C_{36}H_{37}N_{10}O_2$ $(M + H)^+$ 641.3095 found 641.3093 (Δm –0.0002, error –0.3 ppm)

3,3'-(((1,10-phenanthroline-2,9-dicarbonyl)bis(azanediyl))bis(1H-benzo[d]imidazole-2,1-diyl))bis(N,N-dimethylpropan-1-aminium)trifluoroacetate (Phen-Pr). 1,10-phenanthroline-2,9-dicarboxylic acid[3] **7** (25 mg, 0.093 mmol) in 5 mL of dry DCM, amine compound **2** (41 mg, 0.187

mmol), EDC·HCl (72 mg, 0.375 mmol), HOBt (2.5 mg, 0.018 mmol), and NMM (0.15 ml, 1.36 mmol) were used to afford **Phen-Pr** (35 mg, 41% yield). ^{1}H NMR (400 MHz, CD_3OD) δ 8.32 (br s, 4H), 7.93 (br s, 2H), 7.47–7.08 (m, 8H), 4.41 (br s, 4H), 3.26 (dd, J = 7.7 Hz, 6.4 Hz, 4H), 2.80 (s, 12H), 2.31 (br s, 4H); ^{13}C NMR (100 MHz, CD_3OD) δ 173.7, 154.2, 153.3, 145.0, 138.0, 130.5, 130.0, 128.4, 124.7, 124.1, 120.0, 117.0, 113.3, 110.6, 56.1, 43.6, 40.5, 25.1; ^{19}F NMR (376.5 MHz, CD_3OD) δ −76.7; HRMS (ESI) calcd for $C_{19}H_{21}N_5O$ $((M+2H)/2)^+$ 335.1741, found 335.1748 (Δm +0.0007, error +2.1 ppm).

Oligonucleotides

The following oligonucleotide sequences were used for all experiments: human telomeric DNA sequence (22AG: 5'-AGGGTTAGGGTTAGGGTTAGGG-3'), (long telomeric DNA-Telo46: 5'-AGGGTTAGGGTTAGGGTTAGGG-TT-AGGGTTAGGGTTAGGGTTAGGG-3'); duplex sequence (ds17_1: 5'-CCAGTTCGTAGTAACCC-3'and its complementary sequence, ds17_2 5'-GGGTTACTACGAACTGG-3'), and promoter DNA sequences (*c-KIT1*: 5'-GGGAGGGCGCTGGGAGGAGGG-3'; *c-KIT2*: 5'-GGGCGGGCGCGAGGGAGGGG-3'; *c-MYC*: 5'-TGAGGGTGGGTAGGGTGGGTAA-3'). For *Taq* polymerase stop assay, primer sequence (5'-ACGACTCACTATAGCAATTGCG-3'), template containing *c-MYC* sequence (5'-**TGAGGGTGGGTAGGGTGGGTAA**GCCACCGCAATTGCTATAGTGAGTCGT-3', where bold letters indicate quadruplex forming region), template containing mutated *c-MYC* sequence (5'-TGAGGGTGGGTAG**A**GTGGGTAAGCCACCGCAATTGCTATAGTGAGTCGT-3', where underlined letter is mutated nucleotide) were used. All sequences were synthesized in-house utilizing a Mermade 4 synthesizer and PAGE (20%, 7M urea) purified employing standard protocols. The concentration of all oligonucleotides was measured at 260 nm in UV-Vis spectrophotometer using appropriate molar extinction coefficients (ε).

CD melting and CD titration

Circular dichroism (CD) studies were carried out on a JASCO J-815 spectrometer attached with a peltier temperature controller (model: PTC-423S). The spectra were measured in the wavelength range 220–330 nm using a quartz cuvette with 1.0 mm path length. The scanning speed of the instrument was set to 200 nm/min, and the response time used was 2 s. The strand concentration of oligonucleotide used was 15 μM, and the ligand stock solution used was 10 mM (40% DMSO in water, v/v). The quadruplex DNA solutions (in 100 mM KCl and 10 mM lithium cacodylate buffer, pH 7.2) were annealed by

heating at 95 °C for 5 min and subsequent gradual cooling to room temperature over 2 h. Ligands were titrated in the range 0–4 mol equiv. Each CD spectrum is an average of 3 measurements at 25 °C.

For melting studies, 10-15 μM strand concentration of oligonucleotides in 10 mM lithium cacodylate (pH 7.2), required amount of monovalent salts like LiCl, KCl or NaCl and 3 molar equivalents of ligands (30-45 μM) were used. Human telomeric DNA (10 μM DNA in 10 mM KCl and 90 mM LiCl; or 10 μM DNA in 10 mM KCl, 90 mM LiCl and 40% PEG (v/v); or 10 μM DNA in 50 mM NaCl and 50 mM LiCl), *C-KIT1* (10 μM DNA in 10 mM KCl and 90 mM LiCl), *C-KIT2* (10 μM DNA in 1 mM KCl, and 99 mM LiCl), *c-MYC* quadruplex (10 μM DNA in 1 mM KCl, and 99 mM LiCl), duplex DNA (15 μM ds17_1 and 15 μM ds17_2 in 10 mM KCl and 90 mM LiCl) and long telomeric DNA (10 μM DNA in 100 mM KCl) were annealed by heating at 95 °C for 5 min followed by gradual cooling to room temperature. Thermal melting was monitored at 292 nm, 262 nm and 242 nm for telomeric, promoter and duplex DNAs respectively at the heating rate of 1 °C/min. The melting temperatures (T_m) were determined by sigmoidal curve fit using Boltzmann function in Origin 8.0.

NMR titration

c-MYC DNA (227 μM in 80 mM KCl and 20 mM Potassium phosphate, pH 6.7) was prepared in 10% D_2O in water and 3-(Trimethylsilyl)propanoic acid (TSP) was used as internal standard. Water suppression was achieved by excitation sculpting with gradients technique. **Phen-Et** (20 mM) was prepared in 50% DMSO in water. Spectra were recorded on 800 MHz Bruker instrument at 298 K.

UV-Vis titration

Absorption titration experiments were carried out on a PerkinElmer (Lambda Bio+) instrument. Absorption spectra measured in the range of 225-700 nm using quartz cuvette with 10 mm path length. Initially absorbance of ligand solution (7.5 μM in 100 mM KCl and 10 mM lithium cacodylate, pH 7.2) was measured and titrated with DNA (2-56 μM). After 10 min equilibration time, absorbance of DNA-ligand complex was measured and titration was terminated when 2 or 3 successive additions of DNA gave same absorbance at λ_{max}. Binding constant was derived using following equation as reported previously.[4] Plot of [DNA]/ $\Delta\varepsilon_{ap}$ versus [DNA] provides slope and intercept. Slope is divided by intercept to get binding constant (K_b).

$$[DNA] / \Delta\varepsilon_{ap} = [DNA] / \Delta\varepsilon + 1/ K_b (\Delta\varepsilon)$$

Here, $\Delta\varepsilon_{ap} = |\varepsilon_b - \varepsilon_f|$; ε_b is a molar extinction coefficient of DNA-ligand bound complex and ε_f is molar extinction coefficient of ligand.

^{32}P labelling of primer oligonucleotide

Labelling of oligonucleotide (primer used for stop assay) was carried out as reported previously.[2] Primer oligonucleotide (10 pmol) was incubated with T4 polynucleotide kinase (PNK, 5 U), [γ-32P] ATP (3000 Ci/mmol) and 1 x PNK buffer (50 mM Tris-HCl (pH 7.6), 10 mM $MgCl_2$, 5 mM DTT, 0.1 mM each spermidine and EDTA) in a total volume of 10 µL at 37 °C for 1 h. Then the reaction mixture was heated at 70 °C for 3 min for inactivation of the enzyme. The 5'-labelled primer was purified using a QIAquick nucleotide removal kit employing manufacturer's protocol.

***Taq* DNA polymerase stop assay**

This assay was done as reported previously with slight modifications.[5] Appropriate amount of labeled primer oligonucleotide [~15,000 counts per minute (CPM)] was mixed with cold primer (50 nM) and template (100 nM). They were annealed using an annealing buffer (5 mM Tris pH 7.5, 10 mM NaCl, 0.1 mM EDTA) by heating at 90 °C for 5 min followed by gradual cooling to room temperature over 4 to 5 h.. The annealed primer-template was mixed with polymerase buffer [50 mM Tris pH 7.2, 0.5 mM DTT, 0.1 mM EDTA, 5 mM KCl, 5 mM $MgCl_2$, 1µg/µl BSA] and dNTP (0.2 mM). The ligands in appropriate concentration were added to the reaction mixture (10 µL total volume) and incubated for 30 min at room temperature. The primer extension reaction was initiated by the addition of *Taq* DNA polymerase (0.5 U) and the reactions were incubated at 55 °C for 30 min. The extension reaction was stopped by adding 10 µL of 2 x stop buffer (10 mM EDTA, 10 mM NaOH, 0.1% each bromophenol blue (w/v) and xylene cyanole (w/v) in formamide). The products were analyzed in 15% denaturing PAGE (7M urea) in which 1 x TBE (89 mM of each Tris and boric acid and 2 mM of EDTA, pH 8.3) was used as running buffer. Autoradiograms were generated and bands were quantified by ImageQuantTL software.

Molecular modeling. The NMR structures of human telomeric parallel (PDB entry 1KF1),[6] antiparallel (PDB entry 143D,[7] with pseudointercalation site), hybrid (PDB entry 2MB3)[8] and *c-MYC* (PDB entry 1XAV)[9] G-quadruplex DNAs were downloaded from protein data bank. The duplex DNA d[CCGTACCT TATAGCAGT/GGCATGGAATATCGTCA] was modelled using nucgen module in AMBER 12 and are subsequently energy minimized using 5000 steps of conjugate gradient method. All the receptor structures were minimized (5000 steps of steepest descent) for subsequent grid generation

using the default parameters in protein preparation wizard in Schrödinger LLC.[10] The **Phen-Et** and **Phen-Pr** ligands shown in Figure S10 were optimized at B3LYP/6-311G** level in Gaussian 09.[11] The energy optimized ligands were docked flexibly in to the three different G-quadruplex DNAs and duplex DNA using extra precision (XP) Glide docking method.[12] For each ligand, 30 rounds of docking runs were carried out and upon completion of each round, 100 poses were generated, from which only one pose was automatically filtered out based on glide score. Finally 30 poses were obtained from 30 rounds of docking, and from the 30 poses, the pose with less RMSD threshold of 0.5 – 1.5 Å and lower Glide score (−15 kcal/mol) was taken for MD simulations. The docked pose was then subsequently utilized to calculate the RESP charges in Gaussian 09 and is fitted using antechamber RESP charge fitting procedure.[13]

Utilizing the results obtained from the docking studies, MD simulations were carried out for 8 complexes with the SANDER and PMEMD module in AMBER 12 using the protocol reported by Haider and Neidle.[14] Generalized AMBER force field (GAFF) parameters were used for ligand[15] and G-quadruplex DNAs were parameterized using FF12SB force field. All the complexes were solvated using octahedral TIP3P water box at 10 Å distance from any of the solute, which yielded 6500-7000 water molecules. The charge of the DNA backbone was neutralized using K^+ ions and two ions in the middle of the G-quartet were retained. Water molecules and counter ions were energy minimized by 7000 steepest descent energy minimization and then by conjugate gradient minimization with a convergence of root mean square gradient around 0.1 kcal/mol Å. The entire system was then subjected 20,000 steps of steepest descent and conjugate gradient minimization. After equilibrations (500 – 650 ps), the complexes were subjected to 100 ns of unrestrained MD simulation under constant pressure at 1 atm. The temperature was controlled by Langevin dynamics and was kept constant at 300 K. Electrostatic interactions were taken into account using the Particle Mesh Ewald molecular dynamics (PMEMD) with a cutoff distance of 10 Å. The trajectory files were saved for every 1 ps for further analysis. Binding energy evaluations were carried for each complex was out using MM-PB/GBSA,[16] entropy calculation was done using nmode module available in AMBER 12. The SASA calculations for G-quadruplex DNAs over 100 ns of MD simulations were carried out using Surf module. Trajectories were visually evaluated and their two dimensional RMSD maps were plotted using UCSF Chimera.[17] The hydrogen bond and stacking occupancies between G-quadruplex and ligand was calculated using ptraj module.

Stacking energy between G-quartets was carried out using MP2/6-31G*(0.25) level in Gaussian 09.[18-20] For this, the lowest energy G-quadruplex DNA structures emerged from the 100 ns of MD

simulations performed with the quadruplex-ligand complexes were utilized. The sugar phosphate backbone was excised and their dangling bonds are terminated with hydrogen atoms. To find the ligand induced stacking energy, the experimental structures of ligand free G-quadruplex DNA obtained from protein data bank were utilized. Difference in the stacking energy between the ligand free and ligand bound structure gives the ligand induced stacking energy.

Molecular modeling studies of dsDNA and ligand complexes were performed by following the same procedure used for G-quadruplex and ligand complex. All the figures were rendered using PyMOL v0.99 (http://www.pymol.org).

CD melting curves of promoter quadruplex and duplex DNAs

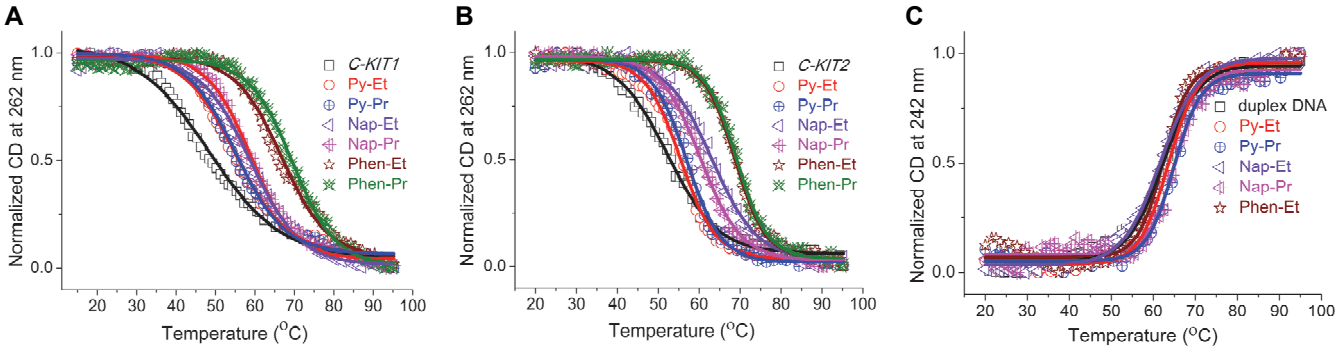

Figure S1. CD melting curves of promoter quadruplexes and duplex DNA in the absence and presence of ligands (3 molar eq.). (A) *c-KIT1* DNA (10 µM in 10 mM lithium cacodylate buffer pH 7.2, 10 mM KCl and 90 mM LiCl). (B) *c-KIT2* DNA (10 µM in 10 mM lithium cacodylate buffer pH 7.2, 1mM KCl and 99 mM LiCl). (C) Duplex DNA (15 µM in 10 mM lithium cacodylate buffer pH 7.2, 10 mM KCl and 90 mM LiCl).

CD melting curves for reference compound 3AQN

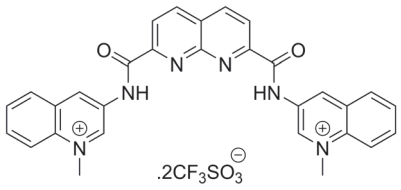

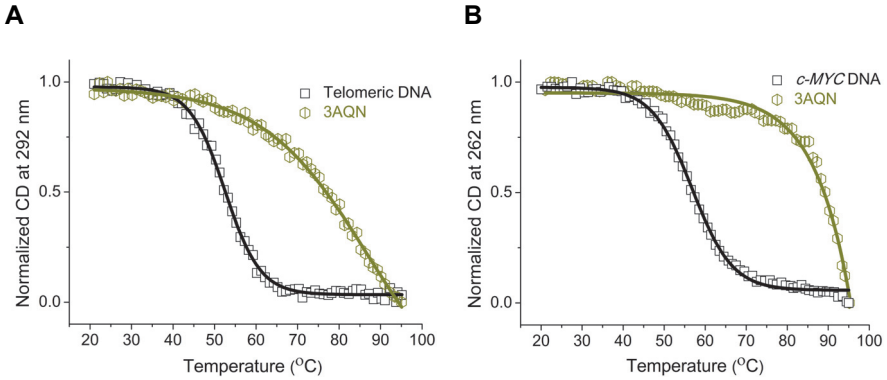

Figure S2. CD melting curves of quadruplex DNA in the presence and absence of **3AQN**. (A) Telomeric DNA (10 µM in 10 mM lithium cacodylate buffer pH 7.2, 10 mM KCl and 90 mM LiCl). (B) *c-MYC* DNA (10 µM in 10 mM lithium cacodylate buffer pH 7.2, 1 mM KCl and 99 mM LiCl).

CD melting curves of telomeric DNAs

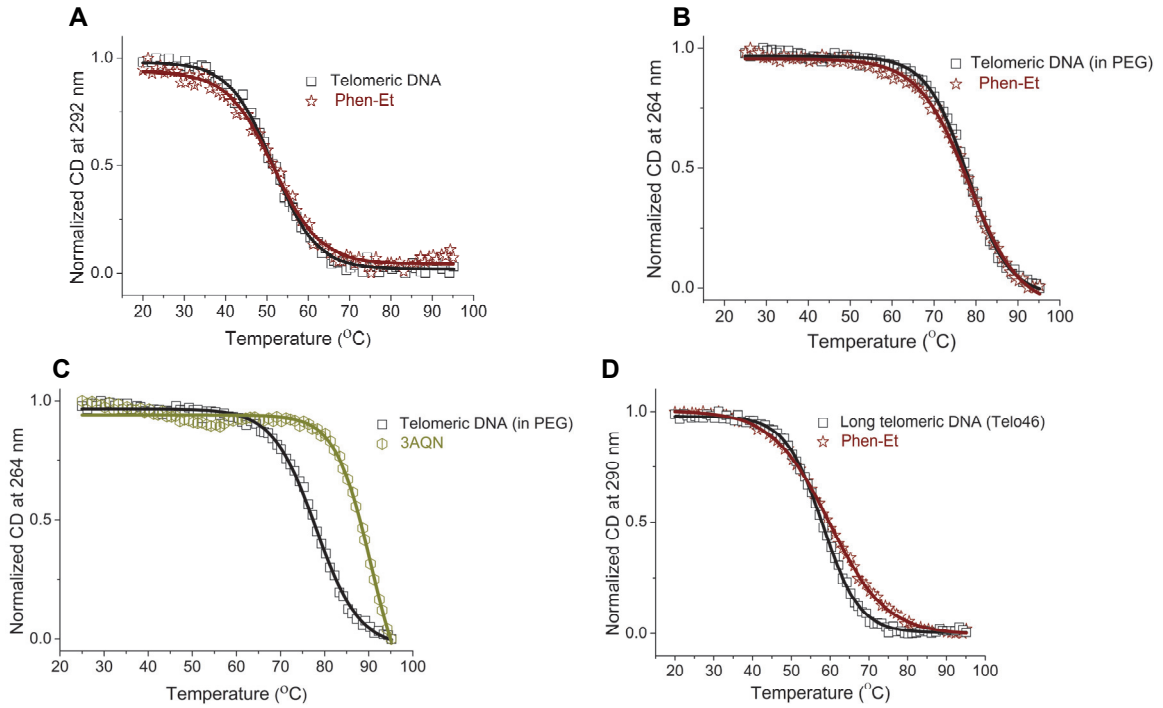

Figure S3. CD melting curves of telomeric DNA (short and long) in various condition in the presence and absence of **Phen-Et** or **3AQN** (3 molar eq.). (A) Telomeric DNA (10 μM in 10 mM lithium cacodylate buffer pH 7.2, 50 mM NaCl and 50 mM LiCl). (B) Telomeric DNA (10 μM in 10 mM lithium cacodylate buffer pH 7.2, 10 mM KCl, 90 mM LiCl and 40% PEG 200 (v/v)). (C) Telomeric DNA (10 μM in 10 mM lithium cacodylate buffer pH 7.2, 10 mM KCl, 90 mM LiCl and 40% PEG 200 (v/v)). (D) Long telomeric DNA (10 μM in 10 mM lithium cacodylate buffer pH 7.2 and 100 mM KCl).

CD titration spectra for promoter and telomeric DNAs in the absence of salts

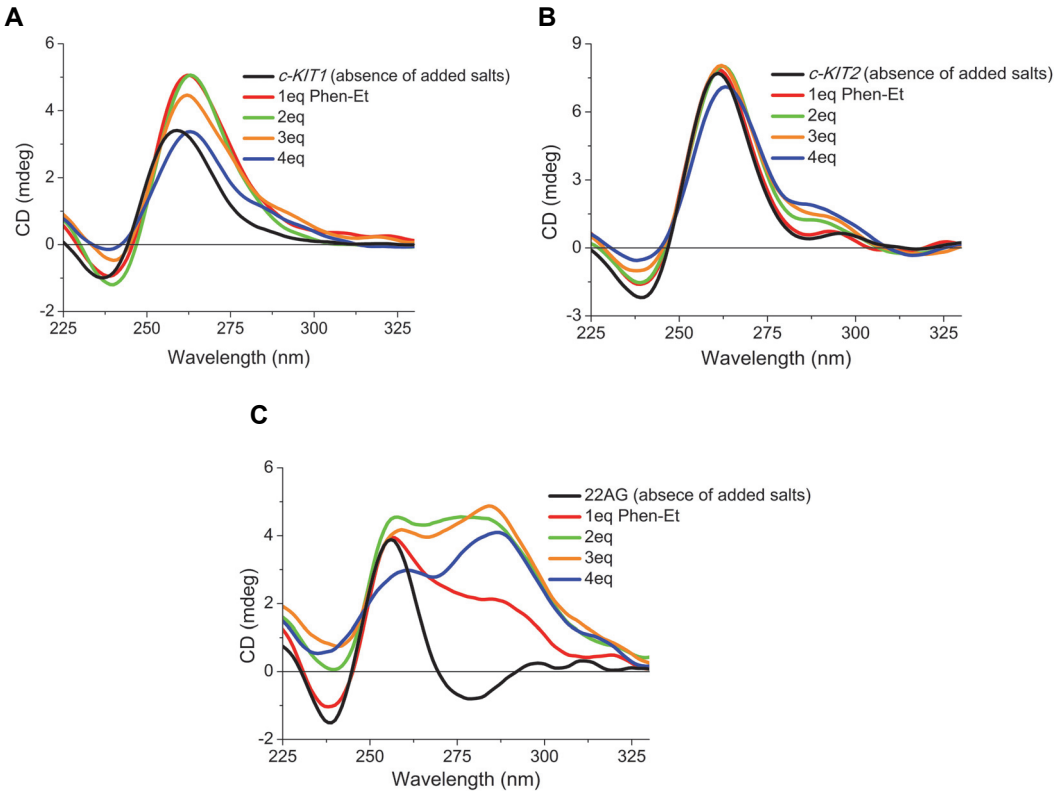

Figure S4. CD spectral changes of quadruplex DNA (15 µM in 10 mM Tris buffer pH 7.2) upon addition of **Phen-Et (**1 to 4 molar eq.). (A) *c-KIT1* DNA. (B) *c-KIT2* DNA. (C) Telomeric DNA.

CD titration spectra for promoter and telomeric DNAs in the presence of salts

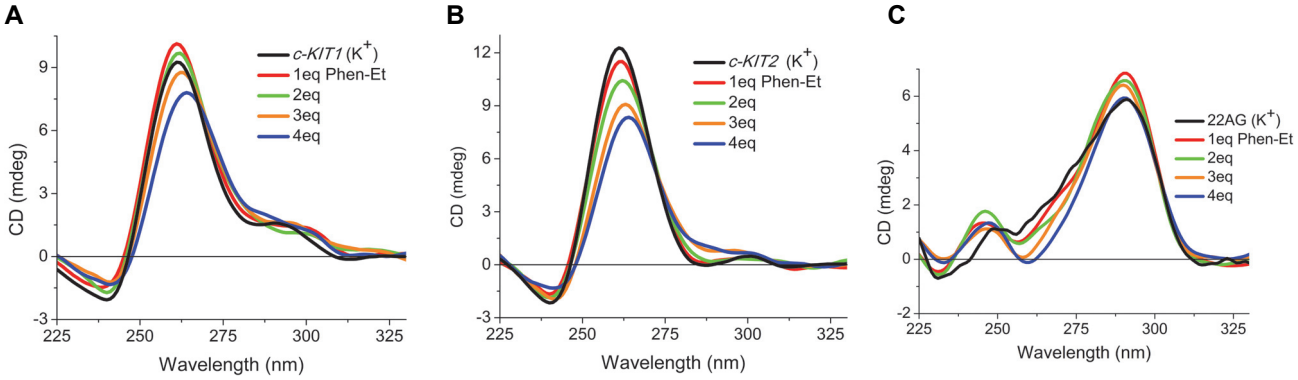

Figure S5. CD spectral changes of quadruplex DNA (15 µM in 100 mM KCl and 10 mM Tris buffer pH 7.2) upon addition of **Phen-Et (**1 to 4 molar eq.). (A) *c-KIT1* DNA. (B) *c-KIT2* DNA. (C) Telomeric DNA.

UV-Vis absorption curves Phen-Et with telomeric and duplex DNAs

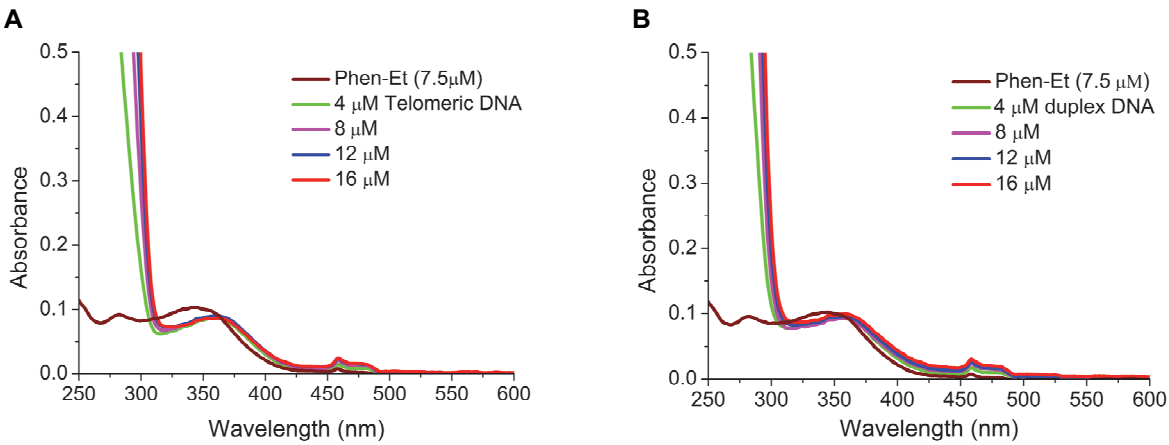

Figure S6. Absorption spectra of **Phen-Et** (7.5 μM in 100 mM KCl and 10 mM lithium cacodylate buffer pH 7.2) with telomeric and duplex DNA (in the identical salt and buffer conditions). (A) Telomeric DNA (4 -16 μM). (B) Duplex DNA (4 -16 μM).

UV-Vis absorption curves Phen-Pr with *c-MYC*, telomeric and duplex DNAs

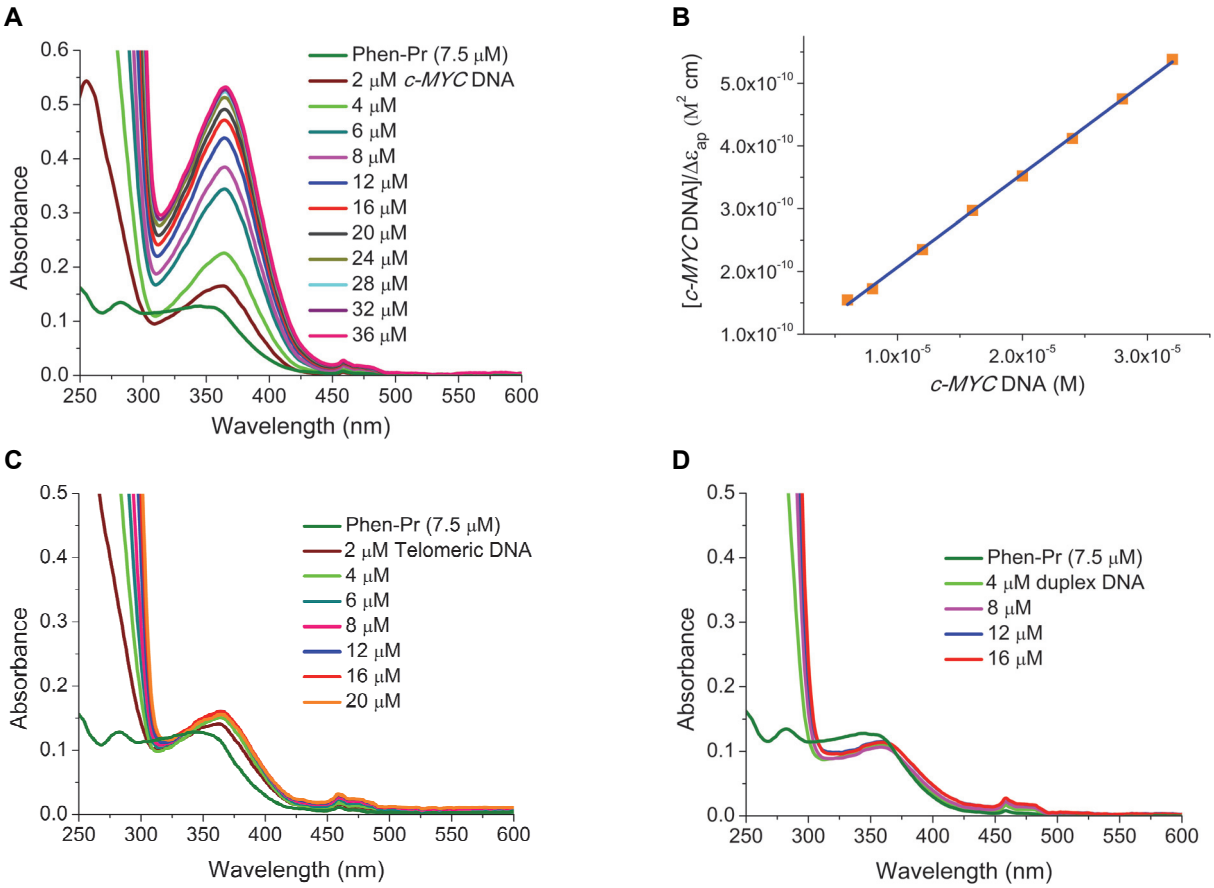

Figure S7. Absorption spectra of **Phen-Pr** (7.5 μM in 100 mM KCl, 10 mM lithium cacodylate buffer pH 7.2) with *c-MYC*, telomeric and duplex DNAs (in the identical salt and buffer conditions). (A) *c-MYC* DNA (2-36 μM). (B) Plot of [*c-MYC* DNA]/$\Delta\varepsilon_{ap}$ versus [*c-MYC* DNA] to calculate the binding constant. (C) Telomeric DNA (2-20 μM). (D) Duplex DNA (4-20 μM).

Denaturing PAGE of primer extension stop assay for Nap-Et and Nap-Pr

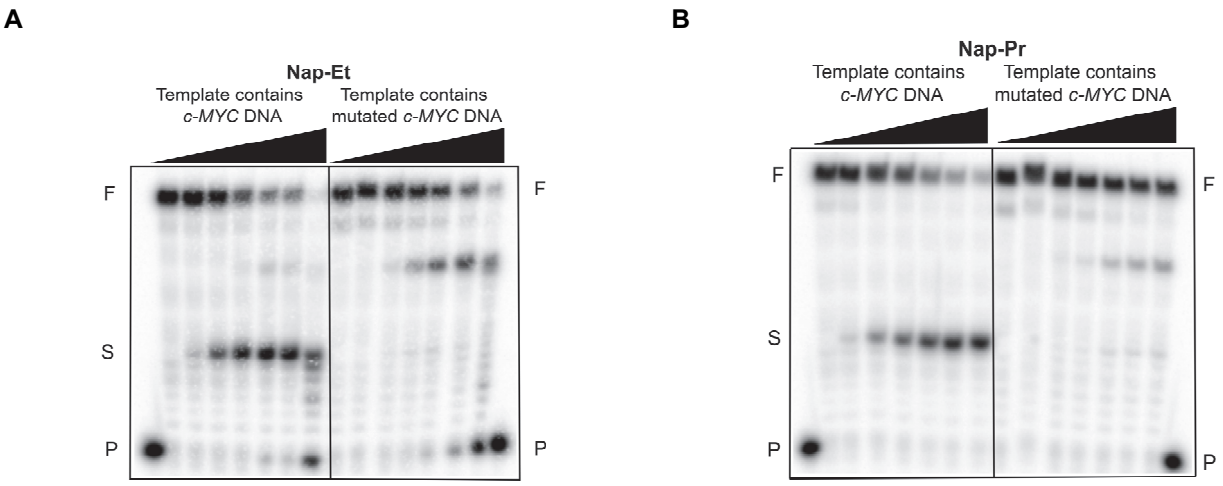

Figure S8. Denaturing PAGE (15%, 7M Urea) of primer-extension stop assay by *Taq* polymerase. Template sequences contain quadruplex forming *c-MYC* DNA and non-quadruplex forming sequence (mutated *c-MYC*). (A) **Nap-Et** (0, 0.25, 0.5, 1.0, 1.5, 2.0 and 3.0 μM). (B) **Nap-Pr** (0, 1.0, 2.0, 4.0, 10, 20 and 30 μM). Conditions: 100 nM template, 50 nM primer, 0.2 mM dNTPs and *Taq* polymerase (0.5 U). F, S and P denote full length product, stop product at quadruplex forming site and primer respectively.

Denaturing PAGE of primer extension stop assay for Py-Et and Py-Pr

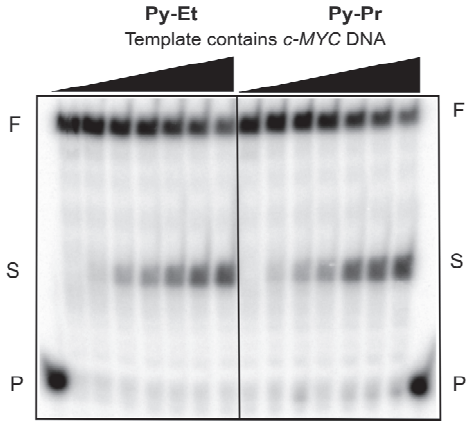

Figure S9. Denaturing PAGE (15%, 7M Urea) of primer-extension stop assay by *Taq* polymerase. Template sequence contains quadruplex forming *c-MYC* DNA. (From left side to right side) **Py-Et** (0, 10, 20, 30, 40, 60 and 100 μM) and **Py-Pr** (0, 10, 20, 30, 40, 60 and 100 μM). Conditions: 100 nM template, 50 nM primer and 0.2 mM dNTPs and *Taq* polymerase (0.5 U). F, S and P denote Full length product, Stop product at quadruplex forming site and Primer respectively.

Plot of stop assay products with respect to ligand concentrations

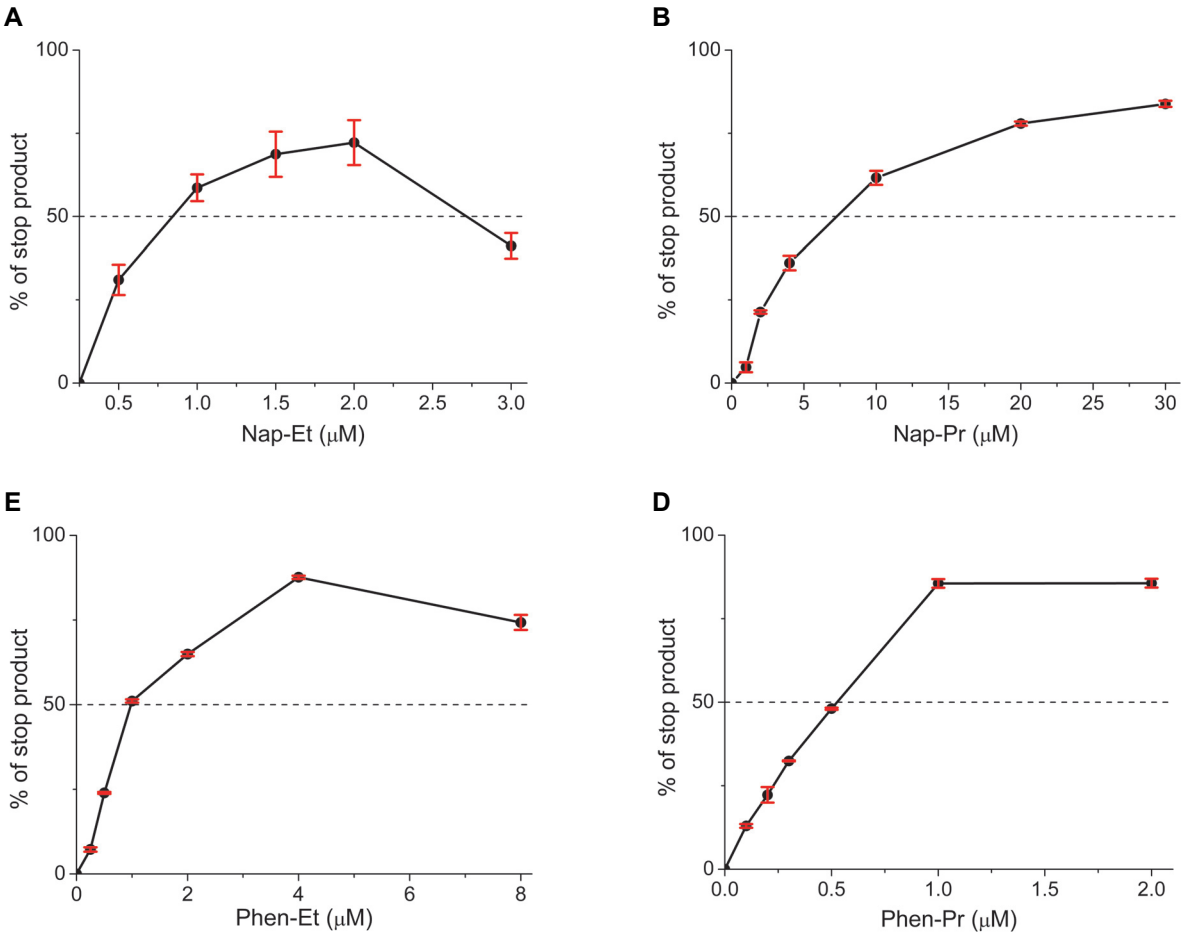

Figure S10. Plots of normalized percentage of stop products versus ligand concentrations. The concentration at which 50% stop product formed was assigned as IC_{50} value. (A) **Nap-Et**. (B) **Nap-Pr**. (C) **Phen-Et**. (D) **Phen-Pr**.

Energy optimized structure of ligands at B3LYP/6-311G level**

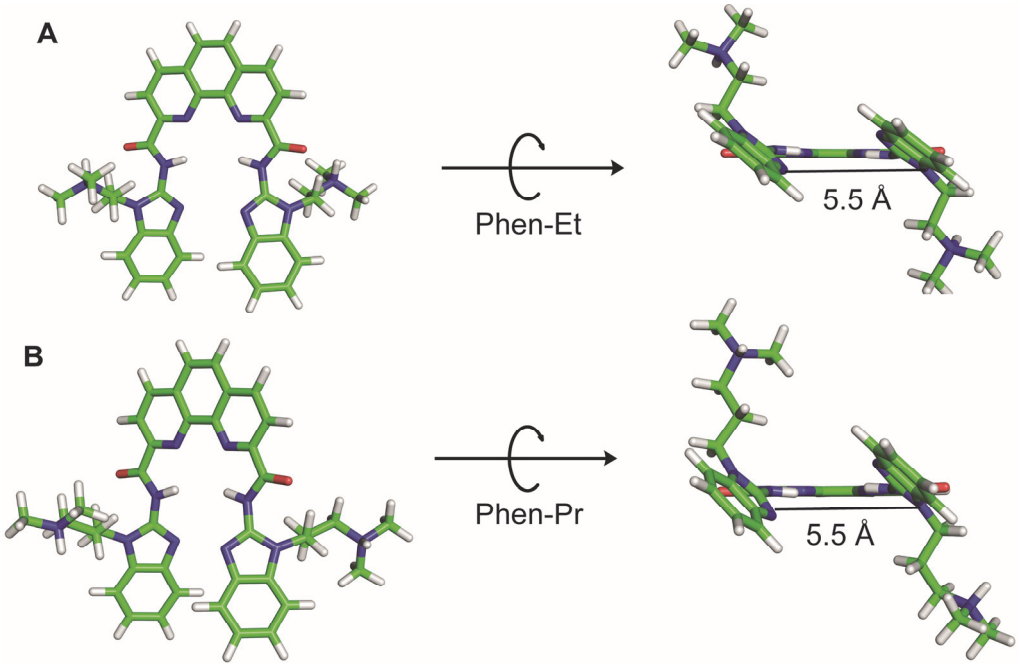

Figure S11. Energy optimized structure of ligands using B3LYP/6-311G** theory level in Gaussian 09. (A) **Phen-Et**. (B) **Phen-Pr** in axial (left) and side (right) view. RESP charges for ligands were derived at HF/6-31G* level. Distance between two benzimidazole rings (side chains) is shown in black lines.

Final MD snapshot of telomeric antiparallel DNA and ligands

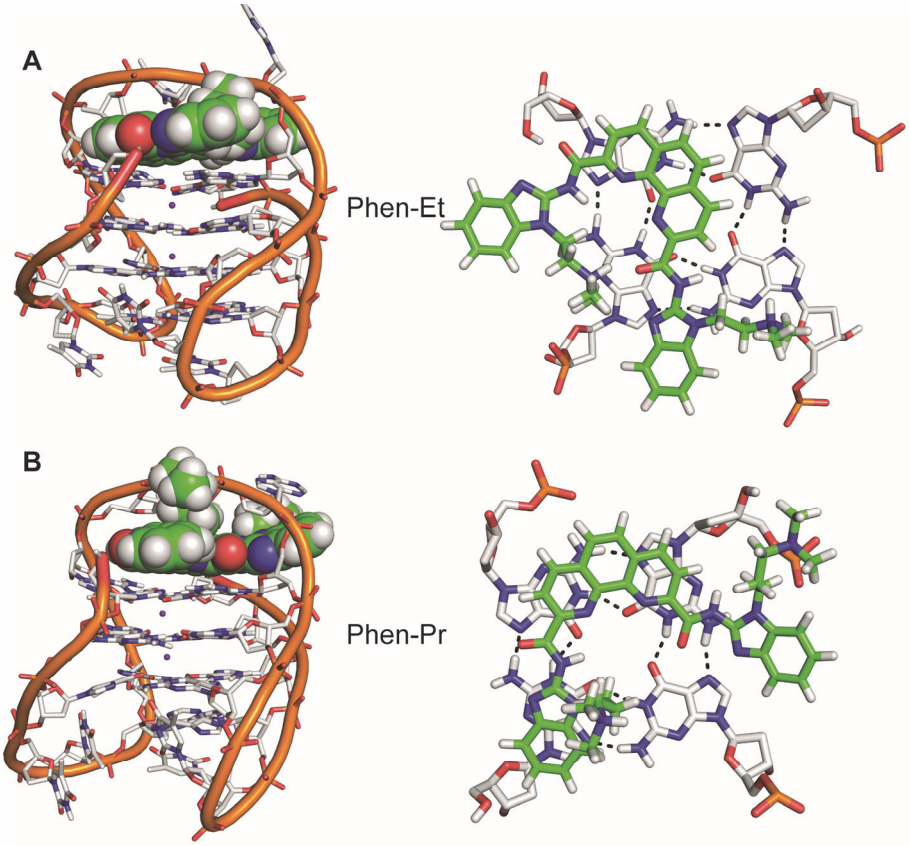

Figure S12. Final MD simulation snapshot of **Phen-Et** and **Phen-Pr** with telomeric antiparallel G-quadruplex DNA after 100 ns. (A) **Phen-Et** bound to antiparallel G-quadruplex DNA. (B) **Phen-Pr** bound to antiparallel G-quadruplex DNA. Nucleosides and phosphate-backbone are represented as stick and cartoon model respectively. Ligands are shown as spheres (green color). Figures were rendered using PyMOL.

Final MD snapshot of ligands with telomeric hybrid DNA

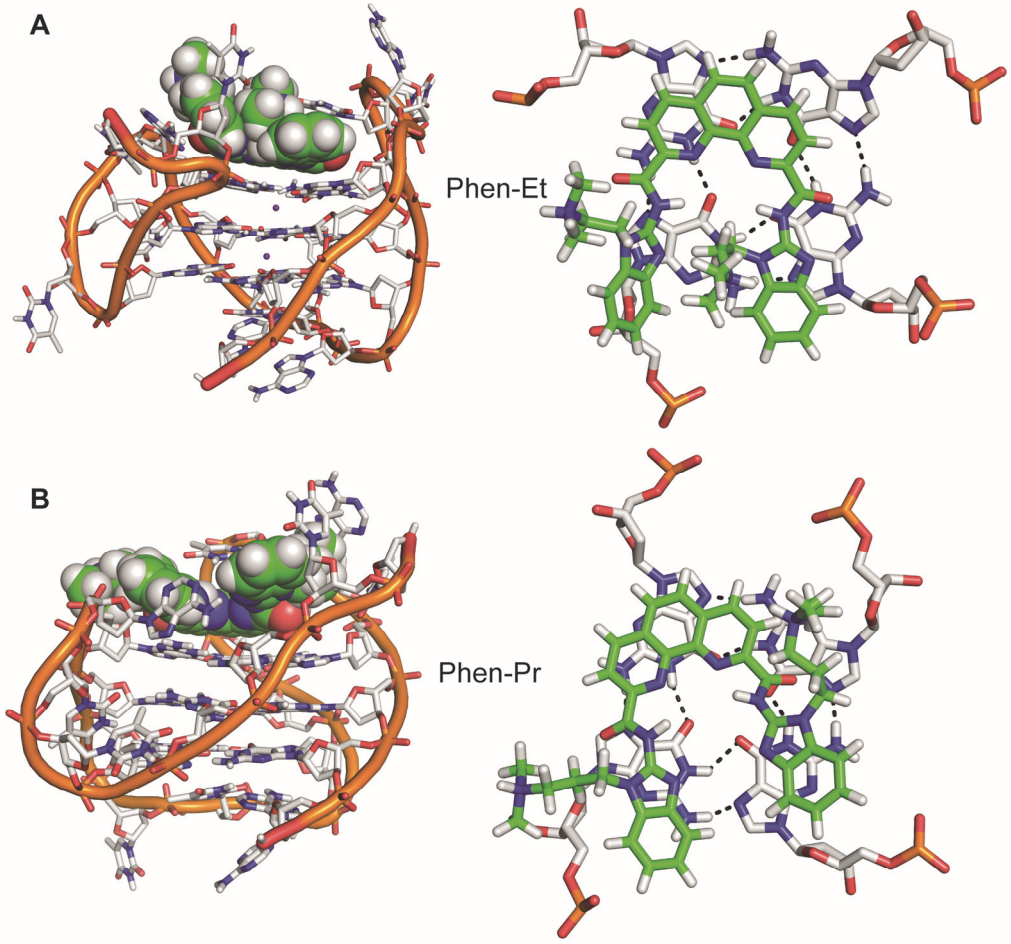

Figure S13. Final MD simulation snapshot of **Phen-Et** and **Phen-Pr** with telomeric hybrid G-quadruplex DNA after 100 ns. (A) **Phen-Et** bound to hybrid G-quadruplex DNA. (B) **Phen-Pr** bound to hybrid G-quadruplex DNA. Nucleosides and phosphate-backbone are represented as stick and cartoon model respectively. Ligands are shown as spheres (green color). Figures were rendered using PyMOL.

Comparison of Phen-Et conformations in complex with G-qudruplex DNAs

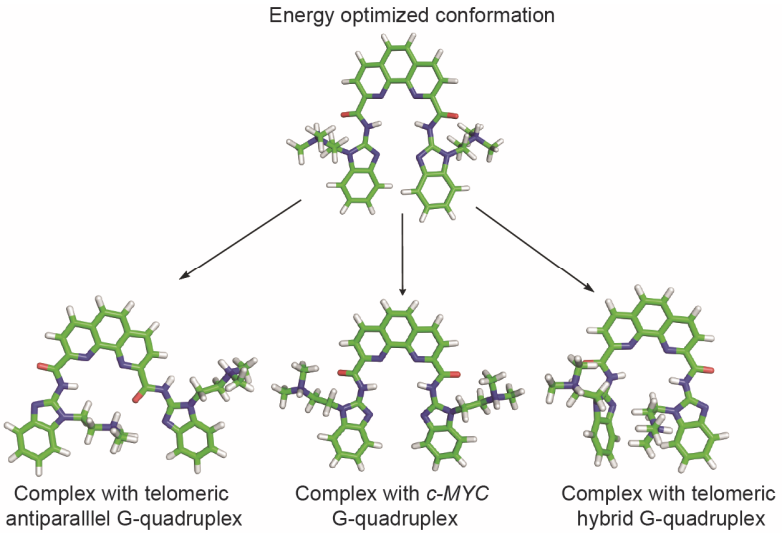

Figure S14. Comparison between energy optimized conformation of **Phen-Et** and in complex with various G-quadruplex DNA topologies. The energy optimized conformation of ligand is at B3LYP/6-311G** level in Gaussian 09. Ligand conformation in complex with *c-MYC*, telomeric antiparallel and hybrid G-quadruplex topologies were obtained after 100 ns of MD simulations. Figures were rendered using PyMOL.

Representation of electrostatic interactions of ligands with telomeric DNAs

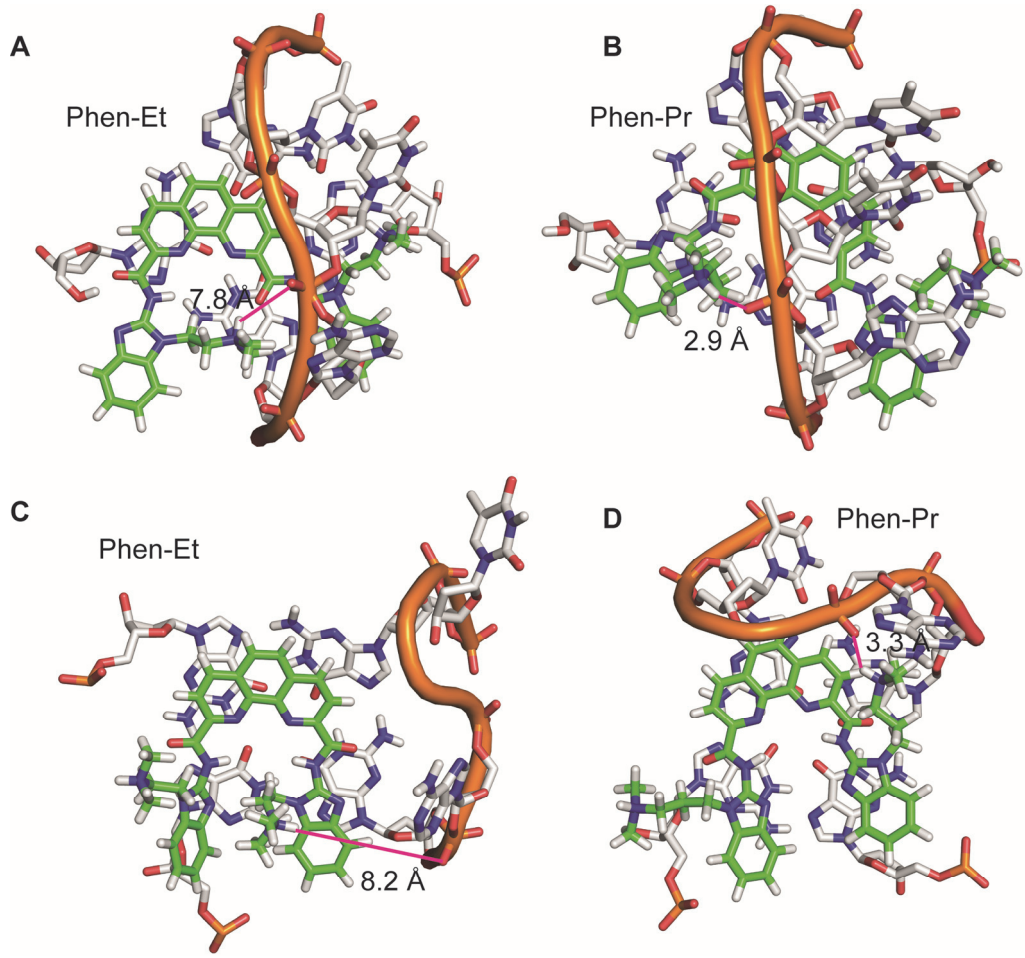

Figure S15. Representation of electrostatic interactions between *N*-protonated side chain and phosphate backbone of telomeric antiparallel and hybrid G-quadruplex DNA during 100 ns of MD simulations. (A) **Phen-Et** with telomeric antiparallel G-quadruplex DNA. (B) **Phen-Pr** with telomeric antiparallel G-quadruplex DNA. (C) **Phen-Et** with telomeric hybrid G-quadruplex DNA. (D) **Phen-Pr** with telomeric hybrid G-quadruplex DNA. The pink line indicates the distance between N-protonated side chain of the ligands and phosphate backbone of the diagonal or lateral loop.

Time dependent RMSD graphs of *c-MYC* DNA and ligands

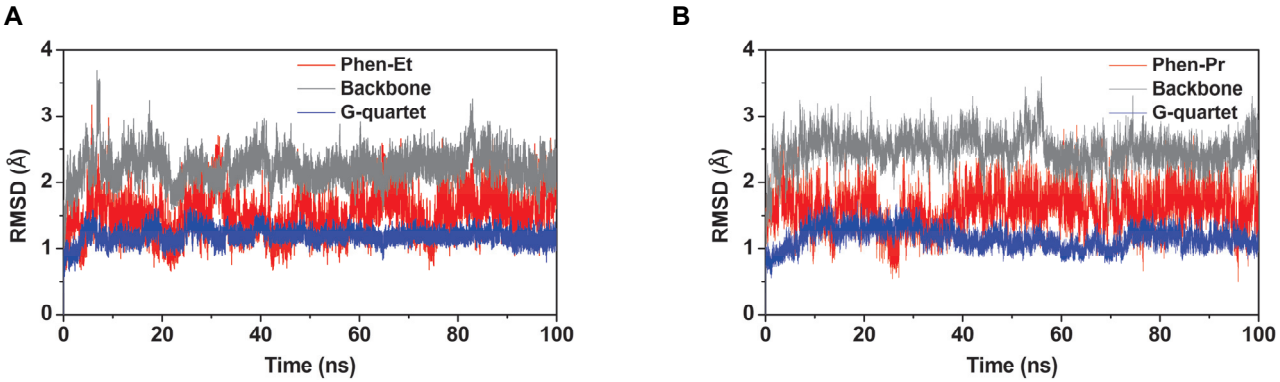

Figure S16. Time dependent root mean square deviation graphs of *c-MYC* G-quadruplex DNA complexed with ligands (Calculated during 100 ns of MD simulation trajectory using ptraj module in AMBER 12). (A) **Phen-Et** with *c-MYC* G-quadruplex DNA. (B) **Phen-Pr** with *c-MYC* G-quadruplex DNA.

Time dependent RMSD graphs of telomeric antiparallel DNA and ligands

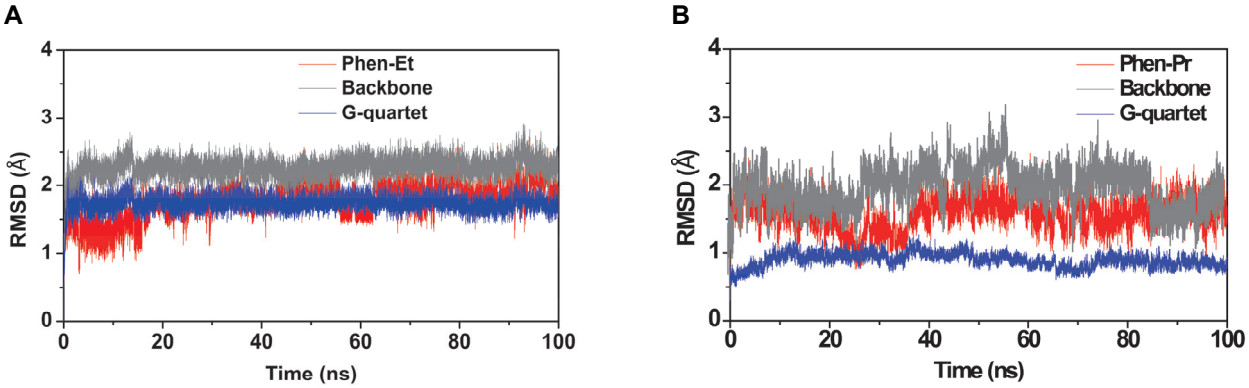

Figure S17. Time dependent root mean square deviation (RMSD) graphs of telomeric antiparallel G-quadruplex DNA complexed with ligands (Calculated during 100 ns of MD simulation trajectory using ptraj module in AMBER 12). (A) **Phen-Et** with telomeric antiparallel G-quadruplex DNA. (B) **Phen-Pr** with telomeric antiparallel G-quadruplex DNA.

Time dependent RMSD graphs of telomeric hybrid DNA and ligands

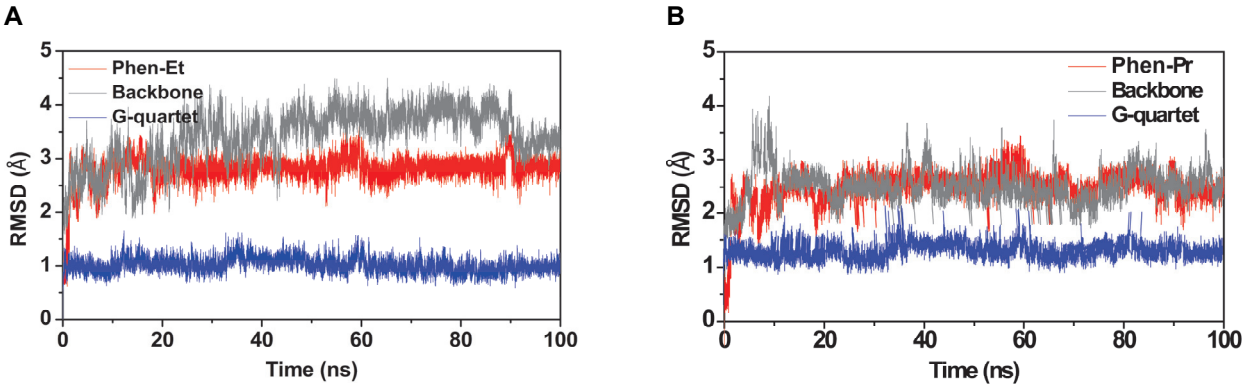

Figure S18. Time dependent root mean square deviation graphs of telomeric hybrid G-quadruplex DNA complexed with ligands (Calculated during 100 ns of MD simulation trajectory using ptraj module in AMBER 12). (A) **Phen-Et** with telomeric hybrid G-quadruplex DNA. (B) **Phen-Pr** telomeric hybrid G-quadruplex DNA**.**

Two dimensional RMSD map of *c-MYC* G-quadruplex DNA and ligands

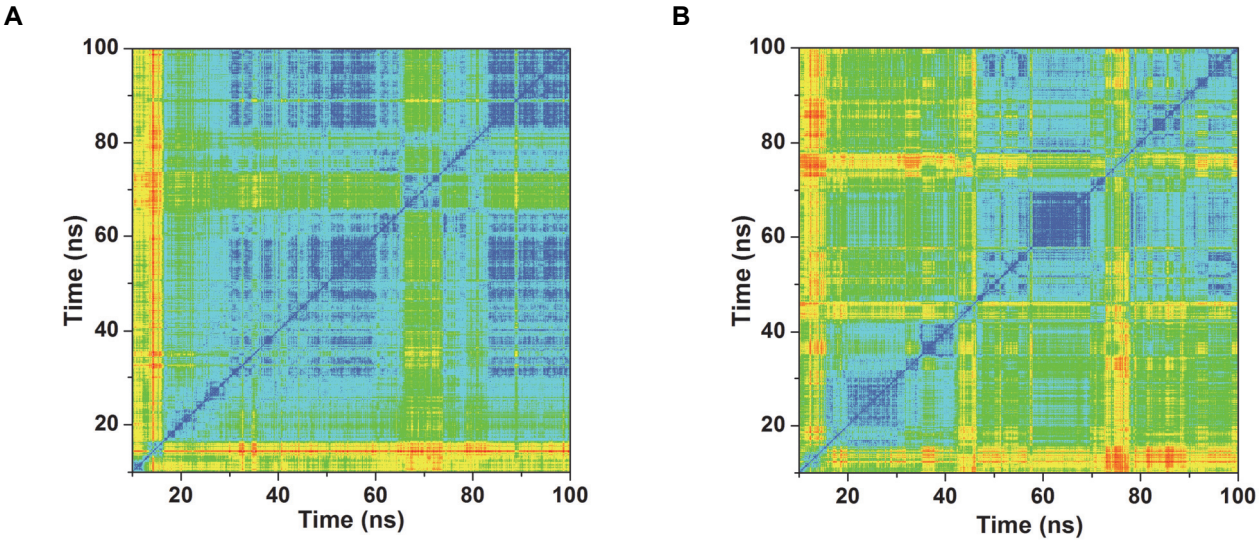

Figure S19. Conformational flexibility of *c-MYC* G-quadruplex DNA and ligand complexes represented by two dimensional root mean square deviation (RMSD) maps during 100 ns of MD simulation. (A) **Phen-Et** with *c-MYC* G-quadruplex DNA. (B) **Phen-Pr** with *c-MYC* G-quadruplex DNA. The colour code is as follow: RMSD from 0 – 0.5Å (blue), 0.5 – 1.5Å (cyan), 1.5 – 2.5 Å (green), 2.5 – 3.5 Å (yellow) and 3.5 – 4.5 Å (red).

Two dimensional RMSD map of telomeric antiparallel DNA and ligands

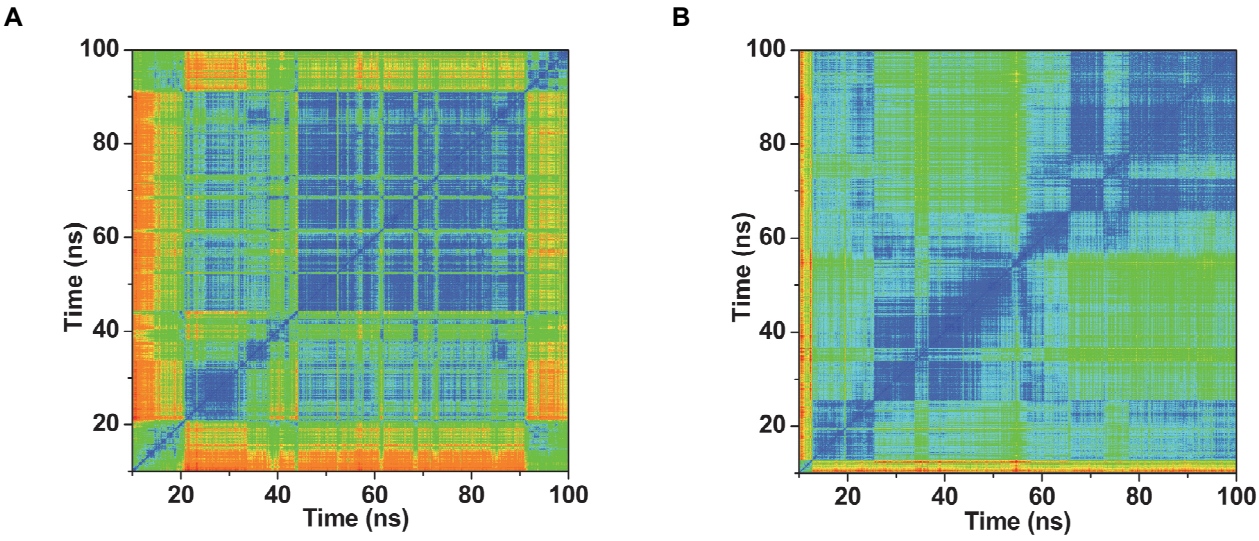

Figure S20. Conformational flexibility of telomeric antiparallel G-quadruplex DNAs and ligand complexes represented by two dimensional root mean square deviations (RMSD) maps during 100 ns of MD simulation. (A) **Phen-Et** with telomeric antiparallel G-quadruplex DNA. (B) **Phen-Pr** with telomeric antiparallel G-quadruplex DNA. The colour code is as follow: RMSD from 0 – 0.5 (blue), 0.5 – 1.5Å (cyan), 1.5 – 2.5 Å (green), 2.5 – 3.5 Å (yellow) and 3.5 – 4.5 Å (red).

Two dimensional RMSD map of telomeric hybrid DNA and ligands

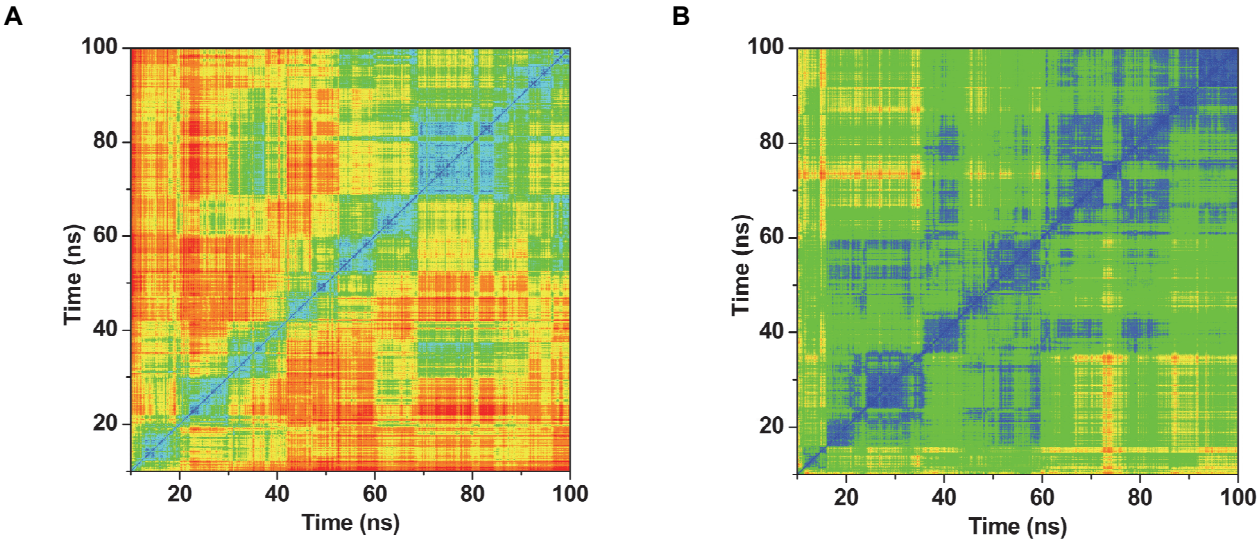

Figure S21. Conformational flexibility of telomeric hybrid G-quadruplex DNAs and ligand complexes represented by two dimensional root mean square deviations (RMSD) maps during 100 ns of MD simulation. (A) **Phen-Et** with telomeric hybrid G-quadruplex DNA. (B) **Phen-Pr** with telomeric hybrid G-quadruplex DNA. The colour code is as follow: 0 – 0.5 Å (blue), 0.5 – 1.5Å (cyan), 1.5 – 2.5 Å (green), 2.5 – 3.5 Å (yellow) and 3.5 – 4.5 Å (red).

Normalized frequency of solvent accessible surface area during MD simulation

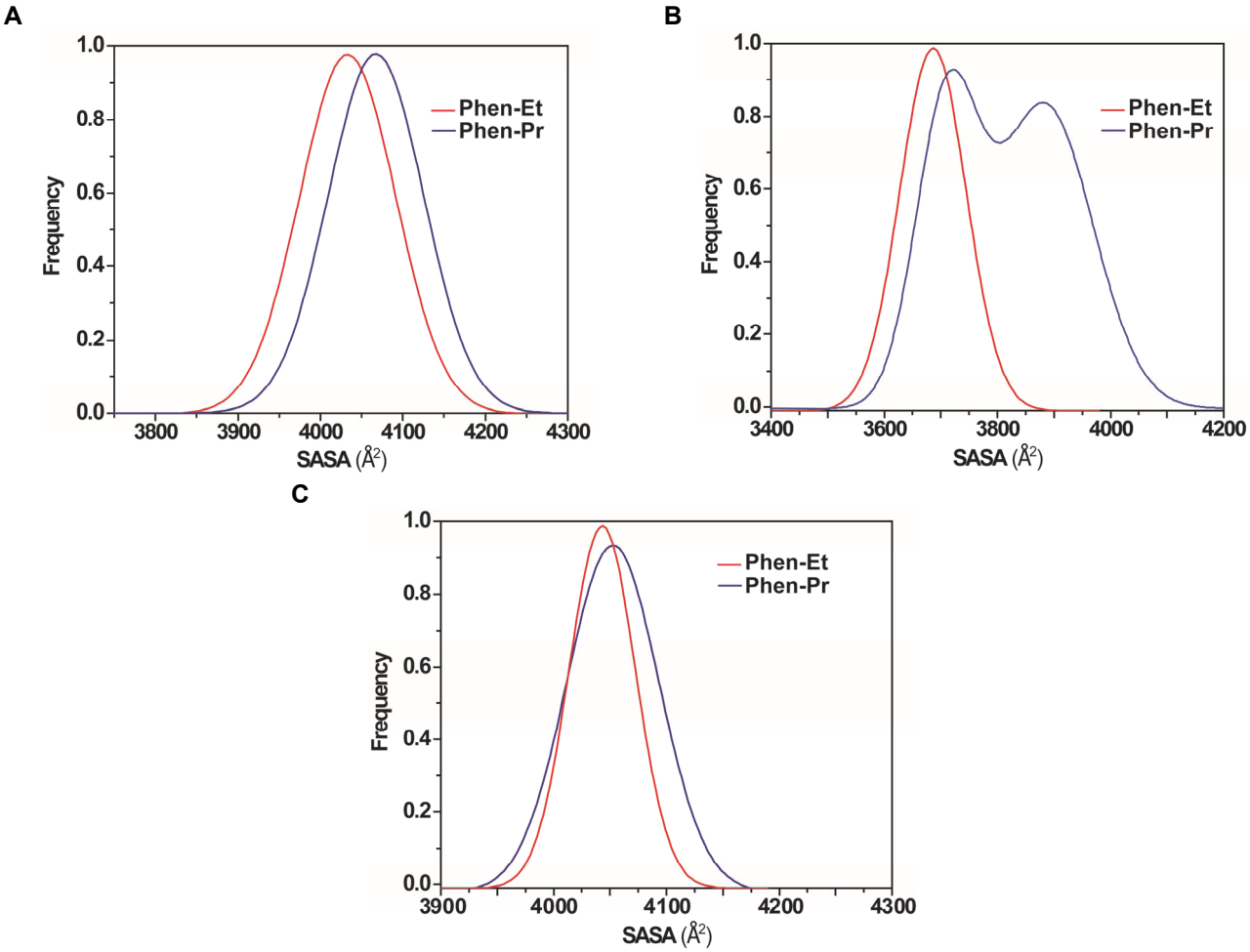

Figure S22. Normalized frequency of solvent accessible surface area (SASA) of G-quadruplex DNA during 100 ns of MD simulations (calculated by Surf module in AMBER 12). (A) *c-MYC* G-quadruplex with ligands. (B) Telomeric antiparallel G-quadruplex with ligands. (C) Telomeric hybrid G-quadruplex DNA with ligands. The SASA of the ligand free *c-MYC* G-quadruplex DNA is 3795 $Å^2$, telomeric antiparallel G-quadruplex DNA is 3527 $Å^2$ and telomeric hybrid G-quadruplex DNA is 3911 $Å^2$.

Final MD snapshot of Phen-Et with telomeric parallel DNA

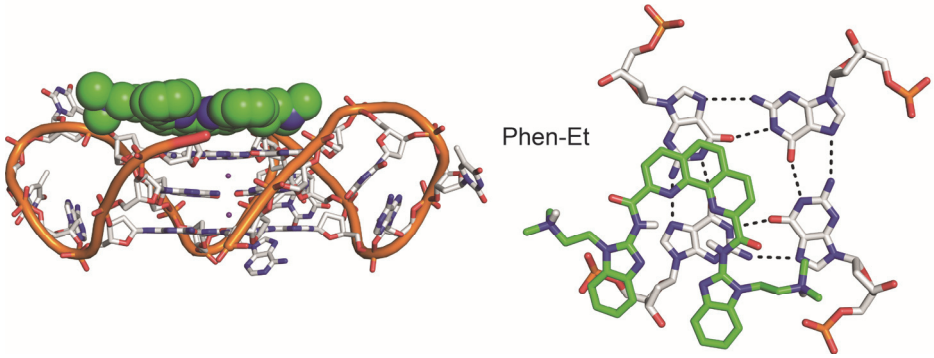

Figure S23. Final MD simulation snapshot (after 100 ns) of **Phen-Et** with telomeric parallel G-quadruplex DNA (PDB ID: 1KF1). Nucleosides and phosphate-backbone are represented as stick and cartoon model respectively. Ligands are shown as spheres (green color).

Time dependent RMSD graph of telomeric parallel DNA and Phen-Et

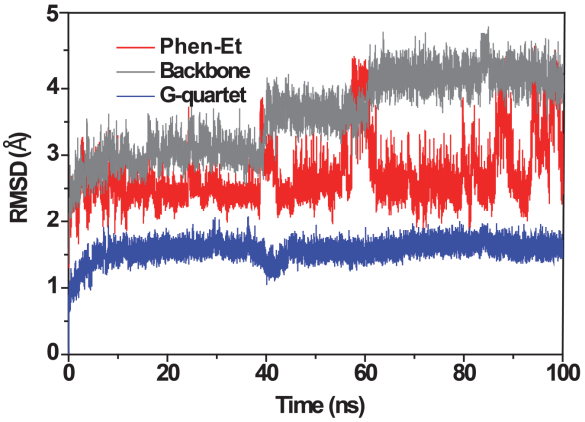

Figure S24. Time dependent root mean square deviation graph of telomeric parallel G-quadruplex DNA complexed with **Phen-Et** (Calculated during 100 ns of MD simulation trajectory using ptraj module in AMBER 12).

Two dimensional RMSD map of telomeric parallel DNA and Phen-Et

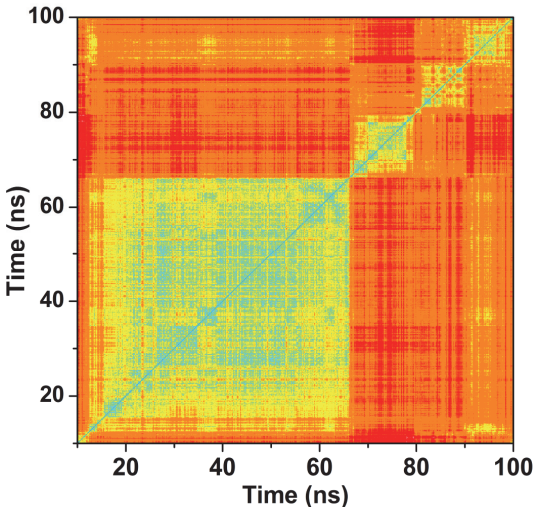

Figure S25. Conformational flexibility of telomeric parallel G-quadruplex DNA and **Phen-Et** complex represented by two dimensional root mean square deviations (RMSD) maps during 100 ns of MD simulation. The colour code is as follow: 0 – 0.5 Å (blue), 0.5 – 1.5Å (cyan), 1.5 – 2.5 Å (green), 2.5 – 3.5 Å (yellow) and 3.5 – 4.5 Å (red).

Final MD snapshot of duplex DNA and ligands

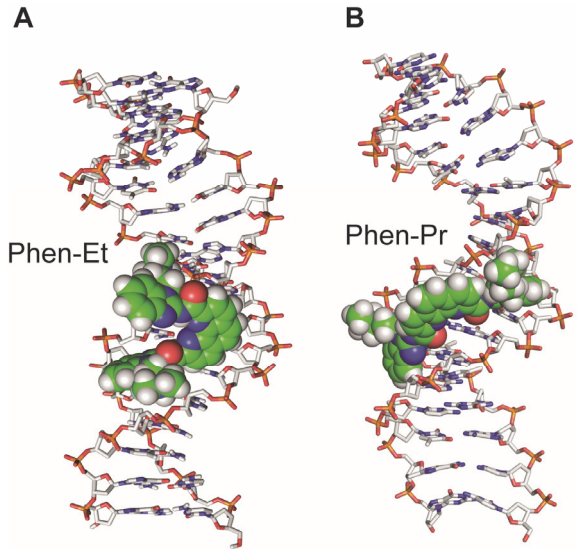

Figure S26. Final MD simulation snapshots of duplex DNA with ligands after 100 ns. (A) **Phen-Et** with duplex DNA. (B) **Phen-Pr** with duplex DNA. DNA and ligands are represented as stick and spheres (green colour) model, respectively. Figures were rendered using PyMOL.

Time dependent RMSD graphs of duplex DNA and ligands

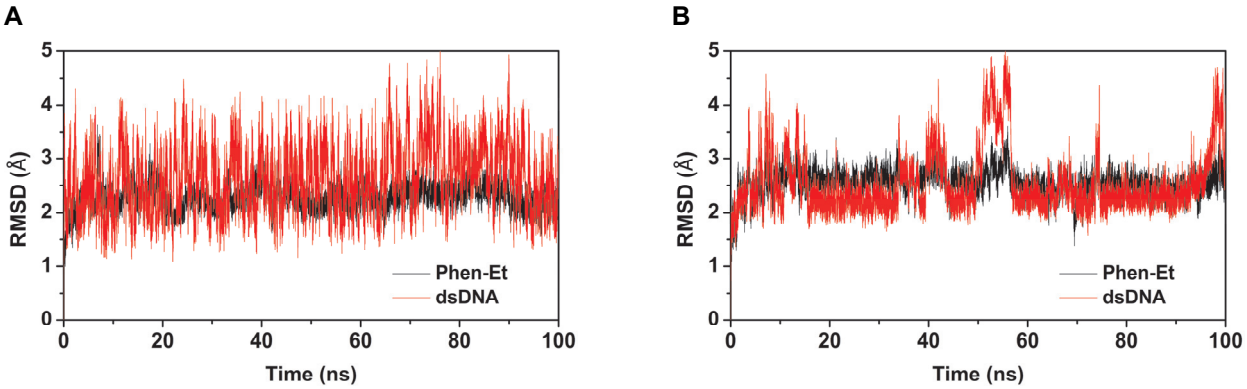

Figure S27. Time dependent root mean square deviation graphs of duplex DNA complexed with ligands (Calculated during 100 ns of MD simulation trajectory using ptraj module in AMBER 12). (A) **Phen-Et** with duplex DNA. (B) **Phen-Pr** with duplex DNA.

Binding free energy components of *c-MYC* G-quadruplex DNA and ligands

MD Simulations (100 ns)	*c-MYC* G-quadruplex DNA (PDB entry: 1XAV)	
	Phen-Et	**Phen-Pr**
ΔE_{ELEC}	−917.66 ± 34.8	−931.02 ± 28.0
ΔE_{VDW}	−75.39 ± 4.4	−81.02 ± 5.3
$\Delta E_{mm}(\Delta E_{Elec}+\Delta E_{VDW})$	−993.05 ± 39.7	−1012.0 ± 25.9
ΔPB_{np}	−6.87 ± 0.4	−7.34 ± 0.4
ΔPB_{cal}	930.40 ± 35.41	946.31 ± 29.70
ΔPB_{solv} ($\Delta PB_{np}+\Delta PB_{cal}$)	923.53 ± 35.0	938.97 ± 29.57
$\Delta H_{PB}(\Delta E_{mm}+\Delta PB_{solv})$	−69.53 ± 6.3	−73.07 ± 7.8
ΔGB_{np}	−6.87 ± 0.4	−7.34 ± 0.5
ΔGB_{cal}	915.81 ± 34.7	935.07 ± 24.3
ΔGB_{solv} ($\Delta GB_{np}+\Delta GB_{cal}$)	908.94 ± 34.2	927.73 ± 27.17
$\Delta H_{GB}(\Delta E_{mm}+\Delta GB_{solv})$	**−84.12 ± 4.6**	**−84.31 ± 7.0**
ΔS_{TRANS}	−13.29 ± 0.01	−13.46 ± 0.0
ΔS_{ROTA}	−11.64 ± 0.02	−11.99 ± 0.0
ΔS_{VIBR}	2.28 ± 1.3	7.81 ± 2.1
$T\Delta S$	−24.45 ± 1.6	−17.65 ± 2.1
ΔG_{bind} ($\Delta G_{GB}-T\Delta S$)	**−61.67± 3.4**	**−66.65 ± 4.2**

Table S1. Binding free energy components of *c-MYC* G-quadruplex DNA with ligands calculated from 100 ns of MD simulations. ΔE_{ELEC} is the electrostatic interaction calculated by the MM force field. ΔE_{VDW} is the Vander Waals contribution from MM. ΔE_{mm} is the total molecular mechanical energy (ΔE_{ELEC} + ΔE_{VDW}). ΔGnp is the nonpolar contribution to the solvation energy. ΔG_{PB} is the electrostatic contribution to the solvation energy calculated by the PB approach. ΔGB_{solv} is the total solvation energy (ΔGnp + ΔG_{PB}). ΔG_{tot} is the total energy without solute entropic contribution (ΔE_{mm} + ΔG_{solv}). $T\Delta S$ is solute entropic contribution. ΔG_{bind} is the total energy with solute entropic contribution ($\Delta G_{tot} - T\Delta S$). The calculations used a subset of snapshots collected during the MD simulations, including the two explicitly bonded K^+ ions. The molecular mechanical energy calculations were calculated using MM/PB-GBSA and entropy calculations were done using nmode in AMBER 12. All the values are reported in kcal/mol. Error values indicate the standard deviation for each component calculated from 100 ns of MD simulations.

Binding free energy components of telomeric antiparallel DNA and ligands

MD Simulations (100 ns)	Telomeric antiparallel G-quadruplex (PDB entry: 143D)	
	Phen-Et	**Phen-Pr**
ΔE_{ELEC}	−844.06 ± 39.7	−901.16 ± 26.4
ΔE_{VDW}	−71.89 ± 3.7	−73.62 ± 5.9
$\Delta E_{mm}(\Delta E_{Elec}+\Delta E_{VDW})$	−915.50 ± 40.9	−984.95 ± 38.5
ΔPB_{np}	−7.40 ± 0.4	−7.65 ± 0.5
ΔPB_{cal}	863.39 ± 40.3	926.52 ± 38.56
ΔPB_{solv} $(\Delta PB_{np}+\Delta PB_{cal})$	855.59 ± 40.1	918.87 ± 38.58
$\Delta G_{PB}(\Delta E_{mm}+\Delta PB_{solv})$	−59.51 ± 5.3	−51.08 ± 5.9
ΔGB_{np}	−7.40 ± 0.4	−7.65 ± 0.3
ΔGB_{cal}	862.51 ± 37.7	925.44 ± 37.7
ΔGB_{solv} $(\Delta GB_{np}+\Delta GB_{cal})$	855.11 ± 37.4	917.79 ± 34.5
$\Delta G_{GB}(\Delta E_{mm}+\Delta GB_{solv})$	−60.39 ± 5.7	−67.16 ± 5.2
ΔS_{TRANS}	−13.42 ± 0.01	−13.37 ± 0.00
ΔS_{ROTA}	−11.84 ± 0.04	−11.82 ± 0.07
ΔS_{VIBR}	0.44 ± 0.32	0.51 ± 0.28
$T\Delta S$	−24.82 ± 2.1	−24.78 ± 1.9
ΔG_{bind} $(\Delta G_{GB}-T\Delta S)$	**−35.57 ± 6.7**	**−42.38 ± 6.7**

Table S2. Binding free energy components of dsDNA G-quadruplex DNA with ligands calculated from 100 ns of MD simulations. The molecular mechanical energy calculations were calculated using MM/PB-GBSA and entropy calculations were done using nmode in AMBER 12. All the values are reported in kcal mol^{-1}. Error values indicate the standard deviation for each component calculated from 100 ns of MD simulations.

Binding free energy components of telomeric hybrid DNA and ligands

MD Simulations (100 ns)	Telomeric hybrid G-quadruplex (PDB entry: 2MB3)	
	Phen-Et	**Phen-Pr**
ΔE_{ELEC}	−752.99 ± 25.64	−855.34 ± 25.84
ΔE_{VDW}	−61.21 ± 21.82	−70.03 ± 3.07
$\Delta E_{mm}(\Delta E_{Elec}+\Delta E_{VDW})$	−813.73 ± 37.38	−925.14 ± 5.14
ΔPB_{np}	−6.25 ± 0.52	−7.71 ± 0.7
ΔPB_{cal}	798.58 ± 28.6	891.17 ± 20.5
ΔPB_{solv} ($\Delta PB_{np}+\Delta PB_{cal}$)	792.33 ± 20.3	883.46 ± 26.7
$\Delta G_{PB}(\Delta E_{mm}+\Delta PB_{solv})$	−21.40 ± 3.9	−41.64 ± 4.5
ΔGB_{np}	−6.25 ± 0.52	−7.71 ± 0.7
ΔGB_{cal}	779.60 ± 26.91	871.20 ± 27.5
ΔGB_{solv} ($\Delta GB_{np}+\Delta GB_{cal}$)	773.34 ± 24.80	863.49 ± 24.8
$\Delta G_{GB}(\Delta E_{mm}+\Delta GB_{solv})$	**−40.38 ± 3.7**	**−61.61 ± 3.9**
ΔS_{TRANS}	−13.79 ± 0.03	−13.52 ± 0.01
ΔS_{ROTA}	−12.14 ± 0.01	−12.16 ± 0.04
ΔS_{VIBR}	−2.58 ± 0.52	6.35 ± 0.32
$T\Delta S$	−28.25 ± 2.27	−19.33 ± 1.5
ΔG_{bind} ($\Delta G_{GB}-T\Delta S$)	**−12.13 ± 3.7**	**−42.28 ± 5.2**

Table S3. Binding free energy components of telomeric hybrid G-quadruplex DNA with ligands calculated from 100 ns of MD simulations. The molecular mechanical energy calculations were calculated using MM/PB-GBSA and entropy calculations were done using nmode in AMBER 12. All the values are reported in kcal mol^{-1}. Error values indicate the standard deviation for each component calculated from 100 ns of MD simulations.

Occurrence of non-covalent interactions between G-quadruplex DNA and ligands

c-MYC	Electrostatic interaction	Stacking interaction
Phen-Et	83%	82%
Phen-Pr	89%	85%
Telomeric antiparallel	**Electrostatic interaction**	**Stacking interaction**
Phen-Et	45%	39%
Phen-Pr	68%	59%
Telomeric hybrid	**Electrostatic interaction**	**Stacking interaction**
Phen-Et	8%	6%
Phen-Pr	74%	65%
Telomeric parallel	**Electrostatic interaction**	**Stacking interaction**
Phen-Et	5%	12%

Table S4. Percentage of simulation time during which electrostatic and stacking interaction were present. The stacking interactions were considered when the distance between the ligand and the G-quartet is < 3.5 Å, and the vector of the plane formed by the two rings is ± 10°. The cutoff distance used for the electrostatic interactions between N-protonated side chain and DNA backbone is < 3.5 Å. The interactions were calculated at each ps from the 100 ns of MD simulation trajectory using ptraj module in AMBER 12.

Stacking energy of G-quartet calculated at MP2/6-31G*(0.25) level

G-quadruplex/ligand complexes	Energy values at MP2/6-31G*(0.25) level			
	Top quartet	Bottom quartet	All 3 G-quartets	Δ*E*
c-MYC	−152.84	−150.28	−227.58	-
Phen-Et	−165.27	−159.54	−248.39	−20.81
Phen-Pr	−169.62	−163.51	−250.14	−22.56
Telomeric antiparallel	−117.51	−113.72	−212.54	-
Phen-Et	−121.48	−117.89	−216.27	−3.73
Phen-Pr	−20.81	−20.81	−222.30	−9.76
Telomeric hybrid	−121.53	−117.56	−218.35	-
Phen-Et	−122.38	−119.65	−222.07	−3.72
Phen-Pr	−129.86	−124.61	−229.24	−10.89

Table S5. Stacking energy of lowest energy structure of G-quadruplex DNA in the geometry of complex state with **Phen-Et** and **Phen-Pr** ligands. The Δ*E* is obtained by comparing the stacking energy of initial quadruplex structure (without ligand) and ligand bound structure obtained from 100 ns of MD simulations. All the values are reported in kcal mol^{-1}.

Average RMSDs of G-quadruplex-ligand complexes

c-MYC	G-quartet	Ligand	Backbone	Loop-1	Loop-2	Loop-3
Phen-Et	1.1 ± 0.1	1.5 ± 0.3	2.2 ± 0.2	1.4 ± 0.2	2.3 ± 0.4	1.2 ± 0.4
Phen-Pr	1.1 ± 0.1	1.6 ± 0.2	2.4 ± 0.2	1.2 ± 0.1	2.2 ± 0.4	1.1 ± 0.3
Telomeric antiparallel	**G-quartet**	**Ligand**	**Backbone**	**Loop-1**	**Loop-2**	**Loop-3**
Phen-Et	1.7 ± 0.1	1.9 ± 0.2	2.2 ± 0.1	1.4 ± 0.1	1.7 ± 0.3	1.3 ± 0.6
Phen-Pr	2.1 ± 0.2	1.8 ± 0.4	2.4 ± 0.2	1.4 ± 0.1	1.6 ± 0.1	1.3 ± 0.4
Telomeric hybrid	**G-quartet**	**Ligand**	**Backbone**	**Loop-1**	**Loop-2**	**Loop-3**
Phen-Et	1.3 ± 0.2	3.1 ± 0.4	2.9 ± 0.2	1.5 ± 0.1	2.4 ± 0.8	2.0 ± 0.2
Phen-Pr	1.1 ± 0.1	1.5 ± 0.2	2.2 ± 0.1	1.1 ± 0.1	1.1 ± 0.2	1.8 ± 0.2
Telomeric parallel	**G-quartet**	**Ligand**	**Backbone**	**Loop-1**	**Loop-2**	**Loop-3**
Phen-Et	1.5 ± 0.2	2.9 ± 1.4	3.4 ± 0.8	2.4 ± 0.3	2.5 ± 0.4	2.4 ± 0.4

Table S6. Average RMSDs of G-quadruplex DNA-ligand complexes during 100 ns of MD simulations. For G-quartet, heavy atoms guanine bases involved in the formation of G-quartet were considered. For ligands, only the heavy atoms in the ligands were considered. For backbone, heavy atoms of the G-quadruplex DNA backbone were considered. For loop atoms, the DNA backbone and bases involved in the formation lateral/propeller/diagonal loop were considered. All the values were calculated using ptraj and are reported in Å. Error values indicate the standard deviation for each component calculated from 100 ns of MD simulations.

Binding free energy components of telomeric parallel DNA and Phen-Et

MD Simulations (100 ns)	Telomeric parallel G-quadruplex (PDB entry: 1KF1)
	Phen-Et
ΔE_{ELEC}	−729.67 ± 22.67
ΔE_{VDW}	−53.21 ± 10.75
$\Delta E_{mm}(\Delta E_{Elec}+\Delta E_{VDW})$	−782.88 ± 31.82
ΔPB_{np}	−6.10 ± 0.21
ΔPB_{cal}	768.75 ± 28.9
ΔPB_{solv} ($\Delta PB_{np}+\Delta PB_{cal}$)	761.52 ± 22.5
$\Delta G_{PB}(\Delta E_{mm}+\Delta PB_{solv})$	−21.40 ± 3.90
ΔGB_{np}	−6.10 ± 0.21
ΔGB_{cal}	728.45 ± 26.91
ΔGB_{solv} ($\Delta GB_{np}+\Delta GB_{cal}$)	734.27 ± 24.80
$\Delta G_{GB}(\Delta E_{mm}+\Delta GB_{solv})$	**−48.23 ± 2.8**
ΔS_{TRANS}	−13.69 ± 0.03
ΔS_{ROTA}	−12.21 ± 0.01
ΔS_{VIBR}	−3.7 ± 0.47
$T\Delta S$	−29.6 ± 1.96
ΔG_{bind} ($\Delta G_{GB}-T\Delta S$)	**−18.63 ± 3.2**

Table S7. Binding free energy components of telomeric parallel G-quadruplex DNA with ligand calculated from 100 ns of MD simulations. The molecular mechanical energy calculations were calculated using MM/PB-GBSA and entropy calculations were done using nmode in AMBER 12. All the values are reported in kcal mol^{-1}. Error values indicate the standard deviation for each component calculated from 100 ns of MD simulations.

Binding free energy components of duplex DNA-ligand complexes

MD Simulations (100 ns)	Duplex DNA	
	Phen-Et	**Phen-Pr**
ΔE_{ELEC}	−827.97 ± 28.4	−863.80 ± 26.8
ΔE_{VDW}	−49.20 ± 3.6	−59.21 ± 2.7
$\Delta E_{mm}(\Delta E_{Elec}+\Delta E_{VDW})$	−876.67 ± 27.2	−922.73 ± 24.3
ΔPB_{np}	−6.39 ± 0.6	−5.89 ± 0.6
ΔPB_{cal}	846.27 ± 25.65	888.77 ± 22.61
ΔPB_{solv} ($\Delta PB_{np}+\Delta PB_{cal}$)	839.89 ± 29.8	881.87 ± 27.63
$\Delta G_{PB}(\Delta E_{mm}+\Delta PB_{solv})$	−36.81 ± 6.1	−40.86 ± 6.2
ΔGB_{np}	−6.39 ± 0.6	−6.89 ± 0.7
ΔGB_{cal}	847.52 ± 23.8	881.97 ± 21.8
ΔGB_{solv} ($\Delta GB_{np}+\Delta GB_{cal}$)	841.13 ± 24.5	875.08 ± 22.09
$\Delta G_{GB}(\Delta E_{mm}+\Delta GB_{solv})$	**−35.54 ± 4.6**	**−47.65 ± 7.0**
ΔS_{TRANS}	−13.48 ± 0.01	−13.59 ± 0.01
ΔS_{ROTA}	−12.24 ± 0.02	−12.06 ± 0.05
ΔS_{VIBR}	4.02 ± 2.2	−2.06 ± 1.7
$T\Delta S$	−21.70 ± 2.4	−27.65 ± 2.2
ΔG_{bind} ($\Delta G_{GB}-T\Delta S$)	**−14.47± 5.2**	**−20.00 ± 2.9**

Table S8. Binding free energy components of dsDNA with ligands calculated from 100 ns of MD simulations. The molecular mechanical energy calculations were calculated using MM/PB-GBSA and entropy calculations were done using nmode in AMBER 12. All the values are reported in kcal mol^{-1}. Error values indicate the standard deviation for each component calculated from 100 ns of MD simulations.

^{1}H & ^{13}C NMR spectra

^{1}H NMR of compound **1**

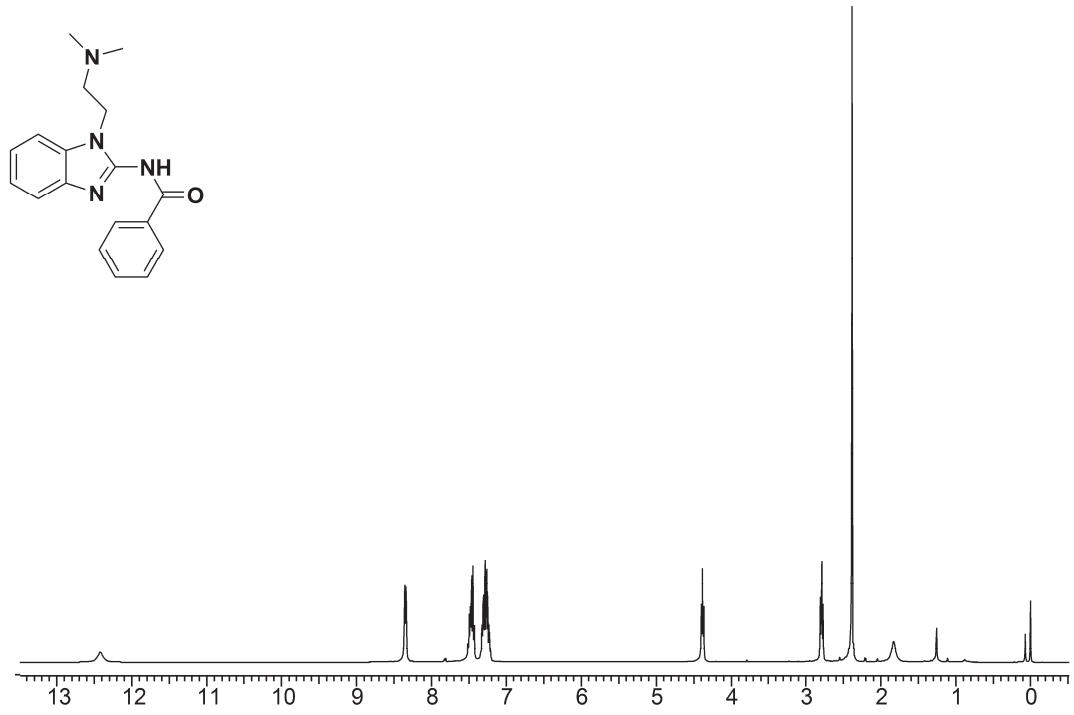

^{13}C NMR of compound **1**

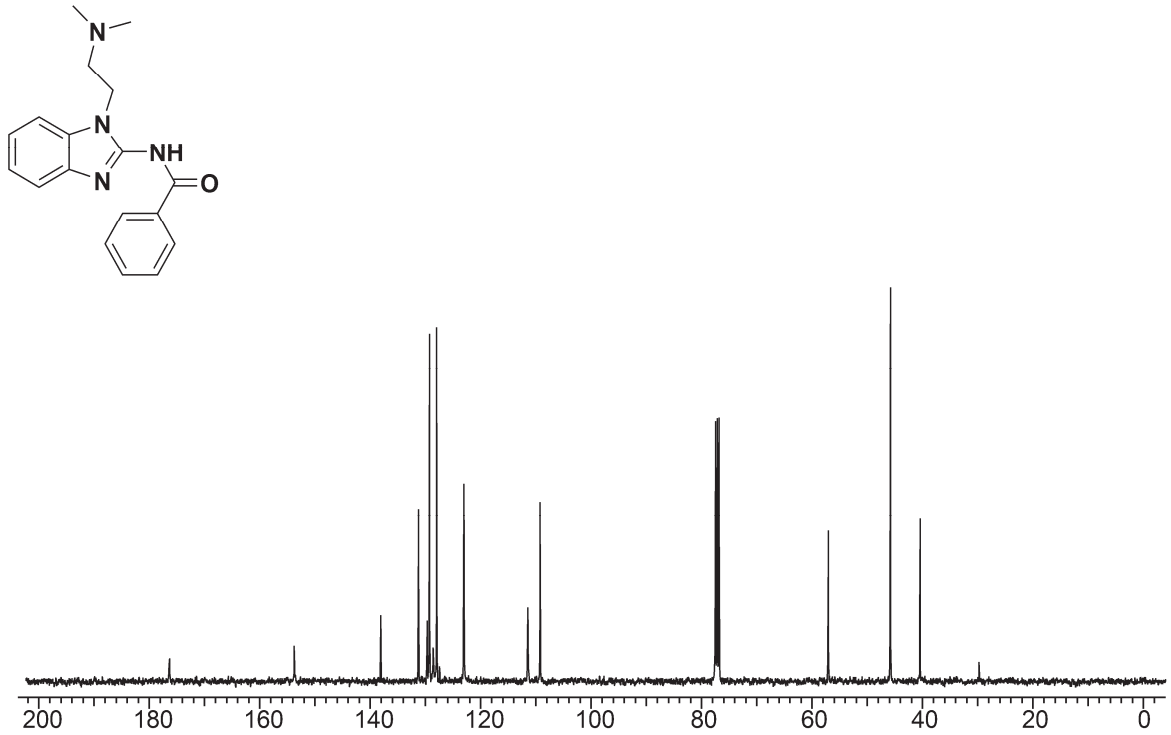

^{1}H NMR of compound **2**

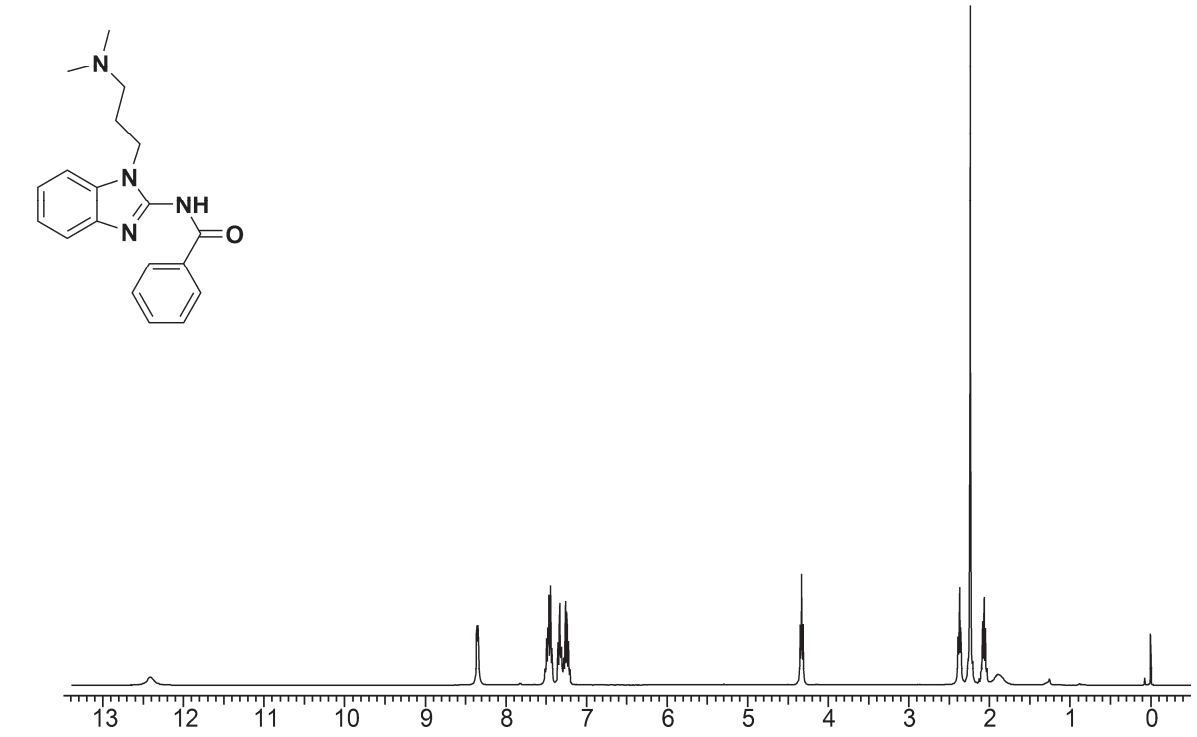

^{13}C NMR of compound **2**

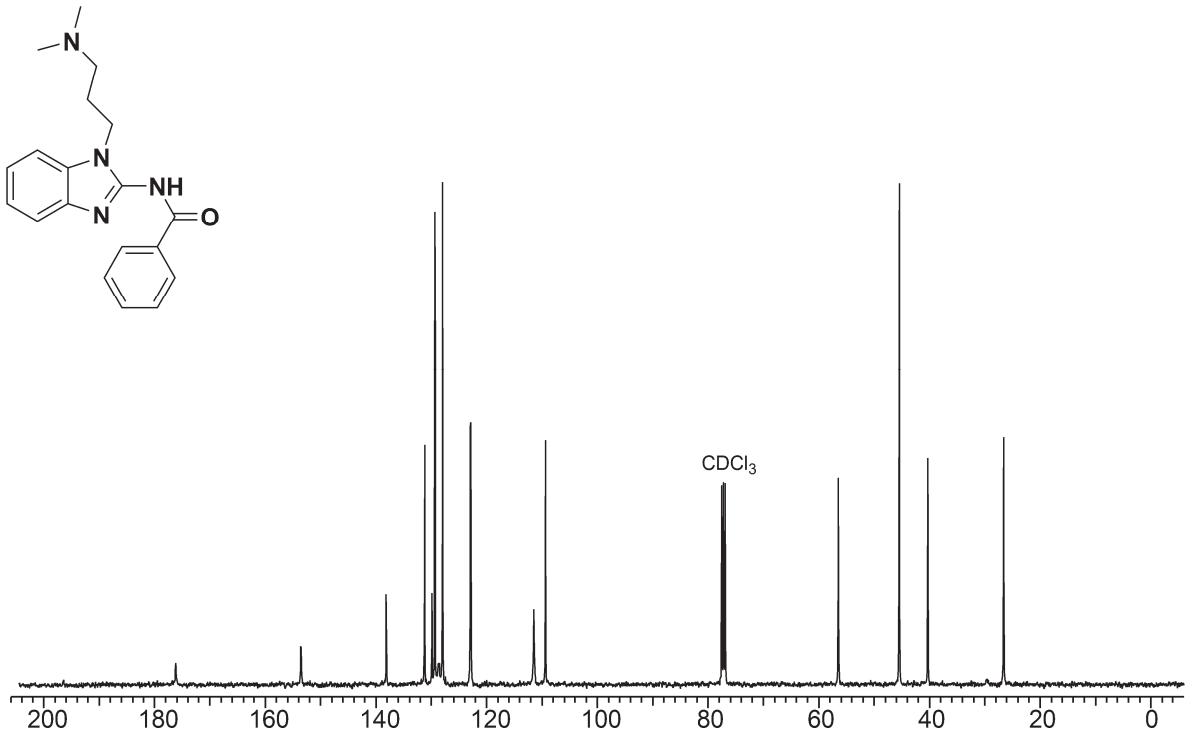

^{1}H NMR of compound **3**

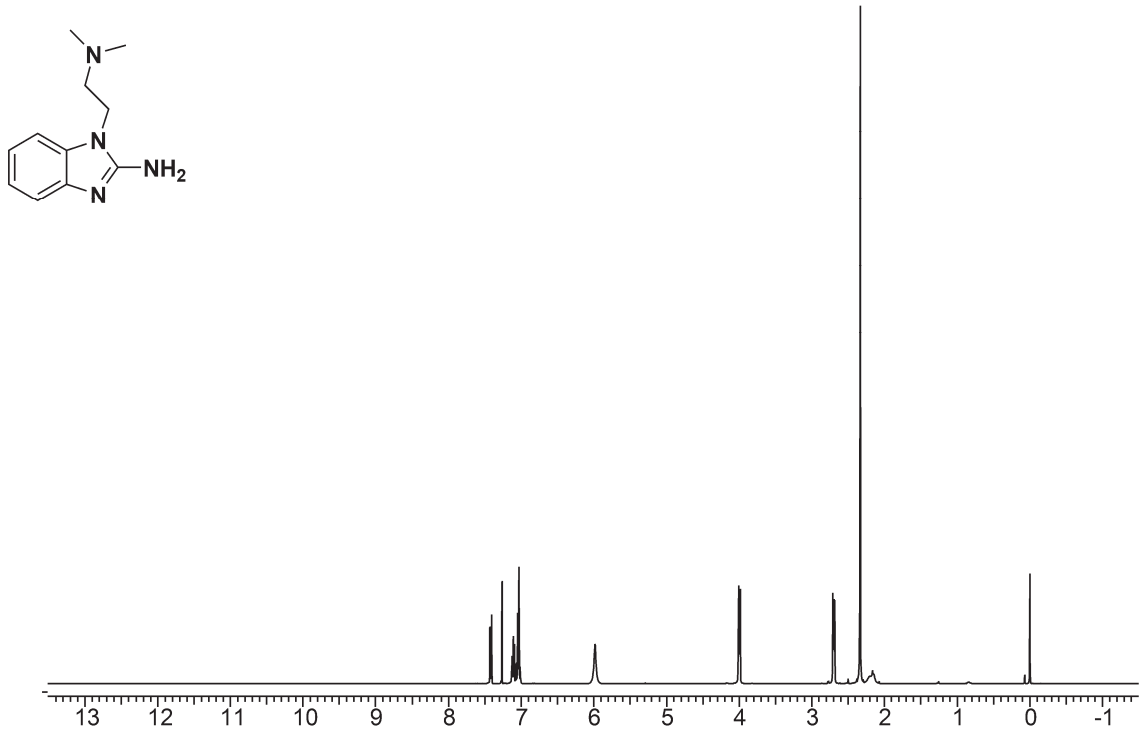

^{13}C NMR of compound **3**

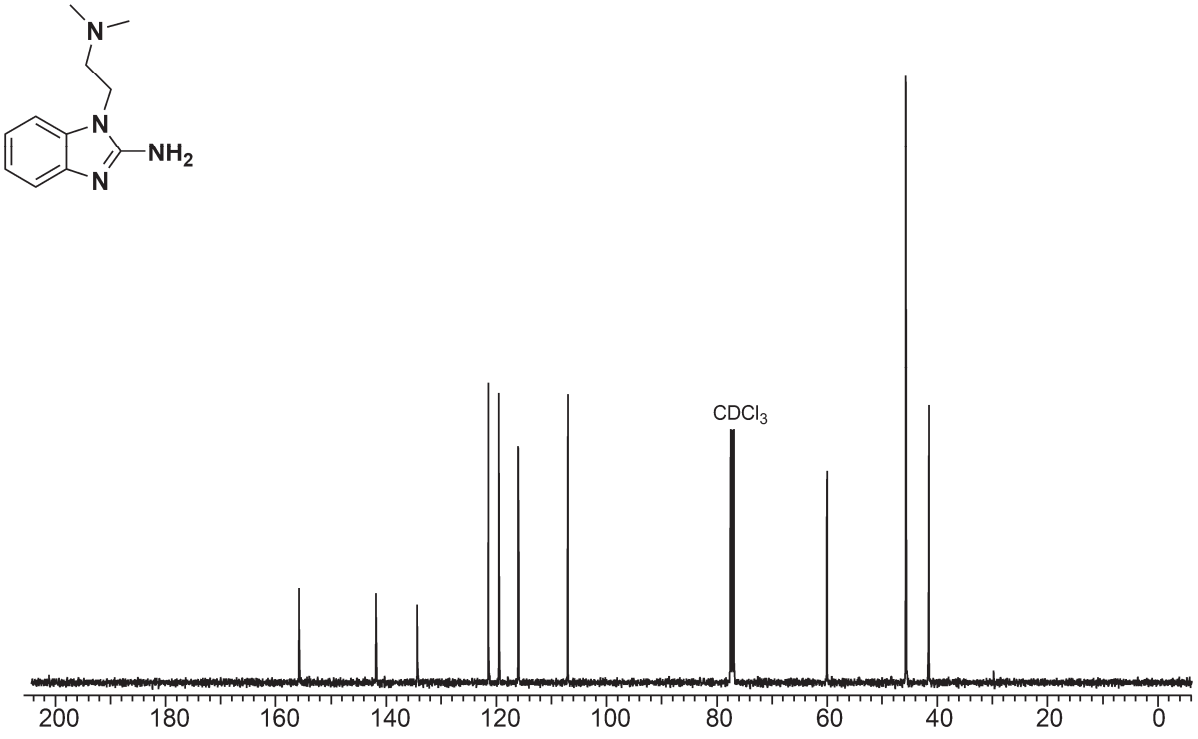

^{1}H NMR of compound **4**

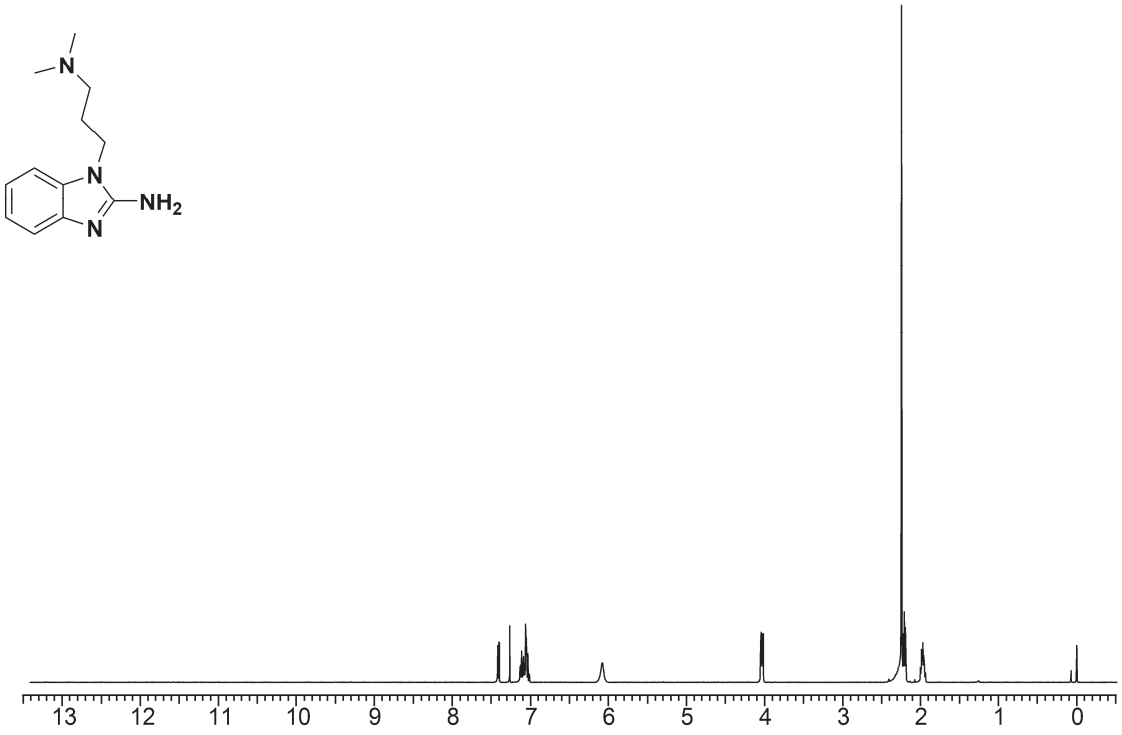

^{13}C NMR of compound **4**

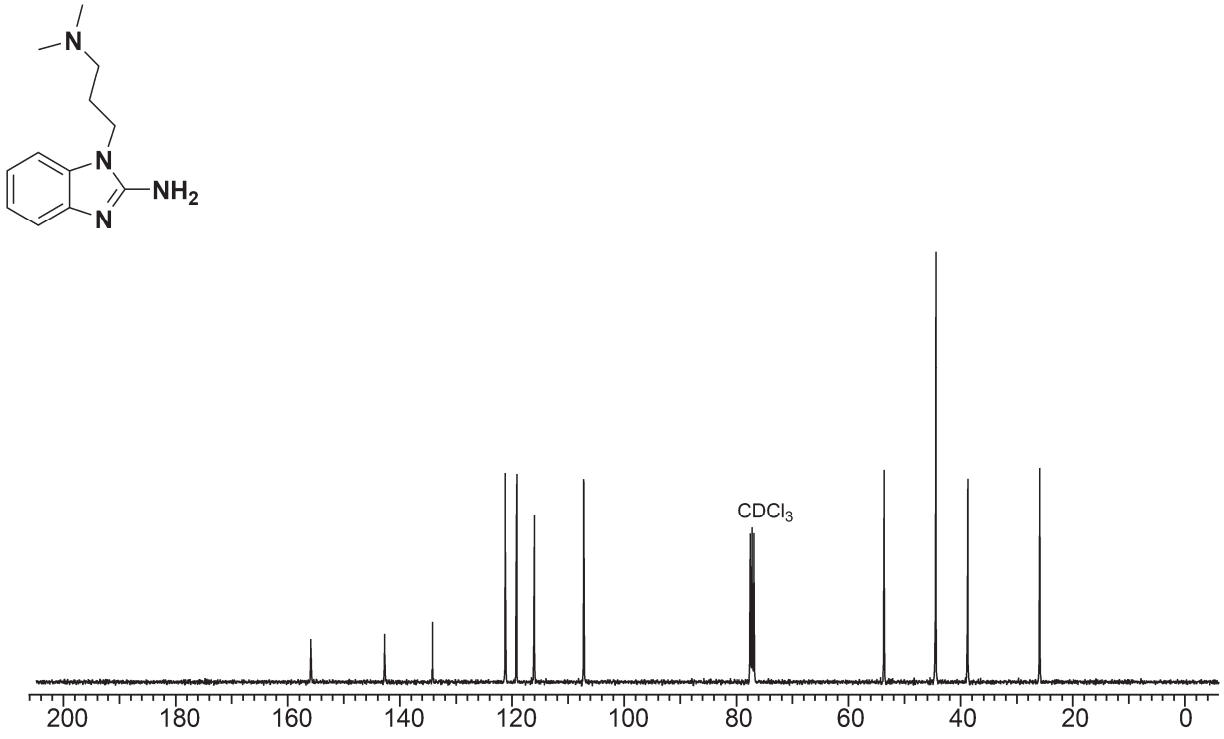

^{1}H NMR of compound **Py-Et**

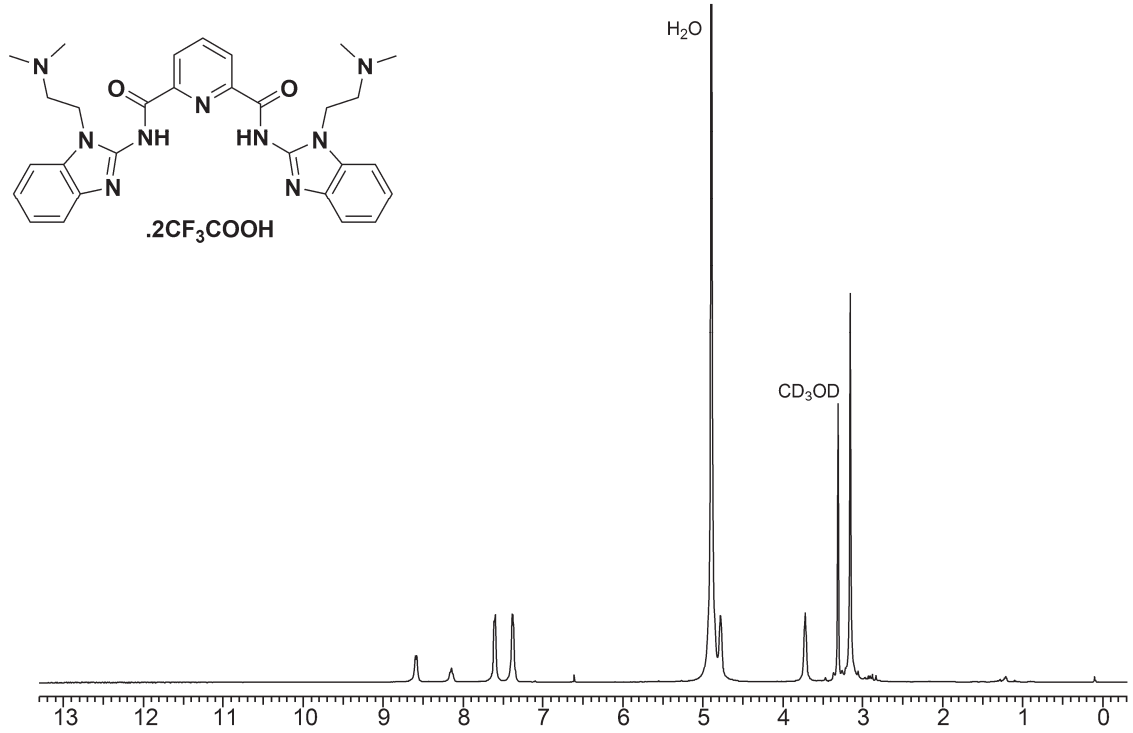

^{13}C NMR of compound **Py-Et**

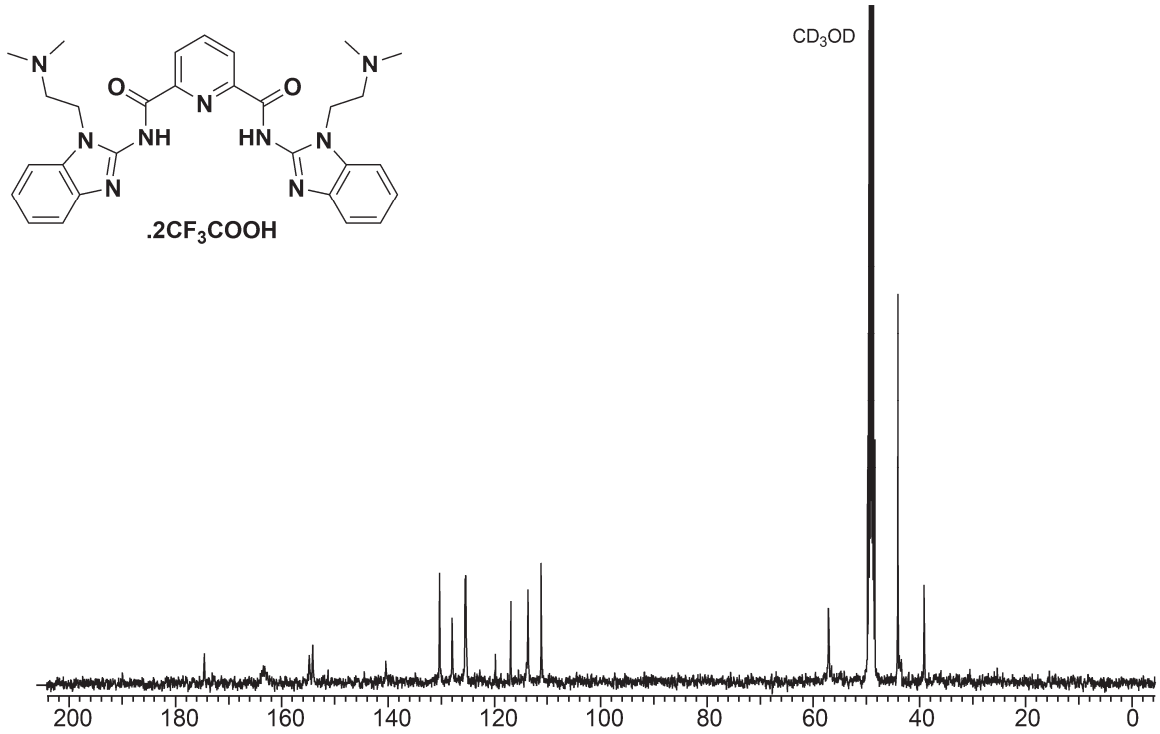

^{1}H NMR of compound **Py-Pr**

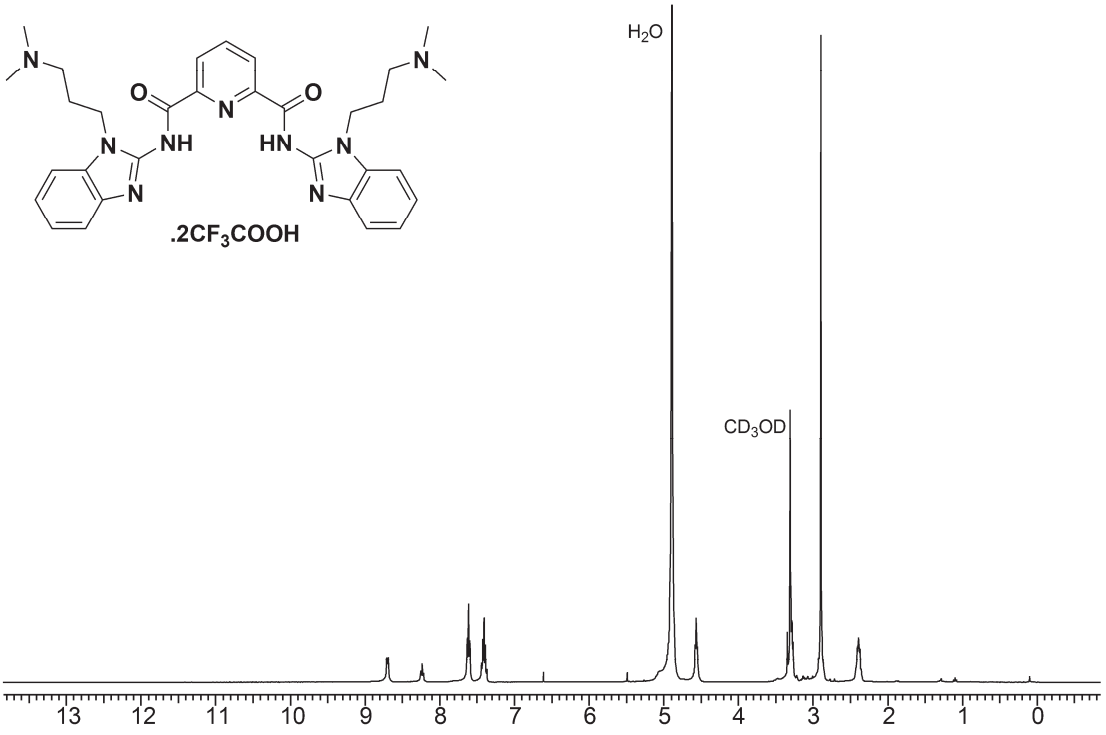

^{13}C NMR of compound **Py-Pr**

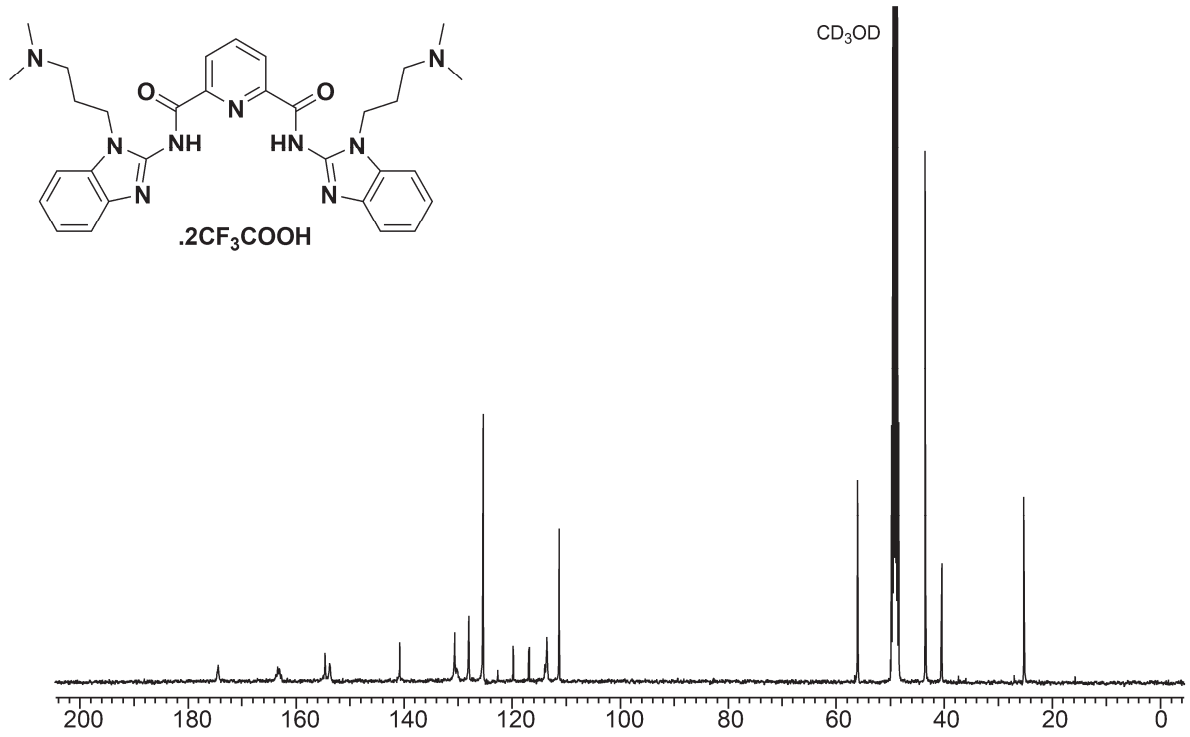

^{1}H NMR of compound **Nap-Et**

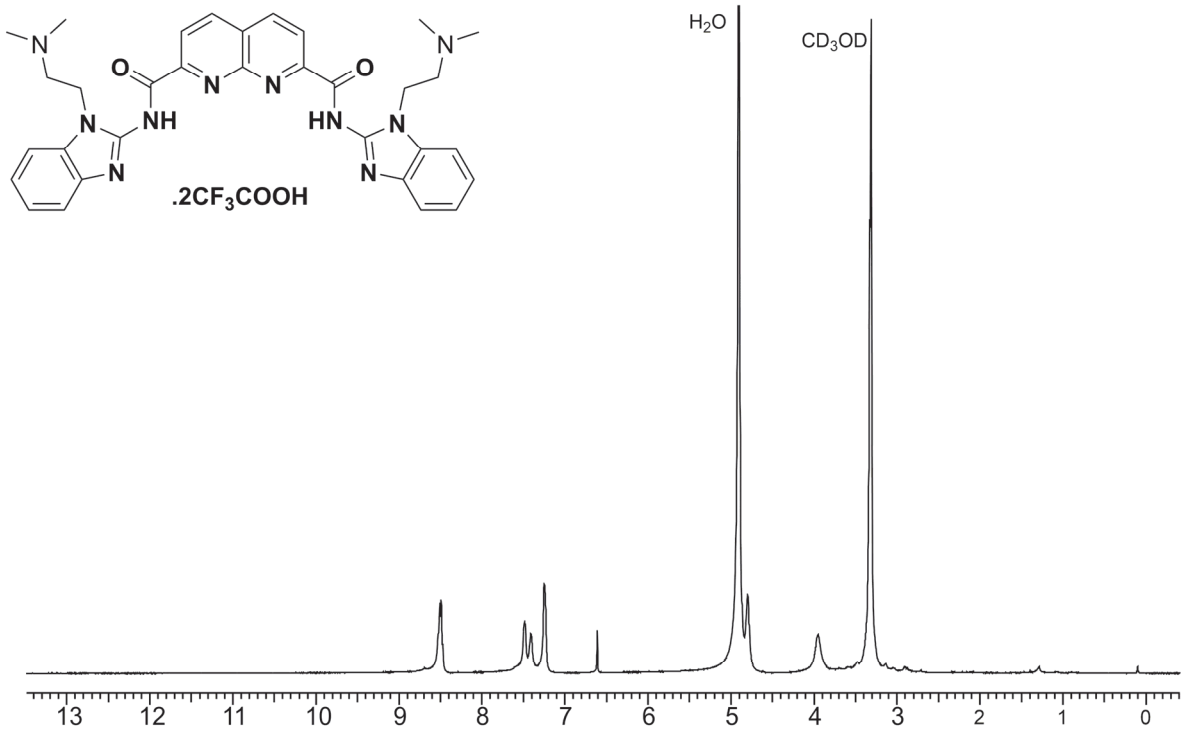

^{13}C NMR of compound **Nap-Et**

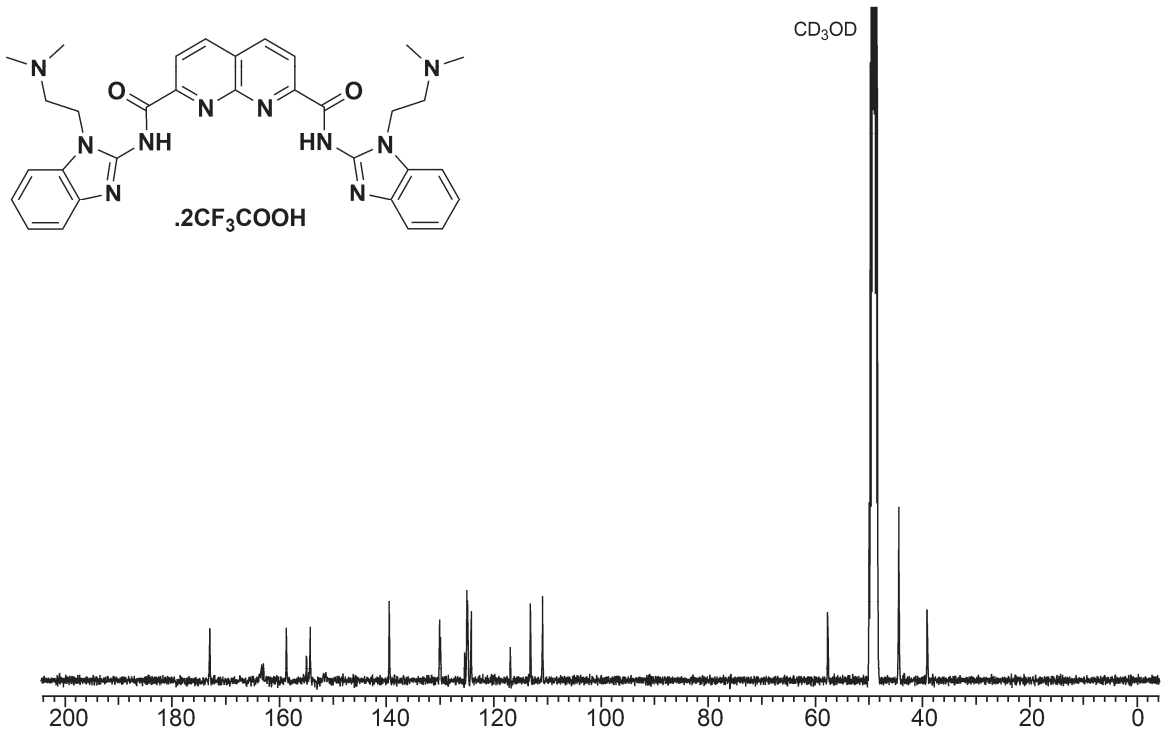

^{1}H NMR of compound **Nap-Pr**

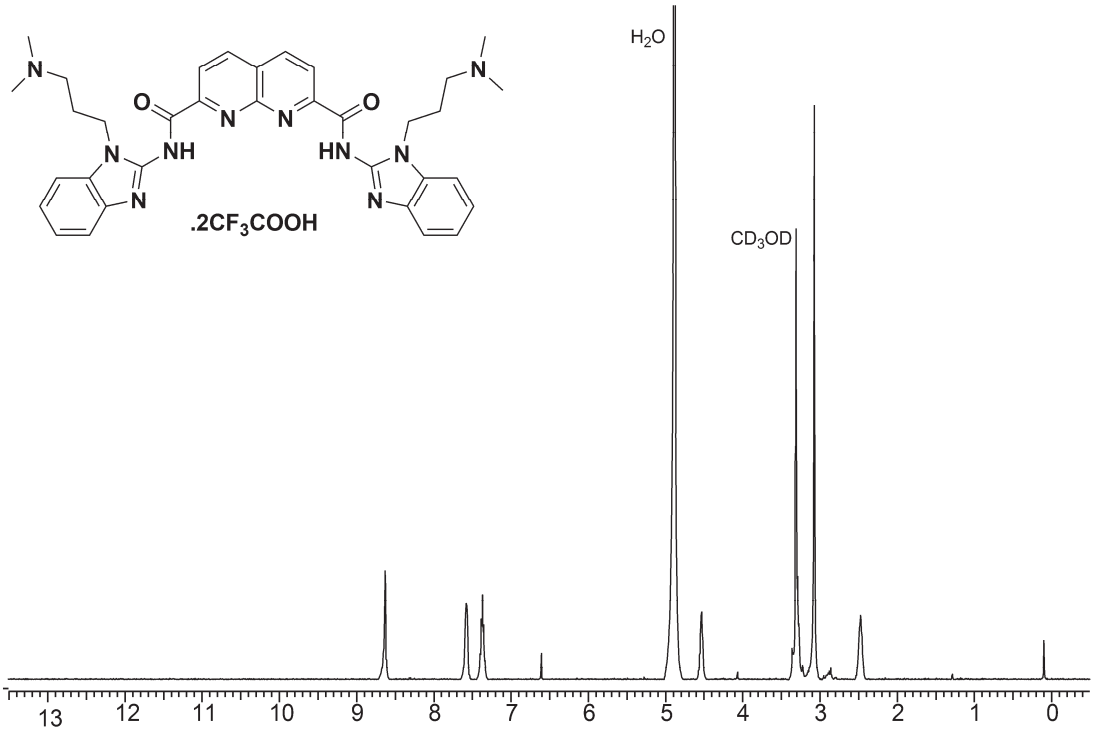

^{13}C NMR of compound **Nap-Pr**

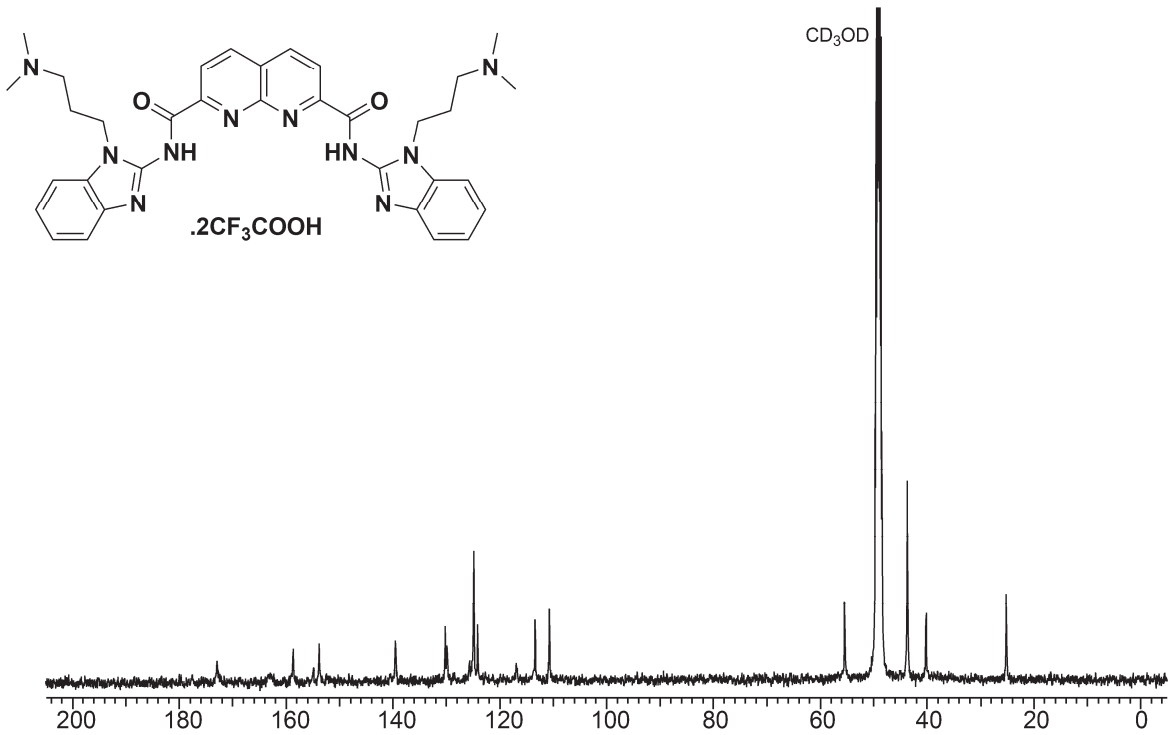

^{1}H NMR of compound **Phen-Et**

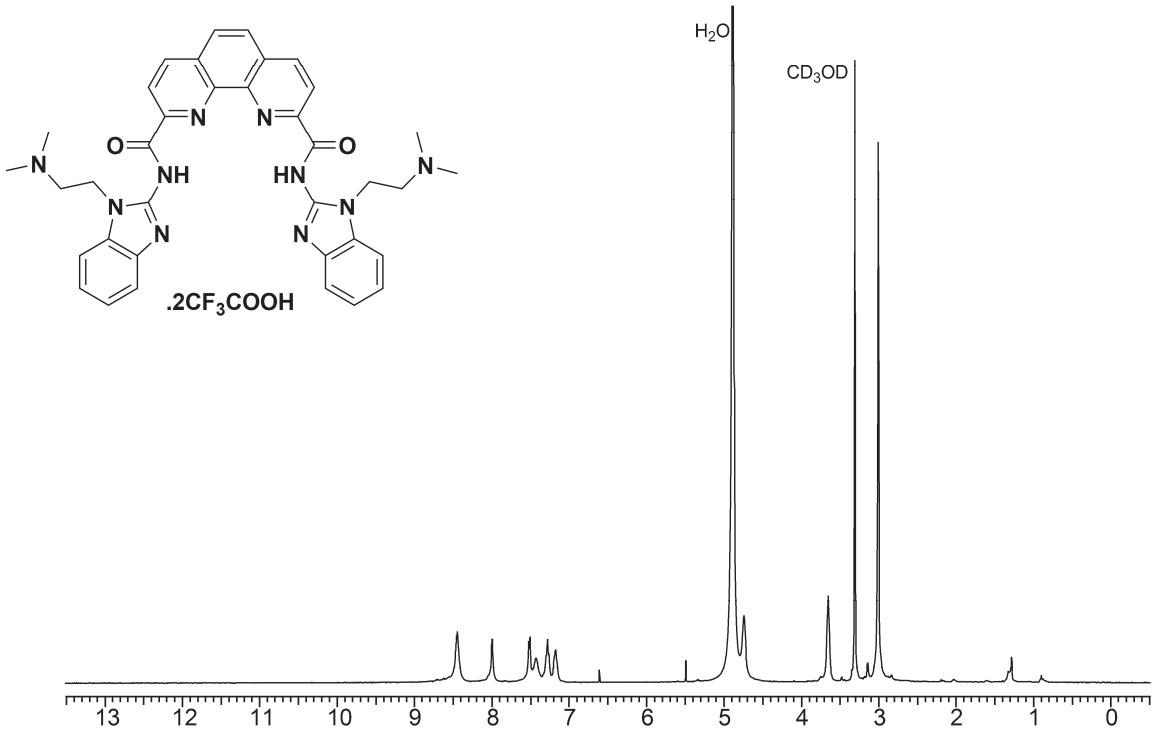

^{13}C NMR of compound **Phen-Et**

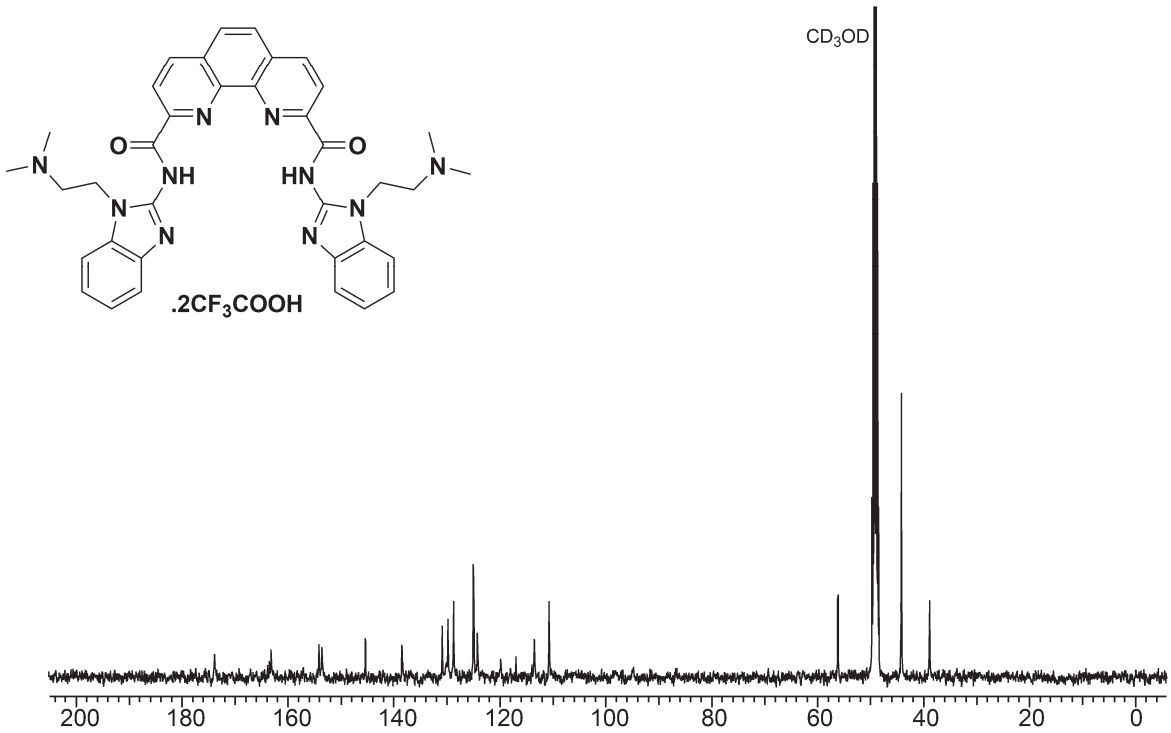

^{1}H NMR of compound **Phen-Pr**

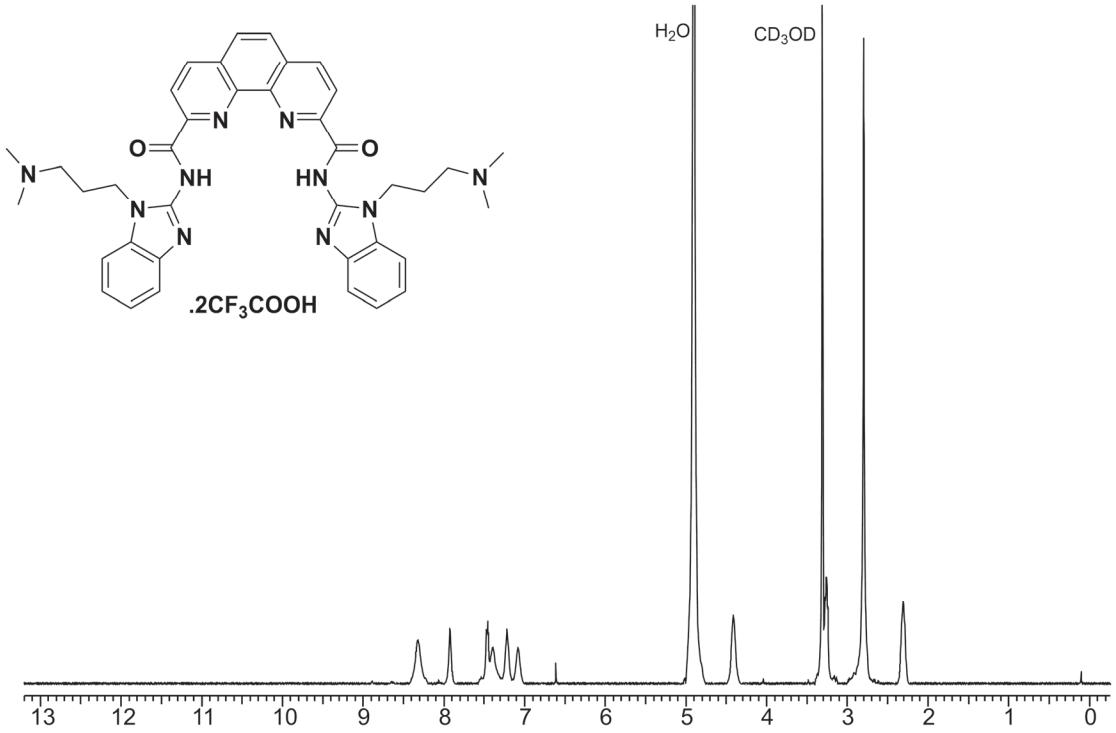

^{13}C NMR of compound **Phen-Pr**

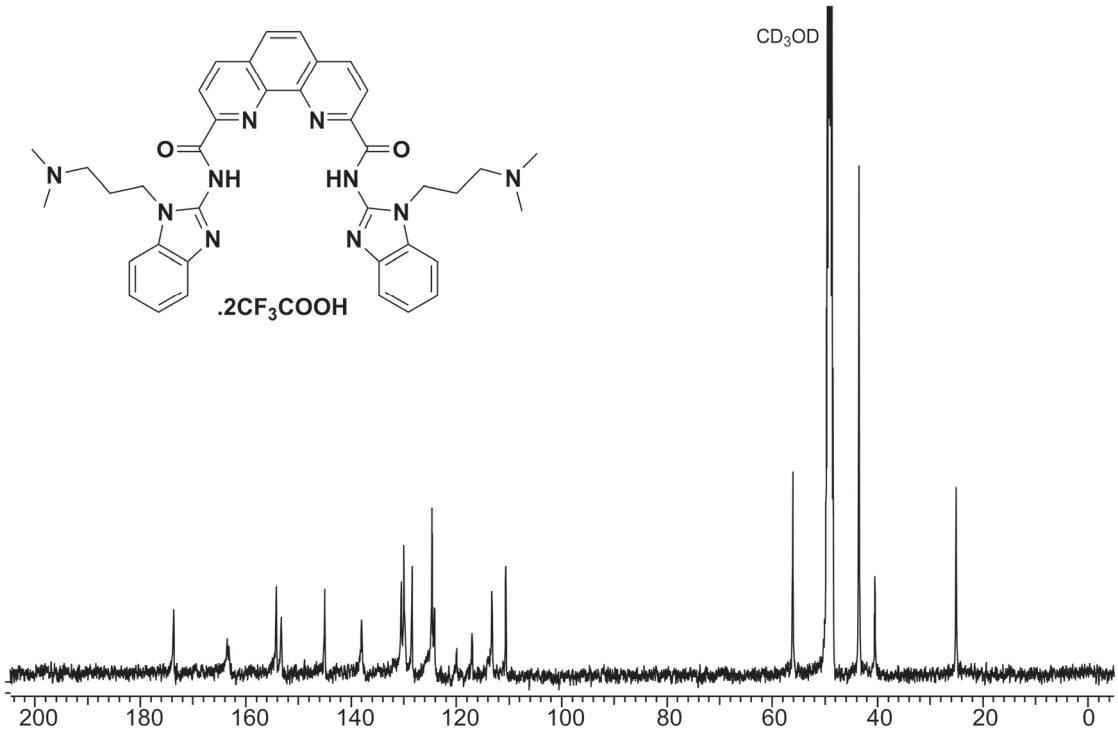

References

1. Seth, P. P.; Robinson, D. E.; Jefferson, E. A.; Swayze, E. E. *Tet. Lett.* **2002**, *43*, 7303−7306.
2. Dhamodharan, V.; Harikrishna, S.; Jagadeeswaran, C.; Halder, K.; Pradeepkumar, P. I. *J. of Org. Chem.* **2012**, *77*, 3233−3245.
3. De Cian, A.; DeLemos, E.; Mergny, J.-L.; Teulade-Fichou, M.-P.; Monchaud, D. *J. Am. Chem. Soc.* **2007**, *129*, 1856−1857.
4. Kieltyka, R.; Englebienne, P.; Moitessier, N.; Sleiman, H. In *G-Quadruplex DNA*; Baumann, P., Ed.; Humana Press: **2010**; Vol. 608, p 223
5. Sun, D.; Hurley, L. In *G-Quadruplex DNA*; Baumann, P., Ed.; Humana Press: **2010**; Vol. 608, p 65.
6. Parkinson, G. N.; Lee, M. P. H.; Neidle, S. *Nature* **2002**, *417*, 876−880.
7. Wang, Y.; Patel, D. J. *Structure* **1993**, *1*, 263−282.
8. Chung, W. J.; Heddi, B.; Tera, M.; Iida, K; Nagasawa, K.; Phan, A. T. *J. Am. Chem. Soc.* **2013**, *135*, 13495–13501.
9. Ambrus, A.; Chen, D.; Dai, J.; Jones, R. A.; Yang, D.Z. *Biochemistry* **2005**, *44*, 2048–2058
10. Schrodinger Suite 2011; Schrodinger Inc., LLC, New York, **2011**.
11. Gaussian 09, Revision A.02: Frisch, M. J. Gaussian, Inc., Wallingford, CT, **2009**.
12. Friesner, R.A.; Murphy, R.B.; Repasky, M.P.; Frye, L.L.; Greenwood, J.R.; Halgren, T.A.; Sanschagrin, P.C.; Mainz, D.T., *J. Med. Chem.*, **2006**, *49*, 6177–6196.
13. Fox, T.; Kollman, P. A *J. Phys. Chem. B* **1998**, *102*, 8070−8079.
14. Haider, S.; Neidle, S. *Methods Mol. Biol.* **2010**, *608*, 17−37.
15. Wang, J.; Wolf, R. M.; Caldwell, J. W.; Kollman, P. A.; Case, D. A. *J. Comput. Chem.* **2004**, *25*, 1157−1174.
16. Kollman, P. A.; Massova, I.; Reyes, C.; Kuhn, B.; Huo, S.; Chong, L.; Lee, M.; Lee, T.; Duan, Y.; Wang, W.; Donini, O.; Cieplak, P.; Srinivasan, J.; Case, D. A.; Cheatham, T. E. *Acc. Chem. Res*. **2000**, *33*, 889−897.
17. Pettersen, E. F.; Goddard, T. D.; Huang, C. C.; Couch, G. S.; Greenblatt, D. M.; Meng, E. C.; Ferrin, T. E.; *J Comput Chem.* **2004**, *13*, 1605−1612.
18. Baker, N. A.; Sept, D.; Joseph, S.; Holst, M. J.; McCammon, J. A. *Proc. Natl. Acad. Sci. USA*, **2001**, *98*, 10037−10041.
19. Lech, C. J.; Heddi, B.; Phan, A. T. *Nucleic Acids Res.* **2013**, 41, 2034–2046.
20. Hobza, P.; Šponer, J. *J. Am. Chem. Soc.* **2002**, *124*, 11802–11808.